Harmonic Intravascular Ultrasound

Martijn Frijlink

Copyright ©2006 by Martijn E. Frijlink.

Cover design by XD designers, Delft.

All rights reserved. No part of this publication may be reproduced, stored in a retrieval system, or transmitted, in any form, or by any means, electronic, mechanical, photocopying, recording, or otherwise, without the prior consent of the author. Printed by Optima Grafische Communicatie, Rotterdam, the Netherlands.

ISBN-10: 90-9020916-6
ISBN-13: 978-90-9020916-6

Harmonic Intravascular Ultrasound

Harmonisch intravasculair ultrageluid

Proefschrift

ter verkrijging van de graad van doctor aan de Erasmus Universiteit Rotterdam op gezag van de rector magnificus Prof.dr. S.W.J. Lamberts en volgens besluit van het College voor Promoties.

De openbare verdediging zal plaatsvinden op vrijdag 8 september 2006 om 11:00 uur door

Martijn Egbert Frijlink
geboren te 's-Gravenhage

Promotiecommissie

Promotoren:	Prof.dr.ir. A.F.W. van der Steen Prof.dr.ir. N. de Jong
Overige leden:	Prof.dr. H.G. Torp Prof.dr.ir. A. Gisolf Prof.dr. W.J. van der Giessen
Copromotor:	Dr.ir. D.E. Goertz

This work has been supported by the Technology Foundation STW (RPG-5442).

Financial support by the Netherlands Heart Foundation and the Interuniversity Cardiology Institute of the Netherlands (ICIN) for the publication of this thesis is gratefully acknowledged.

Financial contributions from Oldelft BV, Pfizer, Bristol-Myers Squibb Medical Imaging and Boston Scientific are gratefully acknowledged.

voor Saskia

Contents

Chapter 1

Introduction

1.1 Heart diseases

the circulatory system

The human circulatory system is comprised of blood, the heart, arteries, veins and capillaries. The main functions of this cardiovascular system are the delivery of oxygen and nutrients to all tissues in the body and the collection of metabolic waste products to the excretory organs (e.g. lungs, kidneys, etc.). Blood is also a carrier for hormones and plays an important role in the immune system of defense against infection. The heart is the muscular organ which pumps the blood (fig. 1.1). The right ventricle pumps deoxygenated blood into the pulmonary arteries, which carry the blood to the lungs, where it passes through a capillary network that enables the release of carbon dioxide and the uptake of oxygen. Oxygenated blood from the lungs returns to the heart via the pulmonary veins, then flows from the left atrium into the left ventricle, which pumps the blood through the aorta, the major artery which supplies blood to the body (Guyton and Hall, 1997).

coronary arteries

The arteries that supply the heart muscle, the myocardium, with blood are the coronary arteries. These arteries, when healthy, are capable of autoregulation to maintain coronary blood flow at levels appropriate to the needs of the myocardium. Approximately five percent of the total cardiac output (the volume of blood being pumped by the heart) flows through the coronary circulation (Silbernagl and Despopoulos, 1981). There are two main coronary arteries. The left coronary artery (LCA) arises from the aorta above the left cusp of the aortic valve, typically runs for 1 to 25 mm and then bifurcates into

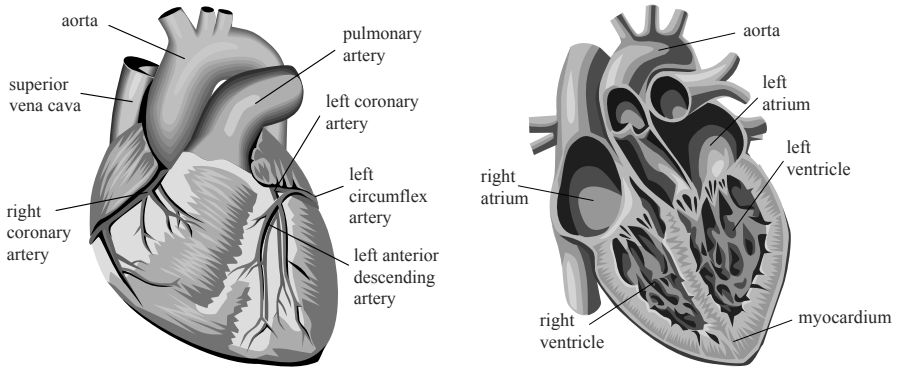

Figure 1.1: Schematic drawings of coronary arteries and a long-axis cross-section of the human heart.

the left anterior descending (LAD) artery and the left circumflex artery (LCX). The right coronary artery (RCA) originates above the right cusp of the aortic valve (fig. 1.1). Coronary arteries have lumen diameters in the 2 to 4 mm range. They have a tortuous, complex three dimensional course and are continuously in motion, which makes them a challenge for imaging techniques.

A normal arterial wall consists of three layers (see fig. 1.2). From inside out, the first layer called intima is a small (50–150 µm) layer that consists of a permeable endothelial cell layer separating the blood from the vessel wall. The internal elastic lamina separates the intima from the media. The media is the middle layer with a thickness of 200–300 µm. This layer consists of smooth muscle cells and in elastic arteries also of collagen and small elastic fibers. The third layer is called the adventitia and contains mainly smooth muscle cells mixed with fibrous connective tissue.

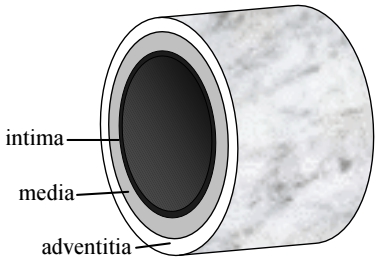

Figure 1.2: Schematic drawing of arterial blood vessel

atherosclerosis

Atherosclerosis (or arteriosclerosis) is a disease of arterial blood vessels. The early atherosclerotic lesion, also called fatty streak, is associated with endothelial cell dysfunction. Cholesterol is delivered by low-density lipoproteins (LDL) through the endothelial cells into the intima, and fatty deposits are building up on the inside of the arterial wall (Libby, 2002). This process causes monocytes, one type of white blood cells, to enter the intima too. Within tissues, monocytes change characteristics turn into inflammatory cells, so called called macrophages. Macrophages ingest oxidized cholesterol, that is delivered by LDL, and slowly turn into large "foam cells". Foam cells eventually die, and further propagate the inflammatory process. Over a period of many years or decades, these fatty streaks develop into plaques and increase in thickness. These vascular lesions known as atheromatous plaques or atheromas initially expand into the arterial wall (Glagov et al., 1987). Intracellular micro-calcification deposits form within vascular smooth muscle cells of the surrounding muscular layer, specifically in the muscle cells adjacent to the atheromas. In time, as cells die, this leads to extracellular calcium deposits between the muscular wall and outer portion of the atheromatous plaques. Atheromas within the vessel wall are soft. The progressive plaques consist of fibrotic material or lipids (atheroma), cell debris, calcium crystals and fibrotic material covered by a thin cap (µm-range) that has been formed by new connective tissue (fibroatheromas). During the progressive disease process, these fibroatheromas initially do not restrict the lumen, because of outward remodeling of the vessel. However, in late stages, typically after decades, these fibroatheromas could expand into the lumen, narrowing the opening of the vessel and therefore reduce blood flow. Narrowing of a vessel is called a stenosis. The *vasa vasorum* are small microvessels within the adventitia of larger arteries (e.g. coronary arteries) that supply the walls of these arteries with nutrients. *Vasa vasorum* are assumed to play an important role in the generation of atherosclerotic plaque.

vulnerable plaque

The "vulnerable" plaque is nowadays considered to be the most important underlying cause of acute cardiovascular events like unstable angina pectoris (chest pain), myocardium infarction (heart attack) and stroke. This vulnerable plaque is a plaque that is supposed to be unstable, prone to rupture, and that might lead to a severe stenosis. The vulnerable plaque can manifest itself in coronary arteries, carotid arteries and other large arteries. Pathologic studies of plaque rupture revealed that an eccentric thin-cap fibroatheroma (TCFA), characterized by morphological features and plaque composition, is assumed to be a vulnerable plaque (Schaar, 2005). A thin fibrous cap with macrophage and lymphocyte infiltration and decreased smooth muscle cell content covering an atheromatous core characterizes this TCFA. The instability of these plaques is mainly caused by large mechanical stresses that will develop in the thinnest part of the

fibrous cap.

In combination with local weakening of the fibrous cap by an increased density of macrophages, the instability of these plaques might lead to rupture of the cap. If a fibrous cap separating a soft atheroma from the bloodstream ruptures, fibroatheroma tissue fragments are exposed and released. Atheroma tissue fragments promote clotting, thrombus formation, by attracting blood platelet accumulation and activate the blood clotting system proteins. Thrombus formation might lead to a stenosis or artery lumen occlusion within seconds to minutes, potentially leading to cardiovascular events.

coronary artery disease

Coronary artery disease (CAD), also called coronary heart disease, is the end result of accumulation of atheromatous plaques within the walls of coronary arteries. If the blood supply to the heart muscle is reduced, cells are partially deprived of oxygen, which is called ischemia. When the myocardial blood supply is severely blocked, cells become necrotic and part of the myocardium dies, i.e. a myocardial infarction occurs. Cardiovascular disease, leading to acute coronary events, is currently the leading cause of death and illness in developed countries, and gets a more prominent role in developing countries. Over seven million people worldwide die each year from coronary artery disease. The major acknowledged modifiable risk factors are high blood pressure, high cholesterol level, smoking, physical inactivity, obesity, unhealthy diets and diabetes (Mackay and Mensah, 2004). Many interventional techniques have been developed to treat coronary artery disease. However, the major problem for making decisions on intravascular interventions or other treatments is the diagnosis of coronary artery disease. Identification of plaque vulnerability *in vivo* is essential to enable the development of treatment and stabilization of such plaque. Currently, the major feedback mechanism that helps cardiologists in decision making is diagnostic imaging. A wide variety of techniques can image the artery lumen, and/or differentiate between different tissue and plaque components. Diagnostic imaging techniques that have the potential to detect vulnerable plaques are developed or currently in development (Saijo and van der Steen, 2003).

1.2 Vascular imaging modalities

non-invasive techniques

X-ray imaging

Computed tomography (CT) scanners emit and detect X-ray radiation that passes a patient. This imaging technique is based on X-ray attenuation differences between different tissue types. The X-ray scanner rotates around the patient to allow for the detection

of many one-dimensional projections from different angles. Two-dimensional data-sets are then computed from these multiple acquisitions. Coronary CT angiography is currently feasible with multislice CT (MSCT), resulting in three-dimensional data-sets. The spatial resolution in the xy-plane of current MSCT scanners can currently be as low as 0.4×0.4 mm (Mollet et al., 2005). The spatial resolution in the z direction is determined by the minimum slice thickness, which ranges from 0.5 to 0.75 mm. This makes it possible to depict the coronary circulation down to the smaller branch vessels.

magnetic resonance imaging

Magnetic resonance imaging (MRI), formerly called nuclear magnetic resonance (NMR) imaging, is an imaging technique based on the magnetic property of an atom's nucleus. By aligning the magnetic axis of hydrogen atoms with an external magnetic field and perturbing this alignment using an electromagnetic field, different tissue types can be discriminated. Using current MRI techniques for imaging of atherosclerosis, small coronary plaque structures and components cannot be assessed (Yuan and Kerwin, 2004), and MRI acquisitions typically suffer from low signal intensities (de Feyter and Nieman, 2002). However, the development of sophisticated receiver coils resulted in MR images of coronary arteries with in-plane spatial resolution of 0.46×0.46 mm, and a 2 to 5 mm slice thickness (Fayad et al., 2000). An isotropic spatial resolution of 1.0 mm^3 in a three-dimensional coronary vessel wall imaging technique was reported by Kim et al. (2002). Recently, intravascular MRI catheters are being developed to perform high-resolution imaging of the vessel wall and atherosclerotic plaque invasively (Qiu et al., 2005; Schneiderman et al., 2005).

invasive techniques

X-ray imaging

Angiography uses an X-ray machine to create two-dimensional image projections of the human circulatory system visualized by X-ray contrast agent, which is typically injected through a catheter. Measurements of lumen diameter and cross-sectional area of arteries are commonly performed with angiography. The percentage of stenosis is a commonly used variable to quantify atherosclerosis (Reiber and Serruys, 1991). Coronary angiography has been so far the gold standard to assess the severity of obstructive luminal narrowing. However, the arterial lumen often includes non-circular cross-sectional areas at the site of a stenosis, resulting in misinterpretations of the actual percentage of stenosis. Although projections of lumen boundaries can be assessed, no information about plaque delineation and plaque components can be given with coronary angiography.

optical imaging and spectroscopy

Angioscopy is an intravascular technique based on direct visualization of arteries with light. This technique uses flexible catheters, small enough to image most vessels of interest. Since opaque blood limits the optical sight, flushing with saline is necessary to get a clear view of the artery wall, thereby potentially inducing ischemia. Intracoronary angioscopy allows assessment of the color and texture of the plaque surface and thrombi. Yellowish plaques seemed to have an increased instability (Uchida et al., 1995). However, intracoronary angioscopy is difficult to perform, and another limitation is that only the surface of the lumen can be visualized, limiting the characterization of plaque components that extend into the vessel wall.

Optical coherence tomography (OCT) is a relatively new technique that can provide cross-sectional images of vessels with a very high resolution. The intensity of laser light (1280–1350 nm wavelengths) that is reflected on surfaces and small particles is measured. Interferometry is used to get intensity information at different depths. The resolution of OCT images is typically 10–20 μm over a penetration depth of up to 2 mm (Brezinski, 2006). This intravascular technique uses a flexible catheter (0.4–0.6 mm diameter) containing optic fibers. Early *in vitro* experiments demonstrated a superior delineation of structural plaque details like thin caps and tissue proliferation (Brezinski et al., 1997). Limitations of OCT are the low penetration depth, and the light absorbance by blood which need to be overcome by saline infusion or balloon occlusion.

Raman spectroscopy can characterize the chemical composition of biological tissue in one dimension by measuring a wavelength change in backscattered light. When incident light (750–850 nm wavelength) excites molecules in a tissue sample, the backscattered light has undergone a wavelength shift (Römer et al., 1998). The wavelength shifts and signal intensities are dependent on the chemical components in a tissue sample. Animal experiments *in vivo* showed that intravascular Raman spectroscopy with an optic catheter is powerful in the detection of cholesterol and calcified components (van de Poll et al., 2001). Limitations of the technique are the limited penetration depth (1–1.5 mm), the long acquisition time, the absorbance of the light by blood and the lack of geometrical information.

thermal imaging

Thermography is a new technique that measures different temperatures in tissues with different thermal characteristics. Intravascular thermography is based on the detection of temperature increases accompanying the inflammatory process in a vulnerable plaque, as caused by macrophage infiltration. Current thermography catheters sense arterial wall temperature differences with one or multiple heat sensors with a contact surface of 0.5×0.5 mm. The temperature accuracy of these catheters is 0.05°C (Stefanadis

et al., 1999; Verheye et al., 2002). Early patient studies showed mostly higher temperatures in atherosclerotic plaques compared to healthy vessel walls. Current limitations of thermography are low signal-to-noise ratio (SNR), low spatial resolution, the lack of geometrical information and limited knowledge of the relation between *in vivo* measured temperatures and the pathologic state of diseased and healthy arteries (ten Have et al., 2005).

ultrasound imaging

Ultrasound imaging is based on the transmission and detection of pressure waves. Intravascular ultrasound is a technique to acoustically investigate arteries from within the lumen by means of an ultrasound catheter. More information about this image modality can be found in section 1.3.

elasticity imaging

Intravascular elastography is able to measure the mechanical properties of the vessel wall. Currently this can be done by intravascular ultrasound catheters (see section 1.3), however light guiding catheters (like OCT catheters) might be able to obtain similar information (Schmitt, 1998). The relative deformation of the arterial wall as caused by changing blood pressure is detected by measuring the time shift of subsequent radio-frequency (RF) traces (de Korte et al., 1998). Soft plaque components will deform more than stiff components. *In vivo* experiments showed that fatty plaques have an increased mean strain value, and high-strain spots were associated with the presence of macrophages (de Korte et al., 2002). A derivative of elastography, called palpography, plots only one strain value per angle as a color-coded contour at the lumen-vessel boundary (Doyley et al., 2001). Palpography has been validated *in vivo* and is currently clinically used as a tool to quantitatively assess local mechanical properties of (diseased) vessel walls (Schaar, 2005).

Modulography is an experimental new imaging method, which computes the Young's modulus distribution of coronary plaques from their measured strain elastogram by solving the inverse elasticity problem (Baldewsing et al., 2005, 2006). The Young's modulus image allows direct discrimination between soft and stiff plaque components, in contrast to the strain image.

1.3 Medical ultrasound

physical background

general

Sound is mechanical energy that propagates through a medium by compression and rarefaction of this medium, resulting in compressional pressure waves. Ultrasound is defined as sound with vibrational frequencies above the audible upper limit of 20 kHz. In nature, some animals such as dolphins and bats transmit ultrasound pulses and detect their echoes to navigate and locate objects. This is the key principle of diagnostic ultrasound imaging. Diagnostic ultrasound imaging is based on the transmission and reception of a short ultrasound wave with frequencies ranging from 1 to 50 MHz. The ultrasound pulses are generated by a transducer which converts electric energy into acoustic energy. Transmitted ultrasound travels through various biological tissues and is scattered, refracted and reflected in inhomogeneous tissue and at tissue boundaries. Parts of these scattered and reflected ultrasound waves, called echoes, are detected by the transducer, which now converts the received acoustic pulses to electric signals. Since the average ultrasound speed through biological soft tissue can be considered constant with a velocity value of around 1540 m/s, the time between transmission and reception of the pulse is directly related to the distance between the transducer and the reflecting object. Ultrasound has become a popular imaging method in obstetrics, gynaecology, neurology and cardiology. High frequency (> 10 MHz) ultrasound applications in the medical and biological field are ophthalmology, small animal imaging, and cardiology (intravascular).

display modes

The transmission and reception of a single acoustic pulse results in a depth-dependent echo amplitude, which can be displayed as a function of time in a single line, called A-mode. The transmission and reception of multiple pulses at different locations or at different angles can result in two dimensional images where the amplitude of the reflected ultrasound pulse displayed in gray scale, called B-mode imaging. Since the acquisition and imaging of individual B-scans can be fast, tissue motion can be visualized when subsequent B-scans are displayed as a movie. The resulting real-time cross-sections, that display acoustic parameters of the insonified part of the human body, give clinicians valuable information about tissue structure and functionality.

safety

Advantages of medical ultrasound over other diagnostic tools are the high efficacy, the relatively low costs, low invasiveness and the safety. In contrast to ionizing radiation

(i.e. X-ray), no negative biological effects induced by diagnostic ultrasound have been reported so far. Possible bio-effects as cavitation and thermal heating are well enough understood to control acoustic output and intensity levels to limit these effects. The frequently used exposure parameter Mechanical Index (*MI*) has become an indication of ultrasound safety with respect to mechanical (non-thermal) effects (Duck, 1999). The *MI* is defined as

$$MI = \frac{\textit{Peak negative pressure}\ \ [\text{MPa}]}{\sqrt{\textit{center frequency}\ [\text{MHz}]}} \tag{1.1}$$

Current diagnostic ultrasound equipment is limited to a maximum *MI* of 1.9 (Barnett et al., 2000).

resolution

The resolution (axial and lateral) of ultrasound images is directly related to the ultrasound frequency used. Axial resolution, which is the resolution in the direction of the ultrasound beam, is determined by the effective pulse length. The shorter the pulse, the higher the axial resolution. Lateral resolution, which is the resolution along the transducer face, is determined by the geometry of the transducer and the ultrasound frequency. High frequencies lead to small wavelengths and result in high resolution. However, high frequencies lead to increased attenuation of ultrasound waves and thus limit the penetration depth. A rule of thumb approximates the effective penetration depth for pulse-echo acquisitions in soft tissue to 100 wavelengths. Consequently, the optimal frequency used for imaging is a trade-off between high resolution and desired penetration depth. Typical ultrasound frequencies in the range of 1–5 MHz are used to image large organs non-invasively, corresponding to imaging depths of approximately 15–3 cm. The axial and lateral resolution of these images is in the order of a millimeter. High frequency ultrasound applications ($>$ 10 MHz) have limited penetration depths ($<$ 1.5 cm) but can result in high resolution images ($\leq$ 200 µm).

transducers

Most transducers used in medical ultrasound imaging are based on a layer of piezoelectric material with electrodes at the top and bottom. An electric field as applied by the electrodes causes the piezoelectric material to deform. The reverse piezoelectric effect converts mechanical deformation to electrical charge that can be sensed with the electrodes. The speed of sound and thickness of a piezoelectric material determine its resonant frequency. Piezoelectric transducer elements are further characterized by their transmit and receive sensitivity, both as a function of frequency. The center frequency

and relative bandwidth of a transducer determine the minimal pulse length. A transducer that is sensitive over a wide range of frequencies (high bandwidth) can transmit short, broadband pulses, subsequently leading to high axial resolution.

Mechanical sector scanners use a transducer that is swept through the scanning plane by vibration or rotation. The transducer moves while echoes from transmitted sound pulses are received from different directions. If multiple small transducer elements are combined in a linear array transducer, containing several acoustic elements in line, two-dimensional scans can be created without moving the transducer. Phased array transducers are similar to linear arrays but the sound beam can be steered and focused by applying phase changes to individual elements. At present, phased-arrays are frequently used in medical ultrasound. Two-dimensional phased arrays, consisting of a matrix of acoustic elements, can steer the transmit and receive beam in two directions, allowing for acquisition in three dimensions without mechanically moving the transducer.

Most piezoelectric materials are ferroelectric materials. The polycrystalline piezoelectric ceramic lead-zirconate-titanate ($PbZnO_3TnO_3$ or briefly called PZT) is currently the material of choice for most medical (array) applications because of its high coupling efficiency, physical durability, stability and low cost. A drawback of PZT is that its acoustic impedance is high relative to that of tissue, which reduces the efficiency of ultrasound transmission. Single crystal piezoelectric materials, like lithium niobate ($LiNbO_3$), kalium niobate ($KNbO_3$), and quartz, are characterized by low losses and moderate electromechanical coupling but are challenging to fabricate transducers from. These single crystal piezoelectric materials are mainly used in single element high frequency applications (Zhao et al., 1999). Some polymers with a crystalline phase can be used as piezoelectric transducers too. These piezopolymers are easily deformable and are characterized by a low acoustic impedance. The piezopolymers polyvinylidene difluoride (PDVF), and PVDF with trifluoroethylene (PVDF-TrFE), are known to be sensitive and typically have a broad bandwidth (Foster et al., 2000a). Another transducer material used in medical ultrasound is piezoelectric composite, which consists of embedded PZT fibers in a low-impedance polymer material to reduce the acoustic impedance mismatch to tissue.

An alternative for large array fabrication of piezoelectric material is the relatively new technology called capacitive micro-machined ultrasonic transducers (CMUTs) , which is based on existing silicon fabrication methods (Schindel et al., 1995; Ladabaum et al., 1996). A CMUT is a tiny, air-filled capacitor that can develop strain as a function of applied voltage. These CMUTs offer advantages such as very wide bandwidth, ease of fabrication of complex two-dimensional arrays and potential integration with electronics. Initial clinical use of medical phased array transducers has been reported by Mills and Smith (2003).

echocardiography

Echocardiography is the application of ultrasound to the imaging of the heart. Currently, ultrasound cardiac imaging is the most important non-invasive imaging technique that cardiologists have for diagnosis. Both anatomical and functional information of the heart can be obtained. Trans-thoracic echocardiography is applied when the transducer is placed on the thorax of a patient and the heart is scanned from outside the body. Ultrasound attenuation and reflection by the ribs and the lungs can limit penetration and cause image artifacts. The small footprint of cardiac phased-array transducers facilitates ultrasound imaging between the ribs. Another way to circumvent these attenuation problems is to image from within the esophagus (trans-esophageal echocardiography), thereby situating the transducer close to the heart. At present there is a tendency to use real-time three-dimensional ultrasound machines, which reduce acquisition time and enable two-dimensional planes with arbitrary orientation to be reconstructed off-line.

Ultrasound scattering from human blood is low compared to the scattering of surrounding tissue at frequencies below 10 MHz. Scattering from blood, and thus its visualization, can be enhanced by ultrasound contrast agents (De Jong, 1993; Frinking, 1999). Contrast echocardiography is a diagnostic method to image blood flow within vessels, heart chambers and the myocardium. The perfusion of tissue and organs give both anatomical and functional information. Ultrasound contrast agents are comprised of small gas bubbles with diameters between 1 and 10 μm encapsulated by a biodegradable shell (e.g. lipid or polymer). The individual contrast bubble can be characterized by its resonant frequency. The small encapsulated contrast bubbles pass the circulatory system, including small capillaries without causing cardiovascular events like a stenosis or occlusion. Encapsulation is necessary to prevent rapid dissolution of the gas content into the blood. Shell rupture can be induced by high ultrasound peak negative pressures, thereby allowing free gas bubbles to temporary increase contrast echoes. Conventional contrast echocardiography applications use frequencies in the range of 1–7 MHz. At present there is an increased interest in using smaller sized contrast bubbles for ultrasound applications at high frequencies (> 10 MHz). Current research focuses on targeting ultrasound contrast agent to specific cell types, like for example endothelial cells, which form a thin layer on the inside of arteries.

intravascular ultrasound

Arteries that are located deep inside the body, like coronary arteries, can not be imaged with sufficient resolution with trans-thoracic or trans-esophageal echocardiography. Intravascular ultrasound (IVUS) is a technique to acoustically investigate arteries from within the lumen by means of a catheter. IVUS is capable of providing real-time (30 frames per second) cross-sectional images of coronary arteries. Current commercially available IVUS systems are based on a single-element transducer or a phased array trans-

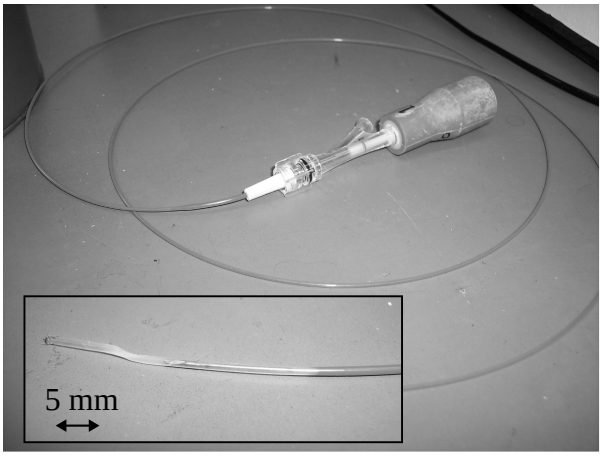

Figure 1.3: Conventional intravascular ultrasound catheter (Princeps 4.3F CCS, Du-MED) and close up of the catheter tip.

ducer. In single-element IVUS catheters, the side-way looking transducer at the tip of the catheter is continuously rotated over 360 degrees by means of a long (∼1.5 m) flexible axis (fig. 1.3 and fig. 1.4). The rotation speed of 30 rotations per second corresponds to the acquired frame rate. The center frequencies of these IVUS transducers are currently 20, 30 and 40 MHz, corresponding to a penetration depth of approximately 5 mm. The phased-array IVUS catheter, where a 64-element transducer is folded around the tip of the catheter, can be electronically steered to acquire cross-sectional images over 360°. The center frequency of this "solid-state" catheter is 20 MHz. The advantage of this catheter-type is the absence of rotational image artifacts. Rotating single-element catheters suffer from non-uniform rotation distortion (NURD), however the resolution as obtained with these catheters is better. In clinical practice, the rotating catheter-type

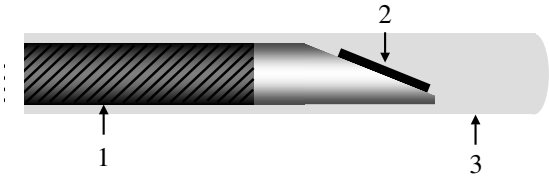

Figure 1.4: Schematic drawing of single-element rotating catheter, with drive shaft (1), transducer element (2) and protective sheath (3).

dominates the market. IVUS has become an important clinical tool for the detection and evaluation of coronary artery diseases (von Birgelen et al., 2003) and for therapy guidance (Degertekin et al., 2004) as well as for clinical research (Saijo and van der Steen, 2003). IVUS has been the basis for other RF-based imaging techniques like intravascular elastography (de Korte et al., 1998), palpography (Schaar et al., 2005) and virtual histology (Nair et al., 2002).

1.4 Harmonic Imaging

nonlinear acoustics

In conventional diagnostic ultrasound, propagation media are assumed to be linear, corresponding to acoustic waves that travel at a constant velocity c_0. Although this linear approximation is generally a satisfactory way to describe low-amplitude ultrasound beams, linear theory only applies to waves with infinitesimal low acoustic pressures.

In a nonlinear medium, the shape and amplitude of an acoustic wave is no longer proportional to the input excitation. In fluids and biological tissues, for example, this is caused by the nonlinear relation between pressure and density. The following Taylor series expansion expresses the pressure variations in fluids as a function of volume compression changes:

$$p - p_0 = A\left(\frac{\rho - \rho_0}{\rho_0}\right) + \frac{B}{2}\left(\frac{\rho - \rho_0}{\rho_0}\right)^2 + \frac{C}{6}\left(\frac{\rho - \rho_0}{\rho_0}\right)^3 + \ldots \tag{1.2}$$

where p is the total pressure, p_0 is the ambient pressure, ρ is the mass density, ρ_0 is the ambient density, and

$$A = \rho_0\left(\frac{\delta p}{\delta \rho}\right) \tag{1.3}$$

$$B = {\rho_0}^2\left(\frac{\delta^2 p}{\delta \rho^2}\right) \tag{1.4}$$

$$C = {\rho_0}^3\left(\frac{\delta^3 p}{\delta \rho^3}\right) \tag{1.5}$$

The partial derivatives are all evaluated in the unperturbed state. A good approximation for the relationship in fluids between phase speed v_t, and particle velocity u_t is (Hamilton and Blackstock, 1998):

$$v_t = c_0 + (1 + B/2A)\, u_t \tag{1.6}$$

where c_0 is the wave speed and B/A has its origin in equation 1.2. Third and higher order effects are assumed to be negligible. The quantity in parentheses, $1 + B/2A$, is referred to as the coefficient of nonlinearity β. This nonlinear coefficient is composed of two parts. The first (*"1"*) is the convective component, which adds the particle velocity to the wave velocity. Due to their local movement, particles in the wave move faster than the wave. The second component (*"$B/2A$"*) depends on the B/A-value which is a property of the medium indicating its nonlinearity.

When the coefficient of nonlinearity (β) is > 1 (which is generally the case for all media), this means that the phase speed is higher in high-density compressions, which corresponds to positive pressures, and lower in low-density rarefactions, which corresponds to negative pressures. A variation in this phase speed at different points in the wave results in progressive distortion of the acoustic pulse with propagation distance. Since the degree of distortion is dependent on the amplitude of the propagated wave, the term "finite amplitude" ultrasound is also used to indicate nonlinear ultrasound. A progressive change increase of a pressure waveform leads to the generation of harmonic signals and ultimately to acoustic saturation. The harmonic signals are generated at integer multiples of the fundamental frequency. During this process, acoustic energy is transferred from the fundamental frequency band to higher harmonic frequency bands.

Figure 1.5 shows time waveforms and corresponding frequency spectra at focus of a typical diagnostic ultrasound beam at low and high pressure. At low acoustic source pressure (fig. 1.5a) the pulse shape resembles the shape of the initial excitation pulse. There is no significant build up of higher harmonic components and thus propagation can be approximated to be linear. At a higher acoustic source pressure (fig. 1.5c), the shape of the waveform has changed and contains significant harmonic frequency components (fig. 1.5d). The asymmetry in the distorted wave, as observed by the magnitude of the peak compression exceeding that of the peak rarefaction, is due to phase variations between the fundamental frequency and its harmonics, caused by the finite size of the source transducer.

In media with low attenuation, the generation of higher harmonics could eventually lead to "shock waves", which is a pressure discontinuity where peak compression follows immediately behind peak rarefaction. Since it is physically impossible for the compression and rarefaction pressure peaks to overlap, shock waves cannot unlimitedly transfer energy to higher harmonics anymore, which leads to an increased attenuation. Dissipation causes the acoustic shock progressively to diminish in magnitude. During the dissipation process generated harmonics are absorbed and acoustic energy is converted

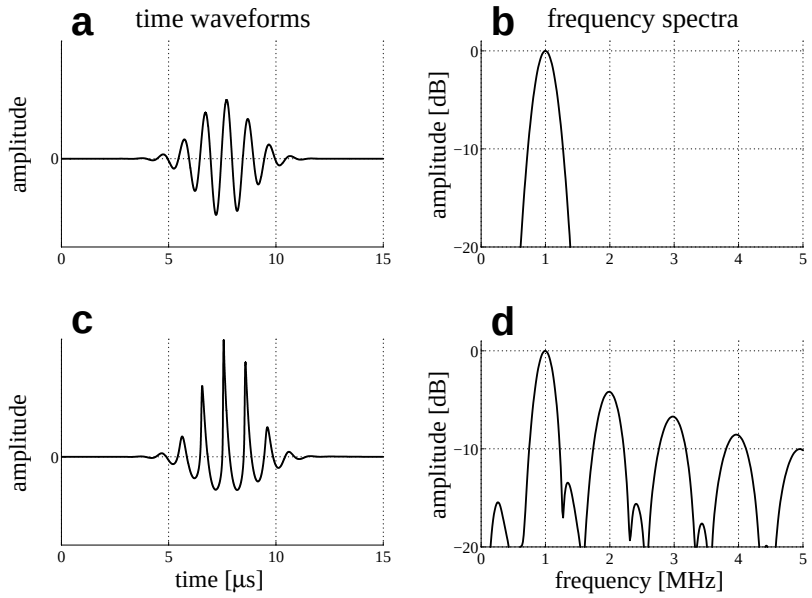

Figure 1.5: Pressure waveforms of a typical diagnostic ultrasound pulse at a low acoustic pressure (a) and high acoustic pressure (c) and their corresponding normalized frequency spectra (b) and (d) respectively. The pressure waveform at high acoustic pressure (c) consists of higher harmonics (see (d)) as a result of nonlinear propagation.

to thermal energy, leading to an excess loss of acoustic energy arising from the attenuating medium. The excess attenuation associated with shock propagation leads to a further phenomenon called acoustic saturation. This describes the condition of an acoustic field point when any increase in source amplitude fails to cause an associated increase in field amplitude. The increased source amplitude only leads to increased absorption, which results in increased heating.

Acoustic propagation in water gives rise to considerable nonlinear effects at diagnostic frequencies, in contrast to nonlinear propagation in biological tissues. In soft tissues there is direct competition between the nonlinear process that generates harmonics and acoustic attenuation caused by absorption and scattering. Higher frequencies are attenuated more since attenuation of biological tissues is frequency dependent. Since this causes the higher harmonics to be attenuated more, frequency dependent attenuation acts as a low-pass filter on the waveforms. The balance between the nonlinear processes (characterized by β or B/A) and the dissipative processes (characterized by attenuation), is given by the Gol'dberg number (Γ). When Γ is about 1.0, the effects of nonlinearity

Table 1.1: Measured B/A-values for some fluids and biological media

Medium	**Temperature [°C]**	**B/A**
water	20	5.0
whole blood	26	6.0–6.1
nonfat soft tissue		6.3–8.0
fatty tissue	37	9.6–10.3

and dissipation are comparable, when $\Gamma > 1$, nonlinear processes become more dominant, and when $\Gamma < 1$, absorption prevents significant distortion from developing. At diagnostic frequencies, the Gol'dberg number for soft tissue is about two orders of magnitude smaller than that for water. As a consequence of the high attenuation values of biological tissues, it is very hard to induce acoustic saturation in these tissues. Table 1.1 gives measured B/A-values (Duck, 1990) for some biologic tissues and fluids. All B/A-values in table 1.1 were measured at low diagnostic frequencies (< 10 MHz). Since the differences in B/A are small, the frequency-dependent attenuation is the dominant acoustic property that distinguishes nonlinear acoustic behavior in soft tissue from that in low-loss fluids, such as water. Nevertheless, the B/A-value has potential as a parameter for tissue characterization (Duck, 2002).

tissue harmonic imaging

In the early 90's people became aware of the significance of nonlinear wave propagation in medical ultrasound imaging (Ward et al., 1995; Averkiou et al., 1997; Christopher, 1997). The primary impulse for introducing harmonic imaging in clinical practice was to enhance acoustic contrast agents (see section 1.4). Commercial systems were supplied with transducers, capable of detecting the second harmonic signal, which was generated by contrast agents oscillating nonlinearly. Once introduced, however, it became obvious that images could be obtained without the introduction of contrast agents, and that furthermore these images demonstrated an improvement in image clarity. This diagnostic imaging technique where the received ultrasound signals are the harmonics of the transmitted frequency is called Tissue Harmonic Imaging (THI). THI utilizes nonlinear propagation to improve image quality. Properties of nonlinear acoustic beams in medical ultrasound have been studied extensively (Ward et al., 1997; Hamilton and Blackstock, 1998; Humphrey, 2000; Duck, 2002). The major advantages of THI in ultrasound imaging are:

1. *Narrower main lobe beam width*
   The generation of harmonic signal is nonlinearly dependent on the fundamental amplitude. Because the second harmonic generation is approximately proportional to the square of the fundamental amplitude (Duck, 2002), the harmonic beam width is smaller than the fundamental beam width. This reduced second harmonic beam width can lead to improved lateral resolution. A narrower beam could also be obtained by direct transmission at the second harmonic frequency from the transducer. However, in an attenuating medium, in which attenuation increases with frequency, it can be as efficient to generate second harmonic using nonlinear propagation as to transmit it directly.

2. *Reduced near field level*
   Since the harmonic field progressively builds up with propagation, and therefore with distance, the harmonic energy close to the source is low. Multiple reflections (or reverberations) from tissue layers within the body wall near to the transducer can give rise to considerable reverberant echoes in normal imaging, but since the harmonic content is low, the reverberations can be reduced with harmonic imaging.

3. *Reduced side lobe levels*
   Ultrasound beams generated by a transducer not only have a main lobe but also have additional, lower level, side lobes. Reflecting structures within these side lobes return off-axis acoustic energy to the transducer, resulting in undesired image artifacts. Since the harmonic generation is dependent on fundamental amplitude, the harmonic side lobe levels are reduced, resulting in a reduction of out-of-plane energy.

The combination of low harmonic content in the near field, a narrower beam and reduced side lobe levels results in a reduction of near field artifacts and an enhancement of the lateral resolution. Because of these advantages over fundamental imaging, THI has become a standard imaging mode in echocardiography in the frequency range from 2 to 10 MHz. The image quality improvement of THI has been demonstrated in precordial echocardiography and abdominal sonography, particularly in technically difficult-to-image (mainly obese) patients (Kasprzak et al., 1999; Tranquart et al., 1999; Burns et al., 2000). The main disadvantage of (second) harmonic imaging is that the harmonic signal levels as used in medical imaging are typically 10 to 20 dB lower than the fundamental signal level. Ultrasound transducers that are relatively sensitive at the second harmonic frequency are required to obtain an acceptable SNR in second harmonic acquisitions.

tissue harmonic imaging at IVUS frequencies

Although THI has been shown to increase image quality in medical ultrasound below 10 MHz, little work has been done to assess the feasibility of harmonic imaging for high-

frequency applications such as IVUS or ultrasound biomicroscopy (UBM). A recent study by Cherin et al. (2002) described the experimental characterization of fundamental and second harmonic beams of a spherically focused high-frequency PVDF transducer in the 20 to 40 MHz range. This type of focused transducer is typically used for the visualization of living tissues at microscopic resolution (Foster et al., 2000a,b). Another study by van der Steen et al. (1999) showed the feasibility of THI at high frequencies for IVUS and presented harmonic images of an excised human femoral artery *in vitro* that were acquired with a needle-mounted transducer element that was discretely scanned over a region of interest.

contrast harmonic imaging

In contrast to Tissue Harmonic Imaging, which is based on cumulative nonlinear effects, Contrast Harmonic Imaging is based on local nonlinear effects. The nonlinear pressure-radius relationship of acoustically driven bubbles such as those used in contrast agents significantly contribute to biomedical ultrasound. The nonlinear coefficient of contrast agents can be 1000× higher than that of biological tissue. This makes Harmonic Imaging extremely suitable to discriminate between biological tissue and contrast agents.

contrast harmonic imaging at IVUS frequencies

A number of studies have begun to explore the extension of microbubble contrast imaging techniques to transmit frequencies above 15 MHz. Recent studies have shown nonlinear scattering from microbubble contrast agents in the 14–40 MHz range (Goertz et al., 2001) and the feasibility of nonlinear microbubble imaging, both subharmonic and second harmonic, at transmit frequencies of up to 30 MHz (Goertz et al., 2005a).

In the context of IVUS, generally operating in the 15–50 MHz range, initial reports have highlighted two application areas. Cachard et al. (1997) demonstrated the feasibility of using contrast agents to assist in delineating lumen boundaries in phantoms. This may be useful in complex clinical situations such as in the presence of vascular dissections or thrombus. A second application is that of targeted contrast agents, which may be of relevance to the diagnosis or therapy of vascular disease. Demos et al. (1999) employed targeted echogenic liposomes to detect thrombus *in vivo*, also by means of enhancement in conventional IVUS images. Moran et al. (2002) examined the scattered signals from several commercial contrast agents with commercial IVUS instrumentation.

1.5 Thesis outline

The aim of this study was to develop Harmonic Imaging for intravascular ultrasound. Chapter 2 describes the initial experimental setup and prototype nonlinear IVUS system that was constructed to characterize fundamental and harmonic high-frequency beams, and to perform imaging in both fundamental and second harmonic modes. In chapter 3, the effect of THI on stent image artifact reduction was examined for two different transducers, a focused PVDF transducer and an unfocused IVUS transducer. In chapter 4, the feasibility of THI with a conventional single-element continuously rotating IVUS catheter was investigated in both a tissue mimicking phantom and an atherosclerotic rabbit aorta *in vivo*. Chapter 5 describes the design, fabrication, and characterization of a piezoelectric transducer with an oval aperture of 0.75 by 1 mm that has been optimized for harmonic imaging at 20–40 MHz. This "dual-frequency" transducer is characterized by two sensitivity peaks at 20 and 40 MHz. In chapter 6, an improved version of this dual-frequency IVUS element was mounted in a commercial IVUS catheter. The performance of the dual-frequency catheter was investigated in THI mode and compared to a conventional IVUS catheter, both with a tissue phantom and in rabbit aortas *in vivo*. Chapter 7 describes the development of a simulation tool to study nonlinear IVUS beams and the influence of catheter rotation, and axial catheter-to-tissue motion on the efficiency of pulse inversion signal processing. In chapter 8, the feasibility of performing contrast harmonic imaging (CHI) with the prototype nonlinear IVUS system in the 15 to 50 MHz range was investigated. Chapter 9 indicates the feasibility of CHI with an IVUS catheter as a new technique for *in vivo vasa vasorum* imaging. Finally, chapter 10 concludes the thesis with future perspectives and discusses potential applications and limitations of harmonic IVUS.

Chapter 2

Experimental setup

2.1 Introduction

In order to test the feasibility and performance of harmonic imaging at intravascular ultrasound frequencies (10–60 MHz) experimentally, a measurement setup was constructed. This experimental setup made it possible to measure the generation of harmonic fields from different high-frequency transducers and to measure the frequency response characteristics of these transducers. Next to these transmission experiments, this apparatus was also able to perform pulse-echo measurements and initial harmonic imaging experiments. In a later stage of the Harmonic IVUS project, this experimental setup was expanded to a prototype IVUS acquisition system that was developed to operate in either fundamental imaging mode, or in second harmonic imaging mode. By means of an adapted motor unit, IVUS catheters could be employed to perform Tissue and Contrast Harmonic Imaging *in vitro* and *in vivo*. Since the configuration of the experimental setup plays an essential role in the development of Harmonic IVUS applications, a detailed description of individual components and a description of the prototype system as used in *in vivo* experiments will be given in this chapter.

2.2 Components of experimental setup

arbitrary waveform generator

A block scheme of the experimental setup is showed in fig. 2.1. An arbitrary waveform generator (AWG) is used to generate low-amplitude (< 2 V_{pp}) pulses. An important characteristic of an AWG is that arbitrary waveforms can be programmed. The Nyquist Theorem, which states that the sample frequency to generate or detect a sinusoidal wave

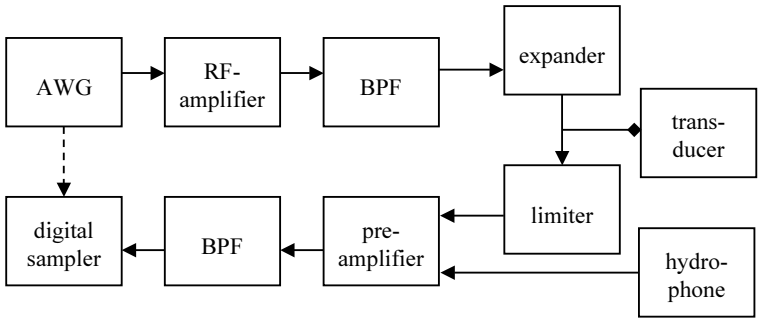

Figure 2.1: Schematic representation of the acquisition system for transmission and pulse-echo experiments.

should be at least two times higher than that of the sine frequency, determines the minimal sampling rate that is required.

Harmonic Imaging in medical ultrasound is based on the detection of harmonic signals which are generated by nonlinear wave propagation or nonlinearly oscillating microbubbles. However, harmonic signals can also be generated by nonlinear distortion of the acquisition system. To discriminate between excitation and propagation harmonic signals, the generation of the acoustic pulses should be well defined in the frequency domain, avoiding the generation of higher harmonics. Harmonic distortion should be low for system components (e.g. AWG and amplifiers). Since harmonic distortion is partly caused by quantization noise, it can be reduced by an AWG with an increased vertical resolution.

Averaging a number of Radio-Frequency (RF) acquisitions can increase the signal-to-noise ratio (SNR) of (semi-)static measurements. Clock synchronization of the AWG with the digital sampling apparatus does significantly help to enable averaging and pulse sequencing (e.g. pulse inversion techniques), because it can avoid time consuming interpolation and cross-correlation techniques.

An AWG gives flexibility to compensate for deterministic signal distortion. For example, harmonic distortion as generated by the AWG itself, the nonlinear amplifier, or nonlinear transducer characteristic could be partly compensated for by changing the waveform (Zhou et al., 2004).

The AWG (AWG520, Tektronix, Beaverton, OR, USA) that was used in the experimental setup of all experiments in this thesis had a maximum sampling rate of 1000 MS/s,

and a vertical resolution of 10 bits. For synchronization purposes, we used the sampling rate of 400 MS/s, corresponding to the sampling rate (or a multiple of that) of the PC-digitizer. Additional in- and outputs of the AWG were used for gating the high power RF-amplifier and for clock synchronization by means of a 10-MHz reference signal.

power RF-amplifier

Low-amplitude pulses generated by the AWG have to be amplified to sufficiently high driving voltages for the transducer to be able to generate acoustic pressure pulses. A broadband (10 to 60 MHz) linear high-power RF-amplifier with an output power during the pulse of 100 to 1000 Watts is necessary. As such high-power amplifiers typically generate considerable noise, some amplifiers have a "gating" option, that actively switches the RF-output to avoid the emission of noise after the pulse is transmitted.

High-power amplifiers generally introduce a considerable amount of nonlinear distortion. The third harmonic distortion level is typically as high as 15 dB below the carrier frequency. Odd harmonic generation is mainly caused by "symmetric" distortion of the input signal. Second harmonic distortion levels are slightly better, typically 20 to 25 dB below the carrier frequency. It is the difference in amplification between the positive and negative part that causes the generation of even harmonics. Both symmetric and non-symmetric distortion are dependent on the amplitude of the input RF-signal. In normal operation, the harmonic distortion increases with increasing input amplitudes.

The 60-dB amplifier that was used in all experiments (LPI-10, ENI, Rochester, NY, USA) was originally intended for MRI and NMR spectroscopy applications. This 1000 Watts linear power amplifier has an effective frequency range from 8 to 100 MHz and could be gated to avoid the transmission of noise during reception in pulse-echo acquisitions. A disadvantage of this optional gating signal is crosstalk, resulting in an unwanted broadband signal in the RF-output. Because this gating-artifact is independent on the input amplitude, its effect can be reduced by using a high-power attenuator in combination with a higher input RF-amplitude. Another limitation of the amplifier is the limited Pulse Repetition Frequency (PRF) of about 15 kHz, which limits the PRF of the complete acquisition system and also limits the maximum rotation speed of single element IVUS catheters in Harmonic IVUS imaging experiments.

The method that was used to avoid the transmission of harmonic distortion at the second harmonic frequency was analog filtering by a high-power custom-made band-pass filter (8 to 28 MHz, 5^{th} order Butterworth). In all experiments, the transmitted signal at the second harmonic frequency was suppressed to more than 45 dB below the fundamental level for all excitation voltages used when operating in second harmonic mode. For 40 MHz transmit frequency, a different high-power custom-made band-pass filter (31

to 51 MHz, 5^{th} order Butterworth) was used to suppress the gating artifact from the RF-power amplifier.

protection electronics

The filtered, high-amplitude pulse passes a passive expander, consisting of an anti-parallel diode pair (Lockwood et al., 1991a) that was used to suppress the transmission of noise from the power amplifier during receive. In the ideal case, this diode pair only passes current if the absolute voltage level exceeds the threshold of approximately 0.6 Volts, resulting in a reduction of low-amplitude noise. Since this expander has a nonlinear transfer function, the generation of harmonics will distort the waveform. For diodes with identical specifications, the distortion is "symmetric", which only results in odd harmonics.

A passive limiter, consisting of a resistor and an anti-parallel diode pair connected to ground, protected the receive electronics from high voltages during transmit in pulse-echo mode. In the ideal case, the diode pair clips voltage levels below and above approximately -0.6 Volts and 0.6 Volts respectively. Receive signal distortion is negligible because the signal amplitudes from the transducer are low (< 0.1 V_{pp}).

Passive 50-Ω attenuators (Minicircuits, Brooklyn, NY, USA) with a fixed attenuation (-1, -2, -3, -6, -10 and -20 dB) over a broad frequency range (DC to 2000 MHz) were used at different positions in the electric circuit for two reasons. First, the input and output impedance of these attenuators are 50-Ω, which makes them ideal for matching the electrical impedance to other 50-Ω electronic components. Second, these attenuators can reduce the signal amplitude to use the linear input range of receive amplifiers and to make optimal use of the dynamic range of the digital sampler. The additional noise from these attenuators is negligible.

hydrophone

Pressure measurements require a measurement device that accurately measures acoustic pressures. This device, called a hydrophone, is a sensitive receiver for acoustic waves underwater. Diffraction in acoustic fields causes the pressure waveform to change from point to point. To avoid spatial averaging, the diameter of the sensitive area of a hydrophone should be in the same order or smaller than the wavelength. A broadband PVDF needle-type hydrophone with a sensor diameter of 75 μm (Precision Acoustics Ltd, Dorchester, UK) is used for fundamental and harmonic beam characterization, as well as for frequency response measurements. This hydrophone was calibrated from 2 to 60 MHz (National Physics Laboratory, Teddington, UK), with uncertainties from ±7 to ±26%. The sensitivity is in general frequency dependent, though our specific

hydrophone has an almost flat sensitivity curve between 4 and 32 MHz.

receive amplifier

The low-amplitude receive signal from the transducer in pulse-echo mode or from the hydrophone in transmission mode needs to be amplified in order to use the full input voltage range of sampling devices such as digital samplers and oscilloscopes. Depending on the required signal gain, we could choose between three broadband (100 MHz) low-noise amplifiers (Miteq,Hauppage, NY, USA), namely a 35 dB (AU-1189), 45 dB (AU-1263) or 59 dB (AU-3A-0110) amplifier. Different amplification values could be realized in combination with the attenuators.

analog filters

In order to reduce the influence of noise and offset and to suppress fundamental or harmonic signal, a range of custom-made band-pass filters were fabricated. The chosen filter characteristic was of the Butterworth type, which is a compromise between a sharp Chebyshev and a flatter Bessel transfer function. A Butterworth frequency response has a relative smooth shape and the slope of the response decreases with 6 dB per octave (an increase to twice the frequency) multiplied by the filter order. Our band-pass filters were all of order five (slope of 30 dB per octave) and had primary attenuation values in the pass-band of approximately 1 dB. In harmonic acquisitions these filters were used to reduce fundamental signal amplitude before amplification to increase the effective dynamic range of the amplified signal. Analog filtering post-amplification suppressed broadband noise as introduced by the receive amplifier. In different studies, different band-pass filters were used, which will be indicated in the concerning chapters.

digital sampler

To digitize and store RF-traces information from the transducer or hydrophone, a data-acquisition device is needed. The Nyquist theorem requires that the minimum sampling rate of a digital sampler is twice as high as the maximum frequency of interest. The dynamic range (DR) should cover the maximum SNR of receive signals. Since quantization noise limits the DR of a digital sampler, the DR can be enhanced by a digital sampler with an increased vertical resolution.
An 8-bit A/D PCI-digitizer (DP235, Acqiris, Geneva, Switzerland) was used in the first studies, and digitization rates of 200 MS/s and 400 MS/s were used. In later studies, the prototype Harmonic IVUS system (section 2.3) consisted of a 12-bit A/D PCI-digitizer (DP310, Acqiris, Geneva, Switzerland) with a sample rate up to 400 MS/s. In all studies, the sampling clock of the digitizer PCI-card was synchronized to the sampling clock of

the AWG by means of a 10-MHz reference signal. All digitized RF-signals were stored on the acquisition PC's harddisk.

XYZ-positioning system

In studies where transducers were moved with respect to a stent or hydrophone, the transducers were moved by a motorized XYZ micropositioning system (MP63-25-DC, Steinmeyer, Dresden, Germany) with a resolution of 0.02 μm and a positioning accuracy of less than 1 μm. This positioning system was controlled by the acquisition PC, which automatically synchronized movement to acquisitions.

2.3 Prototype Harmonic IVUS system

system configuration

The expansion of the measurement setup resulted in a prototype harmonic IVUS system that was used to test the feasibility of THI and CHI with a continuously-rotating single-element IVUS catheter. This system was used to acquire signals and create fundamental and harmonic images of tissue phantoms and of healthy and atherosclerotic rabbit aortas *in vivo*. An example of a detailed configuration scheme of the Harmonic IVUS system as depicted in fig. 2.2 indicates the signal paths of the transmitted and received RF-signal, gating signal and synchronization signals. The individual components are described in section 2.2.

motor unit

In order to create cross-sectional images of tissue phantoms and rabbit aortas, single-element IVUS catheters should be mechanically rotated by a motorized system. In the prototype Harmonic IVUS system the catheters were mechanically driven by a motor unit (Du-MED, Rotterdam, the Netherlands) that was modified to permit rotational speed control, as well as to enable the transmission of controlled catheter input signals and the collection of received signals. In clinical practice, the rotation speed equals the frame rate which is 30 frames (rotations) per second, however a lower rotation speed was used in initial harmonic IVUS imaging experiments as described in chapter 4, 6, 8 and 9.

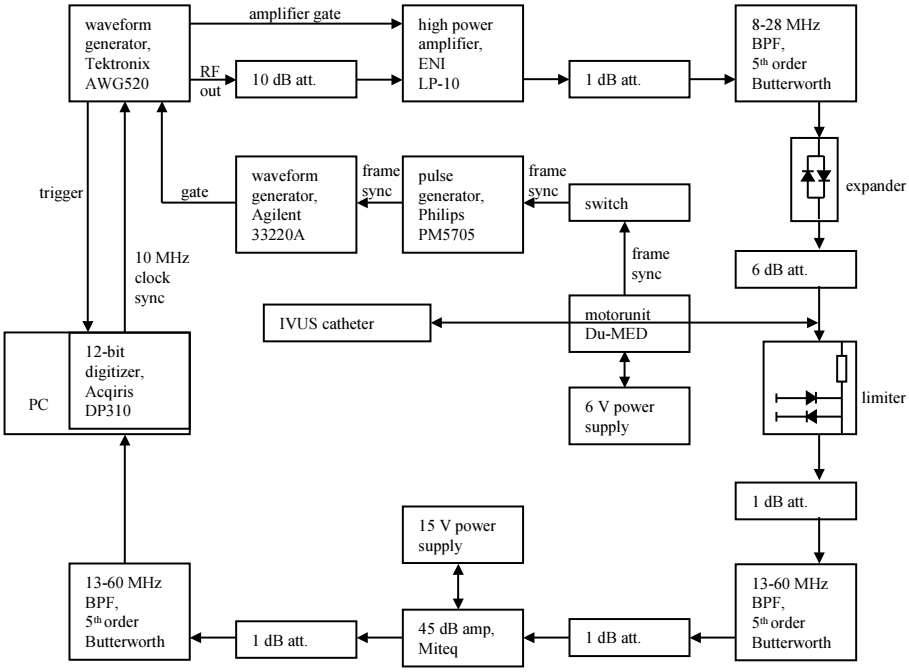

Figure 2.2: Example of a typical configuration of the prototype harmonic IVUS setup for fundamental and harmonic acquisitions with a mechanically-rotated single-element IVUS catheter.

Chapter 3

Reduction of stent artifacts using high-frequency harmonic ultrasound imaging

Based on the publication *"Reduction of stent artifacts using high-frequency harmonic ultrasound imaging"* by Frijlink M.E., Goertz D.E. and Van der Steen A.F.W., Ultrasound Med Biol, 31(10):1335–1342, 2005. *with permission from the World Federation of Ultrasound in Medicine and Biology*

Abstract – Tissue harmonic imaging (THI) has been shown to improve medical ultrasound (US) image quality in the frequency range from 2 to 10 MHz and might, therefore, also be advantageous in high-frequency US applications, like US biomicroscopy and intravascular ultrasound (IVUS). In this study, we compared high-frequency THI (40 MHz) with fundamental imaging (20 and 40 MHz) with a distorting reflective metal stent in the near fields of both a spherically-focused US biomicroscopy transducer (aperture 8 mm, focal distance 13 mm) and an unfocused elliptical IVUS element. Hydrophone measurements of the harmonic beam (40 MHz) of both transducers showed relatively low signal strength in the near field compared with both (20 and 40 MHz) fundamental beams. For the focused transducer, THI suppressed the second stent echo up to 14 dB compared with fundamental imaging. No significant reduction in stent artifact imaging was observed for the unfocused IVUS element.

3.1 Introduction

Although THI has been shown to be feasible at high ultrasound frequencies (>10 MHz) (van der Steen et al., 1999; Cherin et al., 2002), quantification of artifact reduction with THI relative to fundamental imaging at higher frequencies in UBM and IVUS applications has not yet been reported.

IVUS is a commonly used clinical technique capable of providing real-time cross-sectional images of coronary arteries. An important application for IVUS is to guide stent deployment and study the therapeutic effect stents. Stents are small metallic expandable wire-mesh tubes, sometimes coated with drugs (Serruys et al., 1994). A problem in IVUS is that stents can degrade the image quality through artifacts such as reverberations, ringing and shadowing, which complicate the interpretation of IVUS images (Finet et al., 1998; Thrush et al., 1997). Nonetheless, IVUS is considered to be an accurate tool for the assessment of optimal stent deployment and follow-up of its therapeutic effect (Blessing et al., 1999; Bruining et al., 1999; Eeckhout et al., 2003; von Birgelen et al., 2003). IVUS can quantify both stent expansion and stent strut-vessel wall malapposition in a substantial percentage of patients. The conventional function of a stent is to maintain a patent lumen in a diseased artery. A recent development is the "drug eluting stent", which is a drug-coated stent that delivers drugs locally to the arterial wall (Moran et al., 2002). Investigation of the local effects of drug delivery by a drug-coated stent is one circumstance that may benefit from a possible reduction of stent artifacts with the use of harmonic IVUS.

In this study, an experimental setup was constructed to image in both fundamental (20 and 40 MHz) and second harmonic modes (40 MHz). The effect of THI on stent image artifact reduction was examined for two different transducers, a focused PVDF transducer and an unfocused IVUS transducer. We characterized the fundamental and harmonic beams of both transducers with a hydrophone. In the imaging experiments, the degradation in image quality because of the presence of a stent in the near field of the acoustic beam was assessed by comparing different imaging modes (fundamental 20 and 40 MHz and second harmonic 40 MHz).

3.2 Materials and Methods

Experimental setup

The experimental setup, constructed to image in both fundamental and harmonic modes at high frequencies, is described in section 2.2. During second harmonic experiments, a high-power custom-made band-pass filter (8 to 28 MHz) suppressed the unwanted transmitted second harmonic signal to 51 dB below the fundamental (measured at 25%

−6-dB band width). Two different transducers were used in this study. The first one was a spherically-focused PVDF transducer T1 (aperture of 8 mm, focal length of 13 mm and center frequency of 20 MHz) (Sherar and Foster, 1989). The second transducer was an elliptical unfocused lead zirconate-titanate (PZT) element T2 (long axis 1 mm, short axis 0.75 mm and center frequency of 30 MHz). This transducer was extracted from a conventional IVUS catheter (Princeps 4.3 F, Du-MED, Rotterdam, The Netherlands) and mounted on a needle tip with its beam directed perpendicular to the needle axis. The needle hydrophone (see section 2.2) was used as a detector in the beam profile experiments.

The transducers were moved by an XYZ-micropositioning system. A rotational motor (DT 65-LM, Steinmeyer, Dresden, Germany) with a resolution of 0.001 degrees and a positioning accuracy of 0.015 degrees was used to angle the IVUS needle mount (T2) about its long axis to simulate catheter rotation.

The stents used in the imaging experiments were NIR^{TM} stents (Medinol, Ltd., Jerusalem, Israel), capable of expanding to a lumen diameter of 3.0 to 5.0 mm. The circular expanded stent had a length of 12 mm and a lumen diameter of approximately 4 mm. The flattened stent was obtained by cutting an expanded circular stent and removing its curvature.

The phantom experiments were performed with a tissue- mimicking phantom. The material used is a combination of 8% gelatin (Type A, Sigma Chemical Company, St Louis, MO, USA), 2% agar-agarose (Agar Agar CMN, Boom, Meppel, the Netherlands) and 1% carborundum powder with a particle size in the range of 3 to 10 μm (Cats import, Hoogvliet, the Netherlands) diluted with distilled water. The velocity and attenuation of this phantom material have been studied at IVUS frequencies by de Korte et al. (1997).

Experiments

In all experiments, Gaussian-enveloped pulses with center frequencies of either 20 MHz or 40 MHz were generated. A Gaussian modulation was chosen because of the absence of secondary lobes in the frequency domain. The −6-dB fractional band width of the excitation pulses used in the beam profile experiments was 50% and, in the stent imaging experiments, both 25% and 50% fractional band width pulses were used. These band widths are comparable to those used in commercial IVUS systems. In all experiments, we acquired results for the fundamental 20-MHz mode (F20), the fundamental 40-MHz mode (F40) and the harmonic 40-MHz mode (H40) (i.e., the second harmonic at 40 MHz of the fundamental transmitted at 20 MHz). We used signal averaging in all acquisitions to increase the signal-to-noise ratio (SNR). Pulse inversion (PI) was used to achieve suppression of the fundamental signal in the H40 acquisitions (Hope Simpson et al.,

1999).

Beam profile experiments

To characterize the fundamental and harmonic sound fields of both the focused PVDF transducer (T1) and the unfocused IVUS element (T2) in water, pressure levels were measured with the hydrophone.

Pressure levels of T1 were acquired in two lateral scan planes perpendicular to the transducer axis. One scan at focus (13 mm from T1) was sampled at regular intervals of 20 μm in both directions and another scan was made at half the distance to focus (6.5 mm from T1), with a regular sampling distance of 50 μm in both directions. Pressure levels of T2 were acquired in an axial scan plane parallel to the short axis of the transducer. The scan was sampled at 200-μm intervals in the axial direction and at 50-μm intervals in the lateral direction.

After data acquisition, the maximum of the envelope was calculated and used to plot the axial beam profiles.

Stent reverberation experiments with PVDF transducer

To examine the effect of harmonic imaging on multiple echoes from a highly reflective target in the near field of a high-frequency US beam, a flattened stent was interposed halfway (6.5 mm) between T1 and a 20-μm diameter glass fiber point scatterer that was located at focus (13 mm from T1). The orientation of the flattened stent was perpendicular to the beam axis. We acquired the US signals in pulse-echo mode in the focal plane, perpendicular to the beam axis, with a spacing of 10-μm steps in both directions (0.8×0.8 mm). Next, the envelope was calculated and the maximum value within a limited time window was used to plot C-scans of the point scatterer and the stent reverberations. Power comparisons of areas within the C-scan were calculated by comparing the integrated signal power within a time window of 0.1 μs over multiple locations. The average noise power was then subtracted from the total signal power.

Stent reverberation experiments with IVUS element

The aim of these experiments was to determine the effect of harmonic imaging on multiple echoes from a reflective stent in the near field of an US beam of an unfocused conventional IVUS element. T2 could rotate around the needle axis to simulate the rotation of an IVUS catheter (fig. 3.1). T2 was inserted in the circular expanded metal stent. We acquired the US signals in curved scan planes by rotating (angular spacing of 1°) and translating (lateral spacing of 50 μm) the IVUS element parallel to the needle axis.

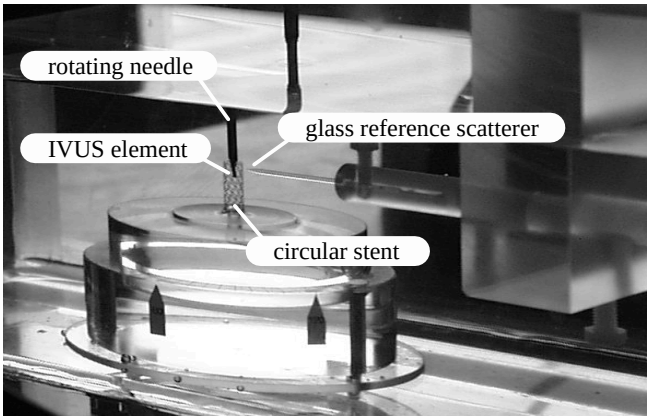

Figure 3.1: Experimental setup with rotating IVUS needle, circular expanded stent and glass point scatterer.

Next, the envelope was calculated and the maximum value within a time window was used to plot C-scans of the stent reverberations.

Imaging behind stent experiments with IVUS element

Clinically, it is of interest to image closely behind a reflective stent. A potential improvement may be obtained with a second harmonic field, in this circumstance. The aim of these experiments was to determine the effect of THI on images of a point reflector located closely behind a reflective stent strut. The flattened stent was positioned perpendicular to the beam axis of T2 at a distance of 1, 2 and 3 mm. At 400 µm behind the flattened stent, a 50-µm diameter glass fiber point reflector was located. We moved this reflector to nine different locations relative to a horizontally orientated stent strut to study the acoustic shadow created by the stent strut in fundamental and harmonic modes. We acquired B-scans in the direction of the long axis of T2 with a spacing of 20 µm.

Stented phantom experiments with IVUS element

We constructed a tissue-mimicking phantom to show its effect on the stent artefact appearance in THI mode. An expanded circular stent was inserted in the vessel phantom with an inner diameter of 4 mm. By rotating T2 within the stented phantom in steps of 1° over 120° in total, B-scans of one third of a full cross-section were acquired.

3.3 Results

Beam profile experiments

In water, the measured fundamental peak pressure at focus of T1 was 3.4 MPa when this transducer was driven by a 20 MHz excitation pulse and an amplitude of 120 volts peak-to-peak (V_{pp}). Lateral planes in F20, F40 and H40 modes, at focus (13 mm from T1) and at half the distance to focus (6.5 mm from T1), can be seen in fig. 3.2. The dynamic range of each image is normalized with respect to the maximum signal at focus of the corresponding mode. The diffraction patterns at half the distance to focus and at focus do not exhibit a great deal of structure due to the use of a wide band width transmit pulse. The measured beam widths of the fundamental 20 MHz beam at −3-dB, −6-dB and −20-dB were 130 µm, 180 µm and 470 µm, respectively. The harmonic the 40-MHz field showed narrower beam widths at the −3-dB, −6-dB and −20-dB thresholds of 80 µm, 120 µm and 300 µm, respectively. The fundamental 40-MHz beam width measurements are close to those of the harmonic 40 MHz, namely, 80 µm, 120 µm and 330 µm,

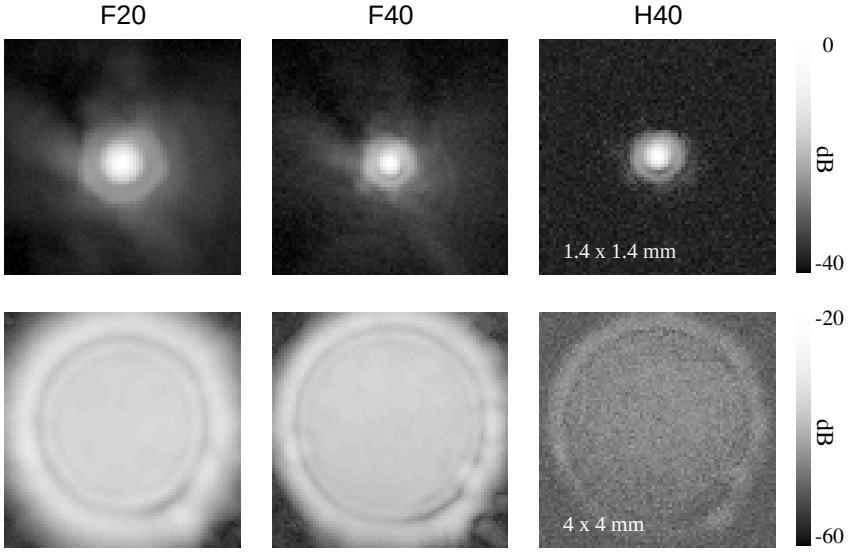

Figure 3.2: Lateral planes at focus (top) and at half the distance to focus (bottom) of the spherical PVDF transducer in both fundamental (F20 and F40) and harmonic (H40) modes. The images are normalized to the maximum signal at focus. The pressure levels of the envelope corresponding to 0 dB are 3.2, 2.2 and 0.57 MPa for the F20, F40 and H40 images respectively. A different spatial scale is used in both image rows.

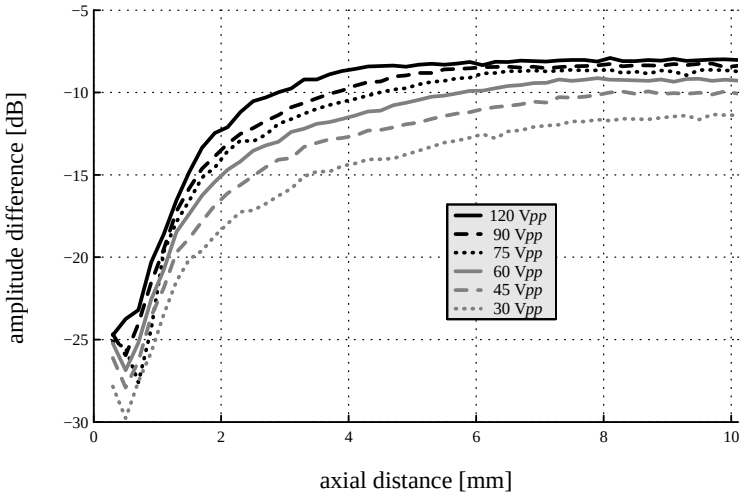

Figure 3.3: On-axis ratios of second harmonic (H40) to fundamental pressure (F20) of the unfocused elliptical-shaped IVUS transducer at six different excitation amplitudes (50% bandwidth pulses).

respectively.

The maximum on-axis fundamental peak pressure of T2 was 1.3 MPa and the maximum on-axis second harmonic pressure was 0.3 MPa, as measured with a 20-MHz pulse and an amplitude of 90 V_{pp}. Figure 3.3 shows the on-axis ratio of second harmonic to fundamental pressure at six different amplitudes. This figure shows the dependence of harmonic generation on fundamental amplitude.

Axial planes in F20, F40 and H40 modes are depicted in fig. 3.4. The dynamic range of each image is normalized with respect to the maximum signal within each image plane and covers a 40-dB range. The H40 beam shows less signal power in the near field close to the transducer surface, compared with both F20 and F40 modes. Furthermore, the H40 beam exhibits lower side lobe levels.

Stent reverberation experiments with PVDF transducer

The presence of a stent in the near field of the high-frequency beam caused reverberations (multiple echoes between the transducer and the stent) resulting in image quality

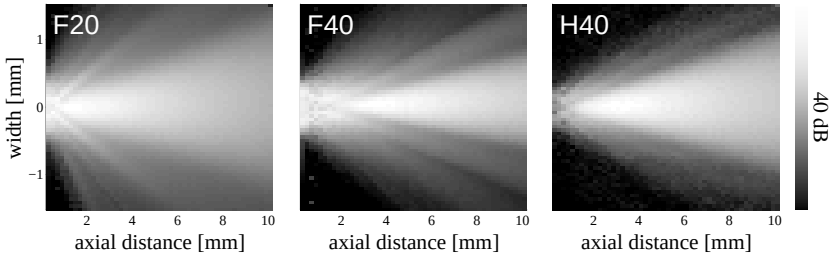

Figure 3.4: Measured axial beam profiles of the unfocused elliptical-shaped needle mount IVUS transducer, in both fundamental (F20 and F40) and harmonic (H40) modes. The images are normalized to the maximum signal at focus. The pressure levels of the envelope corresponding to 0 dB are 1.3, 1.4 and 0.3 MPa for the F20, F40 and H40 beam respectively.

degradation. When the stent was located at half the distance to focus, the energy arrival of the second reverberations from the stent coincided with the echo from the reference scatterer positioned at focus. In both F20 and F40 modes, the point scatterer signal could not be resolved because of the presence of stent reverberations (fig. 3.5). However, the use of the H40 mode made the point scatterer detectable. The reduction of the stent reverberations using the H40 mode has been assessed by comparing signal power in F20, F40 and H40 modes. Table 3.1 shows the signal strength of the reference scatterer relative to the reverberation signal in the three different modes. It can be seen that, in the case of both the 25% and 50% band width pulses, the stent reverberations in the H40 mode have been reduced by 14 dB and 12 dB compared with those in the F20 and F40 modes.

Table 3.1: Difference between signal power of reference scatterer (integrated over 25 locations) and signal power of stent reverberations (integrated over 400 locations) in both fundamental and harmonic modes and at different band widths.

	Fractional band width	
Imaging mode	25%	50%
F20	3.0 dB	1.7 dB
F40	4.3 dB	4.1 dB
H40	17.0 dB	15.5 dB

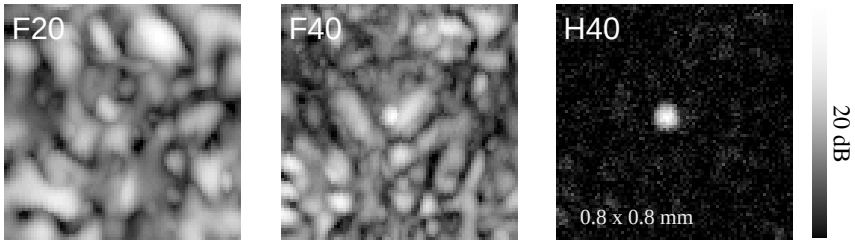

Figure 3.5: Imaging with the spherical PVDF transducer of a point scatterer at focus and a distorting stent halfway to focus, in both fundamental (F20 and F40) and harmonic (H40) modes. The images are individually normalized to the maximum signal in each image.

Stent reverberation experiments with IVUS element

C-scans were acquired when the circular expanded stent was located at different axial distances from the T2 transducer face (0.5, 0.75, 1.0 and 1.25 mm). Figure 3.6 shows C-scans of the first and second echoes of the stent located at a depth of 0.75 mm in F20, F40 and H40 modes. These images have been normalized with respect to the maximum signal in the first stent echo. The geometric pattern of the stent can be appreciated in the first echo and, to a lesser extent, in the second echo. The H40 image of the first echo image shows larger gaps between the individual stent struts. When the gap area is defined by an intensity level below -25 dB within the rectangular box (top row of fig. 3.6), the gap area relative to the F20 beam has been increased in both F40 and H40 modes, by 255% and 330%, respectively. The narrower H40 beam with reduced side lobes caused this improvement over the F40 beam at a distance of 0.75 mm from the transducer. The appearance of the second echo from the stent looks similar in the three imaging modes.

Imaging behind stent experiments with IVUS element

B-scan images show a different appearance with the different imaging modes of the glass point reflector echo behind a highly reflective stent strut. For example, fig. 3.7 shows B-scans of the reflections of two stent struts at a distance of 2 mm away from the transducer in all three imaging modes. The lower three images show the echo from the point reflector located at a position 200 μm away, compared with the upper three images. Arrows indicate the echo of the point reflector. These images are normalized to the maximum stent reflection per image and the dynamic ranges are similar. The point reflector signal in F20 mode is weak compared with that of both the F40 and H40 modes. There is no significant difference in appearance of the point reflector echo in H40 mode

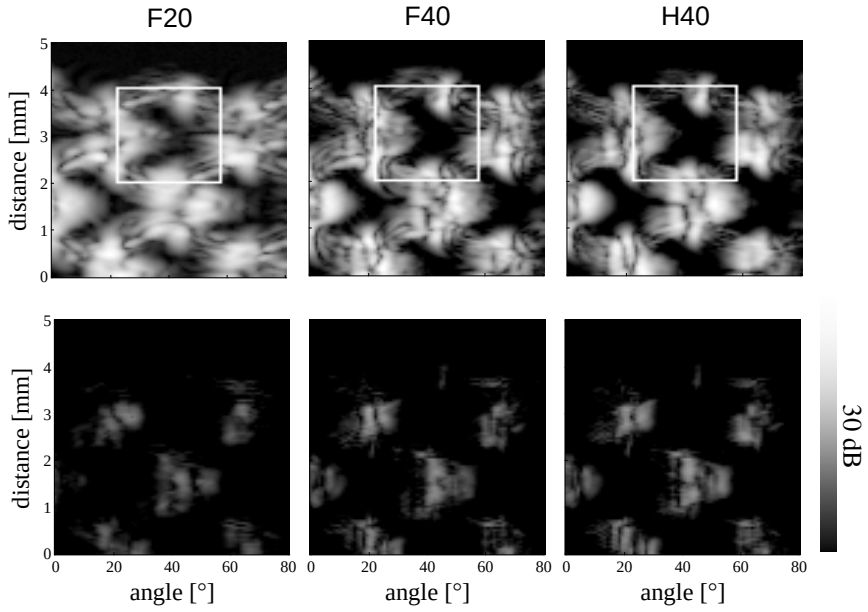

Figure 3.6: C-scans of the first (top) and second echo (bottom) from a circular expanded stent located at 0.75 mm away from the IVUS element, in both fundamental (F20 and F40) and harmonic (H40) modes. The images are individually normalized to the maximum signal in each image.

compared with that in F40 mode.

Stented phantom experiments with IVUS element

Images acquired with the rotating needle mount IVUS element within the tissue phantom are depicted in fig. 3.8. The stent is located at a distance of about 1 mm away from the transducer. These images are normalized to the maximum stent reflection in each image and the dynamic ranges are the same. The brightest regions indicate the first echoes from the stent struts and the less-intense speckle pattern is caused by the scattering of carborundum particles. The F20 image suffers more from a wider beam and side-lobes and this is shown in the region of the stent reflections and by an overall larger speckle size. It is also notable that the decay of signal strength as a function of depth is less pronounced in H40 mode than in the F20 and F40 modes. This is consistent with hydrophone results, and is a function of the combined effects of attenuation and nonlinear signal build-up during propagation. Furthermore, the diffraction effects in the proximity of the stent reflections in the H40 mode are not significantly different from those in the

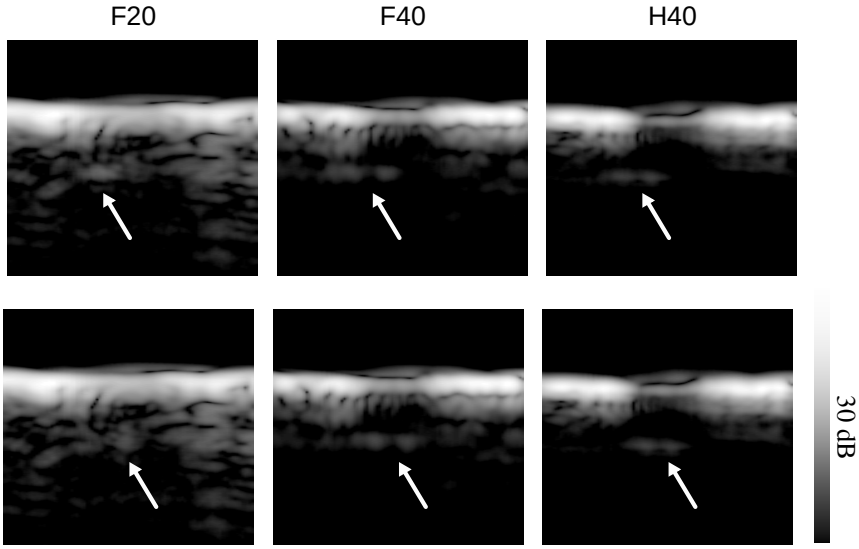

Figure 3.7: B-scans of a glass point scatterer located at two different positions behind two stent struts, in both fundamental (F20 and F40) and harmonic (H40) modes. The lower image row shows the echo from the point reflector located at a position 200 µm to the right compared to the upper row. The arrows indicate the echo from the point scatterer. These images are individually normalized to the maximum stent reflection in each image.

F40 image.

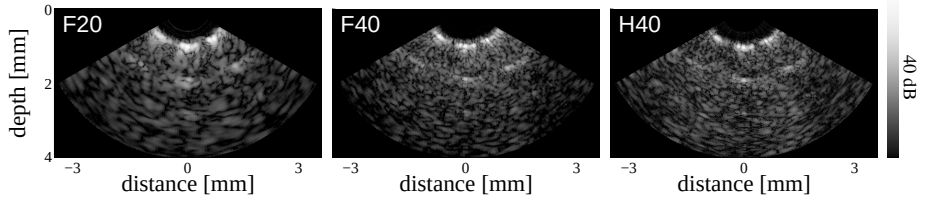

Figure 3.8: B-scans over 120° of a stented vessel phantom, acquired with a rotated IVUS element, in both fundamental (F20 and F40) and harmonic (H40) modes. These images are individually normalized to the maximum signal in each image.

3.4 Conclusion and discussion

An experimental setup was developed to image in both fundamental (20 and 40 MHz) and second harmonic modes (40 MHz) with two different transducers operating in pulse-echo mode. It was shown that THI could reduce image artifacts from a reflective stent in the near field of a focused high-frequency US beam, but not significantly in the case of an unfocused intravascular US beam compared with fundamental imaging modes.

The fundamental and second harmonic beams of both a spherically focused PVDF transducer (typically used for UBM) and a small elliptically-shaped unfocused IVUS element were evaluated. The H40 −6-dB beam width at focus of the focused transducer is 120 µm, which is a small fraction of the 8-mm aperture. The second harmonic pressure at 6.5 mm from the transducer was 35 dB below peak pressure at focus. The H40 −6-dB beam width of the main lobe of the unfocused IVUS element is the narrowest, up to 2.5 mm from the transducer, compared with both F20 and F40 beams. From 2.5 mm, the main lobe of the F40 beam (−6-dB) is narrower. The main lobe of the second harmonic beam rapidly builds up by 15 dB over a distance from 0.3 to 3 mm from the transducer face.

Whereas the reduction of the unwanted second echo using THI with the 8-mm aperture PVDF transducer is clear, the reverberation reduction with the small IVUS transducer is not significant. Qualitative measurements showed different appearances of stent artifact reduction in H40 mode between the two transducers. One reason is the different second harmonic beam shape of both transducers. Another reason for the different reverberation appearance may be the spatial scale of the individual stent struts relative to the local beam width of the transducers. A stent strut covers a larger beam area in the near field of the IVUS transducer than in the near field of the relatively large focused transducer.

Although this study showed that a conventional IVUS transducer could generate and detect a second harmonic beam through water and phantom material, the advantages of THI in stent artifact imaging are not obvious for this element. The stent reverberation experiment suggested that it was easier to delineate the first stent echo in THI mode when the stent was located at 0.75 mm. The smaller −6-dB beam width of the H40 beam in the near field might support this suggestion. The results of the well-controlled experiment where an individual scatterer was positioned closely behind a stent strut were not sufficient to show the potential for THI to look just behind a stent. The more realistic experiment in the stented phantom showed that it could be hard to distinguish between stent artifacts and tissue signal. Hence, it is difficult to see differences in stent artifact appearance between the different modes.

THI might be a straightforward way to improve IVUS imaging. However, a potential

difficulty with the implementation of THI is the increased attenuation of US in biologic fluids and tissues at higher frequencies (Duck, 1990). Because the second harmonic generation is partially dependent on the amplitude of the fundamental pressure wave and is always lower than the fundamental pressure level, it is not obvious that a detectable level of second harmonic signal could be generated and received. As a result of the low signal level and the influence of high-frequency RF noise in our experiments, it was beneficial to use averaging to increase the dynamic range of the second harmonic acquisitions.

In most of the experiments, we used water as the propagation medium. The acoustic nonlinearity parameter B/A (Hamilton and Blackstock, 1998) of water is lower than the B/A in biologic tissue (5.5 compared to 5.5 to 11 of biologic tissue) (Duck, 1990), which has the effect of reducing the generation of harmonics. However, the attenuation in the 20 to 40-MHz range is lower in water than in biologic tissues (Foster et al., 2000b), which has the effect of increasing the accumulation of propagation harmonics.

In addition to analog and digital band-pass filtering, pulse inversion (PI) was used to cancel out fundamental frequency signals present in the second harmonic frequency range. When short fundamental pulses are transmitted (relative band width $\geq 50\%$), the second harmonic axial resolution can benefit substantially from the use of PI. Therefore, it is not necessary to have a strict separation between transmit and receive band widths as used in another study by Cherin et al. (2002).

In conclusion, this study showed a reduction of stent artifacts with a focused PVDF transducer using THI. This effect could improve imaging in UBM applications where reflective objects in the near field degrade image quality. The effect of THI on the appearance of stent artifacts imaged with an IVUS element was not significant. Although one of our results indicated an improved delineation with THI of a stent close to an IVUS element, it remains to be seen if these improvements have the potential to tangibly enhance IVUS performance in clinical circumstances where reflective targets, such as protective sheaths, stents or calcified materials, are present in the very near field.

Chapter 4

Intravascular ultrasound Tissue Harmonic Imaging in vivo

Based on the publication *"Intravascular Ultrasound Tissue Harmonic Imaging In Vivo"*
by Frijlink M.E., Goertz D.E., van Damme L.C.A., Krams R. and Van der Steen A.F.W.,
IEEE Trans Ultrason Ferroelec Freq Control *in press*

Abstract – Tissue Harmonic Imaging (THI) might be used to improve image quality in Intravascular Ultrasound (IVUS). In this study we constructed a prototype IVUS system that could operate in both fundamental frequency and second harmonic imaging modes. This system uses a conventional continuously-rotating single-element IVUS catheter and was operated in fundamental 20 MHz, fundamental 40 MHz, and harmonic 40 MHz modes (transmit 20 MHz, receive 40 MHz). Hydrophone beam characterization measurements demonstrated the build-up of a second harmonic signal as a function of increasing pressure. Imaging experiments were conducted in both a tissue-mimicking phantom and in an atherosclerotic animal model *in vivo*. Acquisitions of fundamental 20 and 40 MHz and second harmonic acquisitions resulted in cross-sections of the phantom and a rabbit aorta. The harmonic results of the imaging experiments showed the feasibility of intravascular THI with a conventional IVUS catheter both in a phantom and *in vivo*. The harmonic acquisitions also showed the potential of THI to reduce image artifacts compared to fundamental imaging.

4.1 Introduction

Although THI has been shown to be able to suppress stent imaging artifacts when high frequency THI (transmit f_c = 20 MHz, receive f_c = 40 MHz) was applied *in vitro* (see

chapter 3. However, results of THI in any IVUS application with a conventional rotating IVUS catheter in phantoms or *in vivo* have not been reported.

In this study the feasibility of THI with a conventional single-element continuously rotating IVUS catheter is investigated. We developed and characterized a prototype IVUS system to operate in either fundamental or second harmonic imaging mode. The fundamental and second harmonic on-axis pressures of this IVUS catheter were measured and compared with simulated results. Next, the frequency response of the IVUS element was assessed. We finally performed THI with a rotating IVUS catheter in both a tissue phantom and an atherosclerotic rabbit aorta *in vivo*.

4.2 Materials and Methods

System description

A prototype IVUS system (see section 2.3) was developed to operate in either fundamental imaging mode for 20 to 40 MHz center frequencies, or in second harmonic imaging mode of a 20 MHz transmit frequency. Individual components of this prototype system are described in section 2.2.
We used a conventional rotating single-element IVUS catheter (Princeps 4.3F CCS, DuMED, Rotterdam, the Netherlands) consisting of an elliptical shaped unfocused element (long axis 1 mm, short axis 0.75 mm) with a center frequency of approximately 30 MHz. This element was used in pulse-echo mode for fundamental 20 MHz (F20) and 40 MHz (F40) acquisitions and second harmonic acquisitions at 40 MHz (H40) from a fundamental 20 MHz pulse. The catheter was mechanically rotated by a motor unit that was modified to permit rotational speed control, as well as to enable the transmission of controlled catheter input signals and the collection of received signals.

In fundamental 20 MHz mode, the received signals were band-pass filtered using an analog 3–70 MHz band-pass filter (5^{th} order Butterworth) to remove any DC-offset and high frequency noise outside the frequency range of interest. For F40 and H40 acquisitions, a 31–51 MHz band-pass filter (5^{th} order Butterworth) was used. The dynamic range of the H40 acquisitions was improved by this filter due to suppression of the high amplitude fundamental 20 MHz signal.

System characterization

Characterization measurements and nonlinear simulations were conducted to determine the potential for the IVUS system to perform THI with a conventional single-element catheter. A broadband hydrophone and XYZ-positioning system (section 2.2) were used

to estimate the one-way frequency response and to measure the fundamental and second harmonic pressures.

frequency response measurement

After a careful alignment procedure of the catheter with respect to the hydrophone, we measured the one-way frequency response of the Du-MED catheter by transmitting Gaussian enveloped pulses with a fractional bandwidth of 10% at center frequencies ranging from 10 to 50 MHz at 2 MHz intervals. Narrow bandwidth pulses were used to increase the measurement accuracy of the frequency dependent sensitivity at individual frequency components. The on-axis response was measured over 10 mm at a measurement interval of 100 μm, to account for frequency dependent diffraction effects. For a flat, circular, piston transducer with a 0.45 mm radius, theory predicts the transition from near to far field to shift from 1.3 to 6.8 mm when the center frequency shifts from 10 to 50 MHz. The maximum signal response for each narrow bandwidth pulse frequency component was used to construct the one-way frequency response. The result was corrected for the frequency dependent response of the calibrated hydrophone and for the frequency dependent attenuation of water (0.002 dB/cm/MHz^2 (Duck, 1990)).

pressure measurements

The ability of a conventional IVUS catheter to generate sufficient pressure to build up a significant level of propagation harmonics is essential for THI. This was investigated with on-axis hydrophone measurements in water. The hydrophone was translated for 10 mm along the catheter beam axis with steps of 100 μm. We applied Gaussian enveloped pulses (f_c = 20 MHz) with a fractional bandwidth of 25% at six different driving voltages (30 to 180 volts peak-to-peak (V_{pp})), acquired the raw signals on-axis and extracted both the fundamental (F20) and second harmonic (H40) pressures by digital filtering (10–30 and 30–50 MHz, 5^{th} order Butterworth). For comparison purposes, we also measured the fundamental pressure at 40 MHz (F40) on-axis. The second harmonic generation as a function of different fundamental peak pressures can be estimated from these measurements as well. The measurements were corrected for the different hydrophone sensitivity at 20 and 40 MHz.

nonlinear simulations

Simulations were performed to confirm that the origin of the measured second harmonic field was associated primarily with nonlinear propagation as opposed to undesired 40 MHz transmission artifacts. Specifically, since propagation harmonics build up with distance, a comparison of simulation results and measured data close to the transducer can provide an indication if transmission artifacts are significant. On-axis pressure levels were modeled in F20, F40 and H40 modes for a flat, circular transducer element with

a diameter of 0.9 mm using a time domain implementation of the non-linear parabolic KZK-equation (Bouakaz et al., 2003). We then calculated the ratio of F40/F20 and H40/F20, since these ratios, compared with the same ratios from measurements, indicate whether the observed 40 MHz signal is primarily propagation harmonic or transmitted F40. The nonlinear parameter of the medium was set to 3.5 (B/A = 5), corresponding to the nonlinear coefficient of water (Duck, 1990). The amplitude of the pressure pulse at the transducer surface was set to 1.5 MPa, which is a realistic value that can generate a detectable level of propagation harmonics in water.

2D beam profile measurements

Two-dimensional beam profiles were made to measure the fundamental and second harmonic sound fields. These beam profiles are central to understanding potential image quality improvements in harmonic mode. Pressure levels of an extracted IVUS element were measured in an axial scan plane to characterize the fundamental (F20 and F40) and harmonic (H40) sound fields in water. This extracted IVUS element was mounted on a needle without a protective sheath that normally surrounds the catheter's element and therefore allowed for hydrophone measurements very close (<1 mm) to the transducer surface. Since propagation harmonics (at 40 MHz) are anticipated to build up relatively fast from the transducer surface, which is in contrast with direct transmission at 40 MHz, measuring very close to the transducer element enables you to detect the origin of the 40 MHz signal. Gaussian enveloped pulses with a fractional bandwidth of 50% were used. The scans were spatially sampled at 200 µm intervals in the axial direction and at 50 µm intervals in the lateral direction over a length of 10 and 3 mm respectively. After data acquisition, the maximum of the envelope (as calculated using the Hilbert transform) was used to plot beam profiles.

Imaging

The prototype IVUS system was configured for THI with a conventional continuously-rotating single-element IVUS catheter. Experiments were performed in both a tissue-mimicking phantom and in a rabbit model *in vivo*. A catheter rotation speed of 5 rotations per second was used in these imaging experiments and we acquired approximately 2400 RF-lines per rotation. This corresponds to a Pulse Repetition Frequency (PRF) of 12.5 kHz, which is lower than the theoretical maximum PRF of a rotating single-element IVUS system of about 100 kHz as limited by sound propagation speed. Although no physical limitations exist to apply and acquire 2400 lines per rotation at a rotation speed of 30 rotations per second, practical limitations of our power amplifier and PC-digitizer prohibited the use of a higher PRF. The high line-density of 2400 lines per rotation limited decorrelation of neighboring lines, thereby allowing pulse inversion (PI) methods to suppress fundamental signal in the second harmonic acquisitions (Hope Simpson et al., 1999). Pulse inversion was implemented by alternate transmission of a pulse (0° phase)

and its inverted counterpart (180° phase) for successive lines. Therefore the summation of two neighboring RF-lines (with an inter-pulse angle of 0.15°) resulted in significant fundamental suppression.

Another advantage of the high line-density is that averaging of the highly correlated neighboring lines could be used to increase the signal-to-noise ratio (SNR). In all imaging experiments we averaged four RF-lines to create a single image line, resulting in final images consisting of 600 lines. For all these experiments Gaussian enveloped pulses (25% bandwidth) at center frequencies of either 20 MHz or 40 MHz were generated. This corresponded to pulse lengths of 0.2 and 0.1 μs, for 20 and 40 MHz respectively, resulting in an expected axial resolution of 300 and 150 μm. Although 25% bandwidth is on the low side for imaging, the overlap between the fundamental and second harmonic signals in the frequency domain is limited. H40 signals were isolated using a combination of PI and analog filtering (see system description). After acquisition, digital band-pass filtering was applied between 10–30 MHz (3^{rd} order Butterworth) in F20 mode and 30–50 MHz (3^{rd} order Butterworth) in F40 and H40 mode, was used to reduce broadband noise. There has been no time-gain-compensation (TGC) to compensate for the depth dependent signal decay. All images are log compressed in order to increase the depicted dynamic range.

tissue phantom

Initial imaging experiments were conducted using a tissue-mimicking phantom. The material used is a mixture of 8% gelatin (Type A, Sigma Chemical company, St Louis, MO), 2% agar-agarose (Agar Agar CMN, Boom, Meppel, the Netherlands) and 1% carborundum powder with a particle size in the range of 3–10 μm (Cats import, Hoogvliet, the Netherlands) diluted with distilled water. The velocity and attenuation of this phantom material used at IVUS frequencies have been studied by de Korte et al. (1997). The lumen diameter within the phantom material was approximately 4 mm. Cross-sectional images were acquired in F20, F40 and H40 modes. The SNR was estimated by calculating the ratio of integrated RF-power of a signal-rich region adjacent to the lumen-tissue boundary and RF-power in a signal-poor region within the water lumen.

rabbit aorta

In vivo THI was performed using a New Zealand White rabbit animal model for atherosclerosis. Briefly, atherosclerosis is induced in this model through a combination of balloon induced endothelial cell injury in the lower abdominal aorta, followed by an 8 week high cholesterol (2%) diet as described by Schaar et al. (2005). An angiographic overview of the infra-renal aorta was performed and radiopaque markers were located subcutaneously to indicate the previously denuded region. Subsequently, an IVUS pullback (40 MHz, Boston Scientific) was done at the location of the denuded segment in order to

locate regions of interest. Following the extraction of the Boston Scientific catheter, the Du-MED catheter was advanced through a 5 French (Fr) sheath through the iliac artery to the region of interest. Images of cross-sections of the abdominal aorta were formed in F20, F40 and H40 modes. Following euthanasia of the rabbit (Euthasate®, 3 ml/kg), the abdomen was opened, and two markers were placed on the aorta. The distance between both markers was measured before and after removal to correct for shrinkage. Eight-micrometer thick cross-sectional slices from the excised aorta were used for histology. All experiments were performed in accordance with institutional regulations and the "Guiding for the care and use of laboratory animals" published by the US as approved by the Council of the American Physiological Society. The SNR in the different imaging modes was estimated by calculating the ratio of integrated RF-power over a signal-rich region (~0.7 mm wide and 1.5 mm deep) and integrated RF-power of a signal-poor region at a location were no echoes were evident on the image.

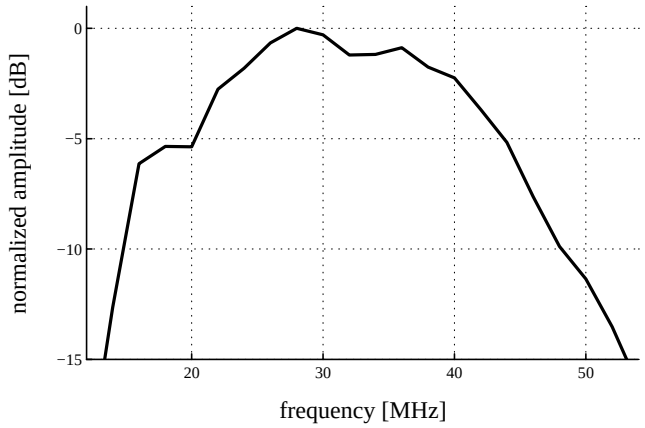

Figure 4.1: One-way frequency response of single-element IVUS Du-MED catheter.

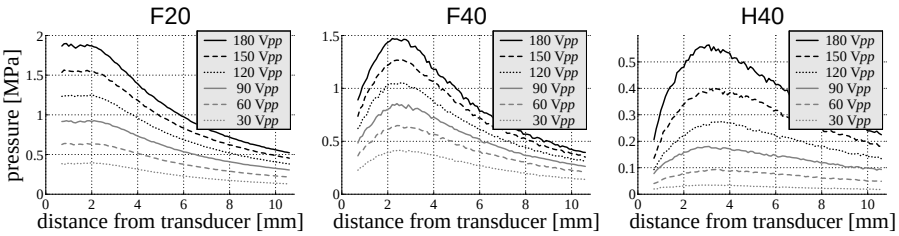

Figure 4.2: On-axis maximum F20, F40 and H40 pressures of a single-element Du-MED catheter at six different excitation amplitudes as measured with a 75-micron-diameter hydrophone.

4.3 Results

System characterization

frequency response measurement

The normalized one-way frequency response of the Du-MED catheter is plotted in fig. 4.1. The −3-dB (one-way) bandwidth of the IVUS catheter was 19 MHz, with the highest sensitivity at a frequency of approximately 28 MHz. The sensitivity at 20 and 40 MHz was 5 and 3 dB below the highest sensitivity, therefore this catheter can be used in the 20 to 40 MHz range for second harmonic imaging.

pressure measurements

Fundamental (F20 and F40) and second harmonic (H40) pressures were measured on-axis for six different excitation amplitudes (fig. 4.2). At a transmit amplitude of 180 V_{pp}, the Du-MED catheter generated a fundamental peak pressure of 1.9 MPa at 20 MHz at approximately 2 mm from the transducer surface. The measured fractional bandwidth (−6 dB) of these pulses was 23%. The second harmonic signal in water built up to 0.55 MPa, corresponding to 11 dB below the fundamental peak pressure. The on-axis H40 signal reached its maximum further from the transducer than the F20 signal, namely between 3 and 4 mm. Figure 4.2 indicates that the IVUS catheter is also able to transmit at 40 MHz. The decay of the F40 in the far field of the beam is faster than that of the H40 field. The relative level of second harmonic generation increases with higher fundamental amplitudes. This is also seen in fig. 4.3, which shows the second harmonic pressure level relative to the fundamental pressure level on-axis for the six different excitation voltages of this catheter. The increasing H40/F20 ratios clearly show the building up of the second harmonic during propagation in water. Close to the transducer at 0.5 mm, the H40 signal is lower than 19 dB below the F20 level for all excitation amplitudes. At the highest excitation amplitude, the H40 pressure on-axis built up to

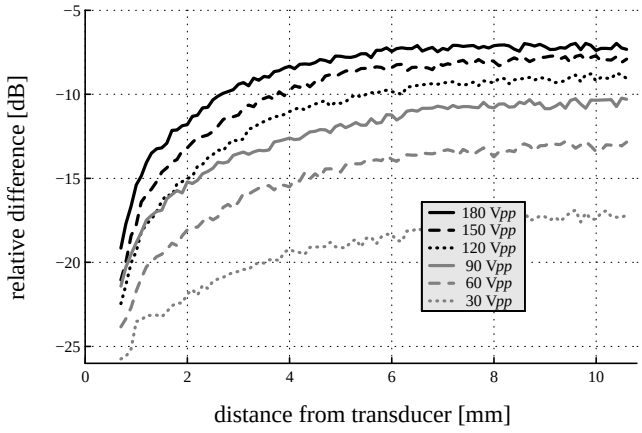

Figure 4.3: On-axis ratios of H40 / F20 of single-element Du-MED catheter at six different excitation amplitudes.

8 dB below the F20 pressure.

nonlinear simulations

Simulated H40/F20 and F40/F20 ratios are compared to hydrophone measurements of the extracted element in fig. 4.4. The on-axis build up of H40/F20 is in reasonable agreement with the theoretical predictions: a steep increase of the H40/F20 ratio occurs close to the transducer. The simulated F40/F20 ratio undergoes fluctuations close to the transducer (< 3 mm) due to the near-field diffraction patterns of both F20 and H40. These fluctuations are missing in the measured F40/F20 ratio, but the trend is similar: the F40/F20 ratio close to the transducer (< 1 mm) is only 5 dB less than the maximum ratio at > 8 mm. The propagation second harmonic is generated as high as 8 dB below fundamental in both simulation and measurement. This comparison indicates that transmission of 40 MHz signal by the element itself in H40 mode is not significant.

2D beam profile measurements

2D beam profiles of the extracted IVUS element in F20, F40 and H40 were measured in a plane perpendicular to the catheter axis (fig. 4.5). The dynamic range of each image is normalized with respect to the maximum detected within each image. The H40 beam shows less signal power in the near field (< 2 mm) compared to both F20 and F40

modes. The H40 beam is also the narrowest of these three beams close to the transducer surface, though beyond 3 millimeters, the F40 beam is narrower. At an axial distance of 2 mm from the transducer for example, the −6-dB beamwidths of the F20, F40 and H40 beams were 560, 480 and 300 µm respectively. At 4 mm from the transducer, these −6-dB beamwidths were 720, 350 and 500 µm respectively. Furthermore, the H40 beam exhibits lower side lobe levels than both fundamental beams.

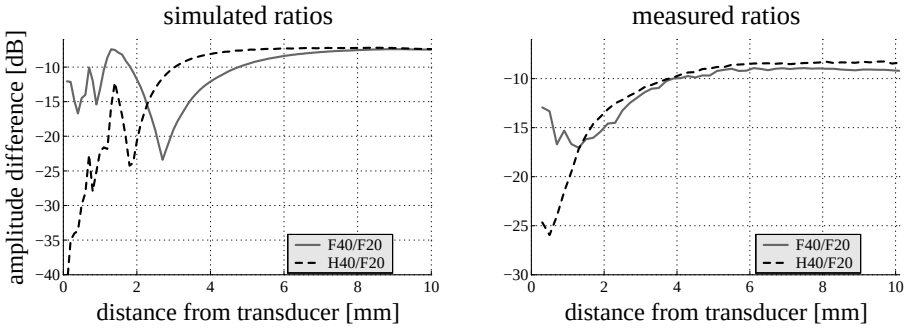

Figure 4.4: Simulated and measured on-axis ratios of transmitted 40 MHz / fundamental 20 MHz and propagated 40 MHz / fundamental 20 MHz.

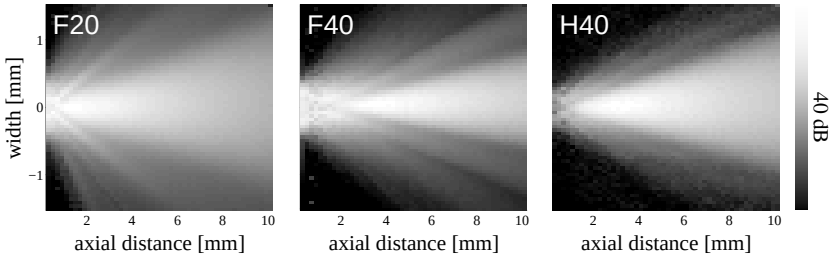

Figure 4.5: Two dimensional beam profiles of the unfocused extracted catheter element in both fundamental (F20 and F40) and harmonic (H40) modes. The images are individually normalized to the maximum signal in each image.

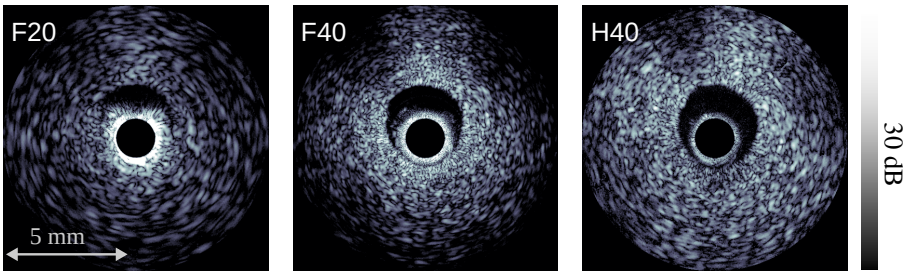

Figure 4.6: Cross-sections of a tissue-mimicking phantom acquired in F20, F40 and H40 mode. The displayed images have been normalized with respect to the maximum tissue signal within the individual images.

Imaging

tissue phantom

Figure 4.6 displays cross-sections of the tissue-mimicking phantom at the same location in F20, F40 and H40 modes. The images have been normalized with respect to the maximum phantom signal within the individual images and the same dynamic range is employed. Close to the catheter (< 2 mm), the image quality is poor due to two primary factors. First, there is saturation of the receive amplifier due to coupling with the transmitted pulse. Second, the protective sheath surrounding the rotating transducer gives rise to reflections and reverberations within the near field of the ultrasound beam. These image artifacts appear strongest in the F20 image. The speckle size in the F40 and the H40 acquisition are similar, while the F20 image shows larger speckles. This is also expected, since the lateral beamwidth and pulse length of the F20 beam is larger than those of the H40 and F40 beams. The pulse length of the H40 is intermediate between the F20 and F40 pulse lengths. The shadows appearing in all three images at approximately 11 and 2 o'clock are due to the protective sheath, which suffers from angle-dependent attenuating differences, possibly caused by thickness or shape variations. The H40-image is acquired after an excitation pulse of 150 V_{pp} (at the output of the high power amplifier) and the SNR of this image is approximately 19 dB.

rabbit aorta

Cross-sections of an atherosclerotic rabbit aorta acquired in F20, F40 and H40 modes are shown in fig. 4.7. Again, the images have been normalized with respect to the maximum signal level in the individual images. The images indicate the contour of the vessel wall and surrounding structures. The structure between 4 and 6 o'clock is presumed to be the vena cava. Figure 4.8 depicts a Hematoxylin and Eosin (HE) staining, showing the

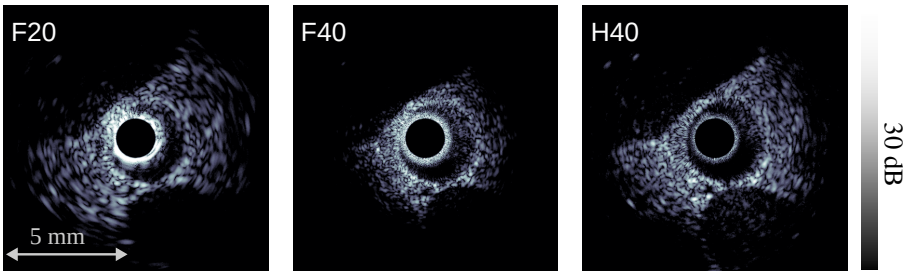

Figure 4.7: Cross-sections of an atherosclerotic rabbit aorta acquired in F20, F40 and H40 mode *in vivo*. These images are normalized with respect to the maximum signal level in the individual images.

histology of the same area. The plaque, intima and media contours are indicated, and a plaque thickness of approximately 400 µm can be appreciated. In the F20 ultrasound image in fig. 4.7, the plaque area is difficult to distinguish due to sheath reflections. However between 12 and 5 o'clock, the less dense speckle pattern in the lumen of the F40 and H40 image is consistent with the detection of plaque. The combined effect of amplifier saturation and reflections of the surrounding sheath, visible close to the transducer, is the least present in the H40 acquisition compared to both fundamental acquisitions. The latter emphasizes the advantage of reducing acoustic energy in the near field through the use of the harmonic beam. The estimated SNR of the H40 acquisition is approximately 25 dB, while the SNR of the F40 mode is approximately 35 dB as in both images four RF-lines were averaged to increase the SNR.

4.4 Discussion and conclusion

A prototype IVUS system was developed and used to demonstrate the feasibility of IVUS THI both in a phantom and *in vivo*. Image cross-sections of a tissue mimicking phantom and an atherosclerotic rabbit aorta were compared in fundamental mode at 20 and 40 MHz as well as in harmonic mode at 40 MHz.

The increasing H40-to-F20 ratio of the on-axis measurement corresponded well with the KZK-simulation results of the modeled transducer element. However, the simulation showed a near field ratio with more extremes than that were measured. This discrepancy may be due to several factors. Firstly, the finite aperture of the sensitive area of the needle hydrophone results in spatial averaging, while the simulation calculated the pressure of an infinitely small point. Secondly, we measured the response of an elliptical shaped transducer, while we simulated a circular one. Finally, the model assumed a uniform

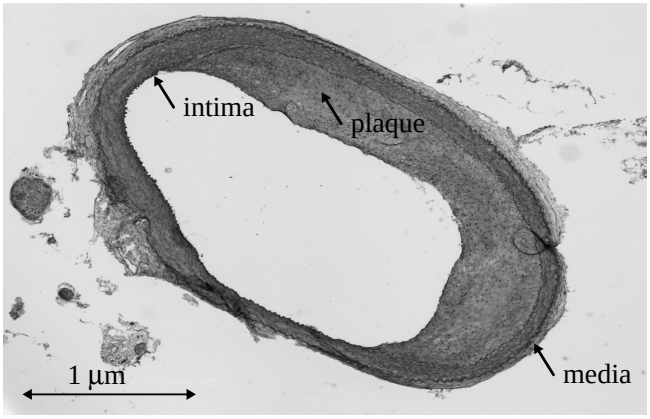

Figure 4.8: HE-staining of an 8 µm thick cross-section of an aorta from an atherosclerotic rabbit model.

pressure distribution over the transducer surface, while this might not be true.

Initial imaging experiments showed that it was possible to form H40 images of both a tissue phantom and a rabbit aorta *in vivo*. The different SNR of the H40 acquisitions was because of different medium characteristics between the tissue phantom and the rabbit aorta *in vivo*. The homogenous tissue phantom has a constant nonlinearity parameter (B/A), and uniform linear scattering and attenuation, while the rabbit aorta consists of multiple inhomogeneous media with different characteristics. Attenuation and nonlinearity values for different biological media can be found in Duck (1990). Although the combination of the limited dynamic range and the averaging in the H40 acquisition prohibited the visualization of blood scattering, it is expected that blood scattering levels as compared to tissue scattering is similar in F40 acquisitions.

Although the objective of this study was to show the feasibility of intravascular THI, the H40 results of the phantom and *in vivo* imaging experiments also showed the potential of THI to reduce image artifacts compared to fundamental imaging. The combined effect of amplifier saturation and the reflective sheath surrounding the catheter element, displayed as a white ring close to the transducer in fig. 4.6 and 4.7, is less prominent in the harmonic acquisitions. This could be linked with the 2D beam profiles in fig. 4.5, showing a relatively lower near-field energy in the H40 beam compared to both fundamental beams. It is also notable that the decay of signal strength as a function of depth (fig. 4.6 and 4.7) is less pronounced in H40 mode than in the F20 and F40 modes. This is also consistent with the hydrophone results (see fig. 4.5). In *in vivo* experiments the signal

decay of the harmonic acquisition will be a function of the combined effects of beam diffraction and tissue properties (B/A, and frequency dependent attenuation). Indeed, it is possible that these effects may conceivably result in a superior effective penetration depth in H40 mode than in F40 mode. This has been investigated with simulations in chapter 7.

The combination of analog filtering, high line-density and PI achieved effective fundamental suppression in harmonic acquisitions in a rabbit aorta. It can be anticipated however, that in human coronary arteries the harmonic acquisitions may suffer more from catheter and tissue motion.

In conclusion, this study showed the feasibility of intravascular THI *in vivo* with a conventional single-element rotating IVUS catheter. The use of THI has the potential to improve IVUS image quality and this might improve future clinical use of IVUS in patients with a cardiovascular disease.

Chapter 5

Transducer for harmonic intravascular ultrasound imaging

Based on the publication *"Transducer for Harmonic Intravascular Ultrasound Imaging"* by Vos H.J., Frijlink M.E., Tesselaar E., Goertz D.E., Blacquière G., Gisolf A., de Jong N. and Van der Steen A.F.W., IEEE Trans Ultrason Ferroelec Freq Control, 52(12):2418–2422, 2005.

Abstract – A recent study has shown the feasibility of tissue harmonic imaging (THI) using an intravascular ultrasound (IVUS) transducer. This correspondence describes the design, fabrication, and characterization of a THI optimized piezoelectric transducer with oval aperture of 0.75 mm by 1.0 mm. The transducer operated at 20 MHz and 40 MHz, and was comprised of a single piezoelectric layer with additional passive layers. The Krimholtz-Leedom-Matthaei (KLM) model was used to iteratively find optimal material properties of the different layers. The transducer characterization showed −6-dB fractional bandwidths of 30% and 25%, and two-way insertion losses of −20 dB and −36 dB, respectively.

5.1 Introduction

It is known that image artifacts may be reduced with tissue harmonic imaging (THI). Since the generation of the second harmonic signal is approximately proportional to the square of the local fundamental frequency pressure (Duck, 2002), less harmonic energy

is present close to the transducer at which image artifacts occur mostly (Cherin et al., 2002). This beneficial effect comes at the cost of lower signal levels of the harmonics, which can be overcome by carefully designing the ultrasonic transducer for harmonic imaging (Saitoh et al., 1995; Takeuchi et al., 2002).

Initial studies have shown the feasibility of THI in IVUS imaging (chapter 3), but these were carried out with transducers that were not optimized for THI. Various fundamental and harmonic imaging transducers for diagnostic medical high-frequency ultrasound are described in literature (Meyer et al., 1999; Cherin et al., 2002; Zhou et al., 2003), mostly based on PVDF and lithium niobate. However, compared to PZT ceramics, these materials have a low dielectric constant, which results in a bad electric match to conventional 50 ohm electronics if the element size is small. Reported IVUS transducers (Foster et al., 1991; Oralkan et al., 2002; Knight and Degertekin, 2003) have not been optimized for harmonic imaging yet.

In this study, a PZT-based single element IVUS transducer is developed with increased sensitivity at two frequency bands at about 20 MHz and 40 MHz. The design and fabrication process of this dual frequency element are described. Finally, the transducer was characterized by its transfer function, electrical impedance and insertion loss.

5.2 Methods and fabrication

design

The purpose of the transducer imposes several design constraints. The center frequency of the transmission pulse was chosen to be 20 MHz, resulting in a second harmonic pulse with a center frequency of 40 MHz. These frequencies are thought to give a good trade-off between axial resolution (which increases with frequency) and penetration depth (which reduces with frequency due to increased acoustic attenuation). As the transducer is mounted inside a catheter tip with 1.3 mm outer diameter (4 Fr), the aperture should not exceed 0.75 mm by 1.0 mm. The matching layers should be electrically conductive to facilitate connection of the electrodes. Based on these constraints, a design was made consisting of a single disc of piezoelectric material and two passive layers for frequency tuning and improved acoustic impedance matching (fig. 6.1). An additional passive layer is sandwiched between the sound-absorbing backing material and the piezoelectric layer and acts as a so-called mismatching layer, increasing the power transmission efficiency in the forward direction. The transducer was modeled with the one-dimensional KLM model, which was extended with acoustic and electric energy loss (Foster et al., 1991; Lethiecq et al., 1993; Kino, 1987). In order to optimize the transducer for harmonic imaging, a multidimensional, nonlinear minimization algorithm (Nelder-Mead simplex method) was implemented. Basically this minimization algorithm searches for the thick-

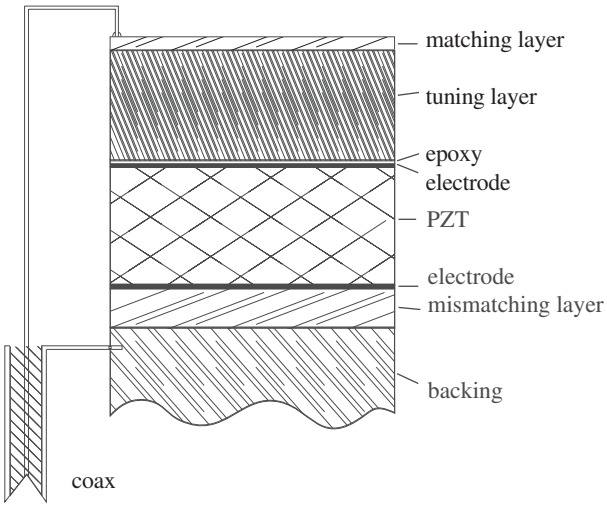

Figure 5.1: Schematic drawing of the transducer. All passive layers are electrically conductive for easy connection. The transducer is elliptical with axes of 0.75 mm and 1.0 mm.

ness of the active layer and the thickness and acoustical impedances of the passive layers that maximize the transmission efficiency and the reception sensitivity. This search was associated with the following cost function

$$\chi = -\log\left\{T_f^2(f_0)\right\} - \log\left\{T_f^{-1}(f_0)\right\} \tag{5.1}$$

with T_f the ratio of the output acoustic force and the source voltage, T_f^{-1} its reception inverse and f_0 the fundamental frequency (20 MHz). We assumed that the maximum allowed transmission voltage is limited by health care regulations. And due to the squared dependency of the harmonic pressure generation on the fundamental pressure, the cost function relies on the squared transmission function. Logarithms were used for faster convergence. Material properties of fine-grain, high-pressed PZT (PPK22, Stelco GmbH, Neumarkt, Germany) were inserted in the model. This material was chosen for its low loss at high frequencies (mechanic loss factor of 0.02 and electric loss factor of 0.03 at 20 MHz), and has a thickness mode coupling coefficient of 0.42 and a relative clamped dielectric constant of 850. Based on the available electrically conductive materials (see section "transducer fabrication"), the acoustic impedance of the backing was set to 7 MRayl and the acoustic impedance of the mismatching layer was set to 4 MRayl. The optimized layer properties based on the extended KLM model are given in Table 6.1. The optimal transducer surface is 1.1 mm^2, but the size restrictions of the

Table 5.1: Optimal Simulated Values of Material Properties [1]

Layer	Thickness [µm]	Velocity [m/s]	Impedance [MRayl]	Loss factor [–]
matching layer	11 (7)	1500 *	4 (4)	0.05 *
tuning layer	64 (59)	6400 *	27 (22)	0.01 *
piezoelectric layer	71 (67)	5000 *	40 *	0.02 *
mismatching layer	14 (21)	1500 *	4 *	0.05 *

[1]Asterixed (*) numbers were manually inserted in the model and kept fixed during the optimization. el-
The optimal values for the design including an adhesive film are depicted between parentheses.

ement resulted in a maximum area of 0.6 mm^2 (elliptical aperture with 0.75 mm and 1.0 mm axes). Simulations showed that this aperture reduction increases the two-way insertion loss with less than 2 dB. The depicted sound velocities and loss factors are measured values of the available materials, on which the prototype is based (see section "transducer fabrication").

transducer fabrication

A 0.5 mm thick disk of PZT was manually lapped and polished to the appropriate thickness and electroded with a 100 nm nickel film. The tuning layer was made from an aluminum foil (measured impedance of 17 MRayl), rolled to the appropriate thickness and bonded with two-component epoxy (AY103 and HY951, Ciba Specialty Chemicals, Basel, Switzerland) under pressure on the front side of the PZT layer. The thickness of the epoxy layer was estimated to be 0.5 µm, based on the assumption that the surface roughness of the polished and electroded PZT limits the epoxy layer thickness. It is hypothesized that the peaks of the nickel electrode penetrate through the epoxy layer to make contact with the aluminum layer, thus maintaining electric conductivity. The surface roughness was measured with a 0.1-µm resolution surface roughness instrument (Mitutoyo SJ-301, Mitutoyo American Corporation, Aurora, IL), and showed peak-to-peak values of about 1.0 µm. The layer thickness is estimated at half the peak-to-peak distance, because we expect half the interstitial volume filled with the PZT and half the volume filled with the epoxy. Simulations indicated that the epoxy layer changes the optimal values for the layer properties; the new values are given between parentheses in Table I. The matching layer and the mismatching layer consisted of 45–55% mass percentage mixed silver- and carbon-filled conductive ink (SS477 RFU and SS427, Acheson Industries, Erstein, France) and had a measured acoustic impedance of 5 MRayl. The

backing consisted of silver-filled, electrically conductive epoxy (EccoBond 66C, Emerson and Cuming, Westerlo, Belgium), which has an acoustic impedance of 7 MRayl. Multiple prototype elements were laser-cut into ovals with axes of 1.0 mm and 0.75 mm and mounted on a catheter tip. For the characterization experiments, this tip was attached to a steel tube with an outer diameter of 0.9 mm. Both sides of the transducer were connected to the coaxial cable (Pico-coax PCX 44 K 11, Grandwill Axon, China), and the element was poled with an electric field of 25 kV/cm at room temperature.

characterization

The electric impedance of the transducer in air was measured with a vector impedance analyzer (HP 4193A, Hewlett-Packard, Palo Alto, CA) before the cable was attached. The fabricated transducer material values were checked with the use of a curve-based fit of the KLM model implementation to the measured electric impedance in air, in which the sum of squared differences between the measured and modeled impedances was minimized. The Nelder-Mead simplex method was used to vary the input parameters. The layer properties thickness, acoustic impedance, and loss factor, together with the piezoelectric coupling factor and a serial loss resistance, were updated. Based on the found fit, the expected transfer function and two-way insertion loss of the transducer in water were calculated with the model. The pressure transfer function of the transducer was measured using a hydrophone. The transducer was driven by a 10 V, single peak amplitude signal using the experimental setup as described in section 2.2. To improve the signal-to-noise ratio (SNR) for the frequency range of interest (10 MHz to 50 MHz), three separate 100% fractional bandwidth, Gaussian-enveloped pulses with center frequencies of 20 MHz, 30 MHz, and 40 MHz were applied. A needle hydrophone (section 2.2) was placed on-axis at 4.0 mm distance from the transducer, which is the theoretical natural focal distance at 40 MHz. The received signal was digitized at a sample rate of 400 MHz and averaged over 400 pulses. The pressure transmission transfer function was calculated by the ratio of the hydrophone received spectrum, and the AWG driving spectrum and was compensated for by the calibrated hydrophone sensitivity characteristics. For efficiency measurements in a pulse-echo configuration, signals were redirected with a passive diode expander/limiter with a two-way signal loss of 12 dB, for which compensation was performed. A flat stainless steel reflector was placed at 3.3 mm distance parallel to the transducer surface. The transmission pulses were similar to those in the hydrophone measurements and had a 5.0 V single peak amplitude. The received pulse was averaged over 1000 repetitions. The two-way insertion loss was calculated by the ratio of the received signal spectrum and the amplifier signal spectrum. The measured transfer function and insertion loss were compared with the simulated functions of the modeled transducer with optimized values and with those resulting from the curve-based fit to the electric impedance. To account for the diffraction effects and water attenuation in the model, we used a numerical approach based on the Rayleigh-Sommerfeld integral

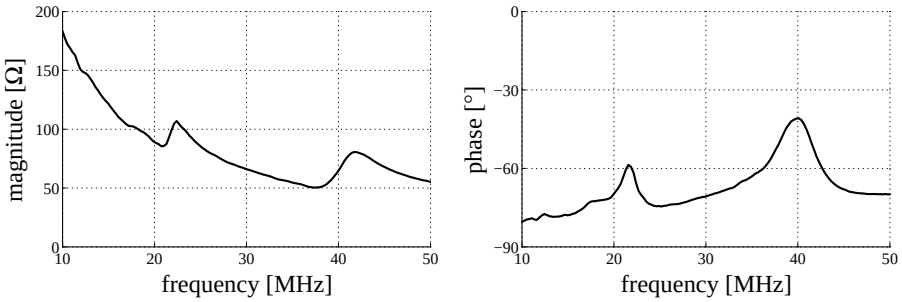

Figure 5.2: Magnitude (left) and phase (right) of the measured electric impedance of the transducer in air.

(Kino, 1987) to calculate the spatial impulse response of the transmitter/receiver setup. In this method, the integral is approximated by a sum over small (<1/100 λ^2) surface elements on both the transmitting and receiving flat surfaces, and the received pressure is the average over the small elements of the receiving plane. The acoustic damping in water is $25{\cdot}10^{-3}$ Np/MHz^2/m in water at 20°C (Duck, 1990), for which compensation was performed in the simulations.

5.3 Results

Figure 5.2 shows the measured electrical impedance of the element in air. The values found with the curve-based fit showed deviations smaller than 20% of the values from Table I. The passive electric loss resistance was 16 ohm, which was mainly caused by the relatively low electrical conductivity of the mixed silver and carbon layers (about 5 ohm per layer). The phase plot shows a peak at 22 MHz and 40 MHz. The fact that the lower-frequency peak is not exactly at 20 MHz is attributed to uncertainties associated with the modeling of the epoxy layer between the PZT and the aluminum layer. Figure 5.3 shows the measured and modeled transfer functions of the transducer at 4.0 mm. It is a graph composed from the three different pulses as described before, plotted in bins with ranges of 10-25 MHz, 25-35 MHz, and 35–50 MHz. The transmission transfer function again shows peaks at 22 MHz and at 40 MHz, with −6-dB fractional bandwidths (BW) of 30% and 25%, respectively. The agreement of the modeled transfer function based on the curve-based fit and the measured transfer function is very good. However, the curve-based calculated pressure is lower than the modeled optimized transducer pressure, which we hypothesize to be due to two factors. First, simulations showed that the epoxy layer can cause unwanted reverberations between layers as it becomes thicker. This resulted in a reduction of 3 dB of the transmit efficiency for the specified bonding

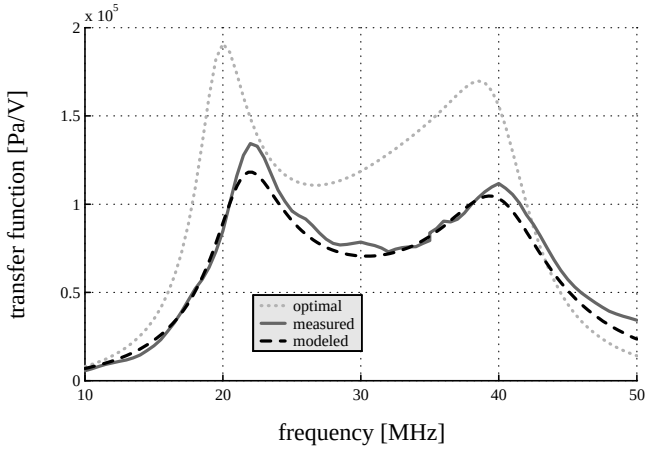

Figure 5.3: Measured, modeled and the optimal transfer functions of the transducer at 4.0 mm distance in water. Water attenuation and diffraction are incorporated in the modeled functions.

layer. Second, the other factor might be the electric resistance of the transducer, causing heat production, which resulted in 2 dB energy loss in simulations. The modeled optimized transducer showed 40% and 35% BW of about 20 MHz and 40 MHz, respectively. Figure 5.4 shows the measured and modeled two-way insertion loss of the transducer. The modeled insertion loss from the curve-based fit and the measured one show good agreement up to 25 MHz and an increasing difference between 25 and 45 MHz of up to 12 dB. Again, the epoxy layer (6 dB, two-way loss) and the loss resistance (4 dB, two-way loss) are hypothesized to give the differences between the optimized simulated design and the calculated insertion loss based on the curve-based fit. Additionally, in the measurements, a suboptimal alignment of the reflector might give undesired diffraction effects, which are absent in the beam profile simulations. Electric tuning effects due to the expander/limiter also might give reverberations, resulting in frequency-dependent interference attributed to the measured insertion loss. Unfortunately, we are not able to quantify these influences, but we only can suspect them to give the differences between the model based on the electrical impedance fit and the measured two-way insertion loss.

5.4 Discussion

An ultrasound transducer optimized for harmonic IVUS has been designed, built, and characterized. The modeled optimized properties of the transducer layers were found with an extended version of the KLM model combined with a nonlinear minimization

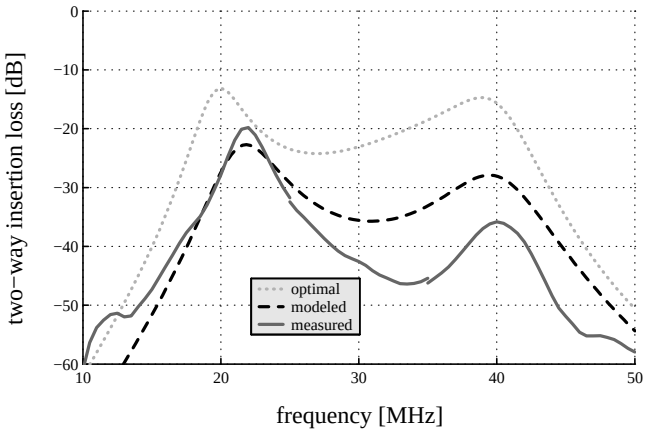

Figure 5.4: Measured, modeled and the optimal two-way insertion loss of the element, with a flat steel reflector at 3.3 mm distance. Water attenuation and diffraction are incorporated in the modeled functions.

algorithm. The prototype showed a −6-dB fractional bandwidth of about 20 MHz of 30%, which should be sufficient for a short pulse. The most efficient transmit frequency of the current prototype appeared to be 22 MHz instead of 20 MHz. This frequency could be tuned in future transducers to 20 MHz by increasing the thickness of the aluminum layer in the design.

The mismatching and the matching layers are the main causes of electrical energy loss, reducing the efficiency and increasing the risk of transducer overheating in a catheter setup. Using a backing material with lower acoustic impedance, which would eliminate the need for a mismatching layer, could alleviate this problem. This material also could be used for the front matching layer.

The surface area of the prototype is smaller than the most optimal surface area, resulting in an electric mismatch between the transducer and the electrical equipment. However, additional simulations showed that this gave a two-way insertion loss increase of about 2 dB, which is negligible compared to the losses described above.

Chapter 6

Harmonic intravascular ultrasound imaging with a dual-frequency catheter

Based on the publication *"Harmonic Intravascular Ultrasound Imaging with a dual-frequency catheter"* by Frijlink M.E., Goertz D.E., Vos H.J., Tesselaar E., Blacquière G., Gisolf A., Krams R. and Van der Steen A.F.W., Ultrasound Med Biol *in press*

Abstract – Recent studies have shown the feasibility of Tissue and Contrast Harmonic Imaging with a prototype nonlinear Intravascular Ultrasound (IVUS) system using a conventional single-element rotating IVUS catheter. In this study, a dual-frequency transducer element was mounted in an IVUS catheter and its second harmonic imaging performance was investigated and compared with that of a conventional IVUS catheter. Hydrophone measurements showed a transmit efficiency improvement of >6 dB for the dual-frequency catheter at 20 MHz. *In vitro* phantom experiments showed a signal-to-noise ratio improvement of >5 dB in second harmonic mode at 40 MHz (H40) with the dual-frequency catheter, when using equal transmit voltage for both catheters. Finally, *in vivo* experiments were conducted and showed improvements in H40 imaging with respect to the conventional IVUS catheter.

6.1 Introduction

The feasibility of THI using a 20–40 MHz mechanically-rotated IVUS catheter was demonstrated *in vivo* in chapter 4. The relatively low-amplitude second harmonic sig-

nals resulted in a limited signal-to-noise ratio (SNR).

Nonlinear intravascular contrast agent imaging has been examined in chapter 8. Another application is intravascular targeted contrast agent imaging (Goertz et al., 2005b).

Harmonic imaging is facilitated by transducers with efficient transmission and sensitive reception at different frequency regimes. This approach has been examined extensively at lower ultrasound frequencies (Hossack et al., 2000; Bouakaz et al., 2002). For high frequency diagnostic ultrasound, a variety of transducer designs incorporating different materials (fiber composite, piezo-polymer, single-crystal and piezo-ceramic) have been studied for fundamental frequency imaging (Meyer et al., 1999; Foster et al., 2000a; Snook et al., 2002). High frequency harmonic imaging would be improved by a high sensitivity over a wide bandwidth. Although polyvinylidene-fluoride (PVDF) transducers generally benefit from a low acoustic impedance and high bandwidth, the electromechanical properties are poor, especially for small transducers (Foster et al., 2000a; Snook et al., 2002). A lead zirconate titanate (PZT) transducer with a double-peak-type frequency characteristic was developed for harmonic and subharmonic imaging at lower frequencies (Takeuchi et al., 2002). This design consisted of an active layer of the sensitive piezo-ceramic PZT and of a passive tuning layer. Recently, a transducer for intravascular harmonic imaging, showing a frequency response with two peaks around 20 and 40 MHz, has been designed, fabricated and characterized (chapter 5). The feasibility of employing such an element in a functional IVUS catheter has yet to be examined.

In this study we improved this "dual-frequency" transducer element and mounted it in a commercial IVUS catheter. The performance of this dual-frequency catheter in THI mode (transmit f_c = 20 MHz, receive f_c = 40 MHz) was investigated and compared to a conventional IVUS catheter (f_c = 30 MHz). Imaging experiments were performed both in a tissue mimicking phantom and in an atherosclerotic rabbit aorta *in vivo*.

6.2 System description

The prototype harmonic IVUS imaging system has been described in section 2.3. Analog band pass filters were used to pass the receive second harmonic signal and reduce the overall noise level (31–51 MHz, 5^{th} order butterworth and 13–60 MHz, 5^{th} order butterworth). The received signal was digitized at 200 MHz using the 12-bit A/D PCI-card (section 2.2).

The custom-made IVUS element was designed to have a dual-frequency characteristic, with increased sensitivity around 20 and 40 MHz. The fabricated element was based on a design consisting of a single disc of piezoelectric material and two passive layers for frequency tuning and improved acoustic impedance matching (chapter 5). All passive

layers are electrically conductive to facilitate electrical connectivity. However, the transducer element used for mounting on an IVUS catheter differed in two respects from the previously reported design in chapter 5. Firstly, the aluminum tuning layer, attached with a second layer of conductive adhesive, was replaced by a single layer of electroplated tin. In this way, the additional electrical resistance of the adhesive layer was eliminated. The high electrical resistance of this adhesive layer could cause considerable heating within the transducer during excitation, which eventually resulted in reduced performance or malfunction. Simulations using the KLM-model showed that the difference in acoustic impedance between aluminum (~17 MRayl) and tin (~26 MRayl) did not result in a significant decrease in sensitivity (2–3%). The second aspect that is different from the original design is that the mismatching layer between the piezoelectric layer and the absorbing backing material was omitted. This mismatching layer was originally intended to increase the power transmission efficiency in the forward direction. However at the cost of a small sensitivity drop of 1–2 dB at 20 and 40 MHz, omitting this extra layer increased the fractional bandwidths of the two frequency peaks at 20 and 40 MHz by approximately 25%. The simulated transmit efficiencies of this element at 20 and 40 MHz are approximately 40 and 50 kPa/V respectively. Fig. 6.1 depicts a schematic drawing of the transducer design and table 6.1 displays the thickness and acoustic impedance for the different layers. A laser-cut circular element with a diameter of 0.8 mm was delicately mounted on a mechanically-rotated single-element IVUS catheter (Du-MED, Rotterdam, the Netherlands) after the careful removal of the conventional transducer

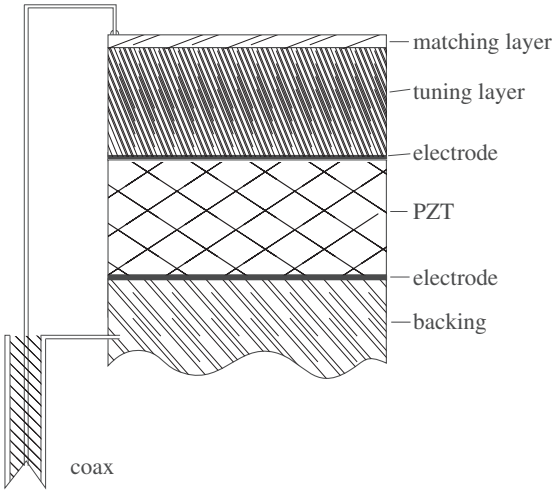

Figure 6.1: Schematic drawing of the transducer. All passive layers are electrically conductive.

Table 6.1: Layer Properties of Dual-frequency Transducer

Layer	Material	Thickness [µm]	Impedance [MRayl]
active layer	PZT	60	40
tuning layer	tin	36	27
matching layer	conductive ink	6	4

element. The wire bonding was performed after the attachment of the dual-frequency element to the transducer mounting substrate consisting of backing material on top of a curved metal substrate. The drive shaft of the catheter was mechanically rotated by a motor unit that was modified to permit rotational speed control as well as to enable the transmission of controlled catheter input signals and the collection of received signals.

6.3 Methods

Hydrophone measurements

A calibrated needle hydrophone (section 2.2) was used to measure the one-way frequency response of the dual-frequency catheter in distilled, degassed water. After a careful alignment procedure, Gaussian enveloped pulses with fractional bandwidths of 10% were transmitted at center frequencies ranging from 10 to 50 MHz at 2 MHz intervals. The on-axis response was measured over 10 mm at a measurement interval of 100 µm, to account for frequency dependent diffraction effects, as theory predicts that the transition from near to far field shifts from 1.1 to 5.3 mm when the center frequency shifts from 10 to 50 MHz for a flat, circular, piston transducer with a 0.4 mm radius. The maximum amplitude for each frequency component was used to construct the one-way frequency response. The result was corrected for the frequency dependent response of the calibrated hydrophone and for the frequency dependent attenuation of water (0.002 dB/cm/MHz^2) (Duck, 1990).

On-axis fundamental pressures have been measured for both a conventional IVUS catheter (Princeps 4.3F CCS, Du-MED, Rotterdam, the Netherlands) and the dual-frequency catheter when excited by an identical Gaussian shaped 20 MHz pulse (fractional bandwidth = 25%) with the same amplitude. The conventional catheter consisted of an elliptical unfocused element (long axis 1.0 mm, short axis 0.75 mm) with a center frequency of approximately 30 MHz. The on-axis response was measured as a function of range at 100 µm intervals from 1 to 10 mm from the transducer face.

Imaging experiments

THI experiments were performed with the prototype harmonic IVUS system using a continuously-rotating dual-frequency IVUS catheter. To compare the ability of the dual-frequency catheter and a conventional IVUS catheter to generate and detect propagation harmonics, imaging experiments were performed in both a tissue-mimicking phantom and in a rabbit model *in vivo*. In both types of imaging experiments, we acquired 2400 RF-lines per rotation at a rotation speed of 5 frames per second, as limited by our IVUS system. Due to this high line-density, the decorrelation between neighboring lines was low, thereby allowing pulse inversion methods (Hope Simpson et al., 1999) to suppress fundamental signal in the second harmonic acquisitions (Goertz et al., 2004). This also permitted the use of averaging of neighboring lines in order to increase the signal-to-noise ratio (SNR).

Gaussian shaped 20 MHz pulses (fractional bandwidth = 25%, phase = 0° and 180° for alternate RF-lines) with equal amplitude were used to excite both catheters. The harmonic 40 MHz signals (H40) (i.e. the second harmonic of 20 MHz pulses) were acquired and images were created by means of pulse inversion and averaging. The SNR was improved by combining four (*in vivo*) and eight (phantom) neighboring RF-lines respectively, resulting in final images consisting of 600 and 300 lines respectively. The SNR for the images was estimated by calculating the ratio of integrated RF-power over a signal-rich region-of-interest and over a "noise-only" region/acquisition.

The tissue mimicking phantom is a combination of 8% gelatin (Type A, Sigma Chemical company, St Louis, MO), 2% agar-agarose (Agar Agar CMN, Boom, Meppel, the Netherlands) and 1% carborundum powder with a particle size in the range of 3–10 μm (Cats import, Hoogvliet, the Netherlands) dissolved in distilled water (de Korte et al., 1997) and had a lumen diameter of 4 mm.

In vivo THI was performed using a New Zealand White rabbit animal model for atherosclerosis. Atherosclerosis is induced in this model through a combination of balloon induced endothelial cell injury in the lower abdominal aorta, followed by an 8 week high cholesterol (2%) diet (Schaar et al., 2005). Cross-sectional images of the abdominal aorta were formed in H40 mode. All experiments were performed in accordance with institutional regulations and the "Guide for the care and use of laboratory animals" (NRC, 1996).

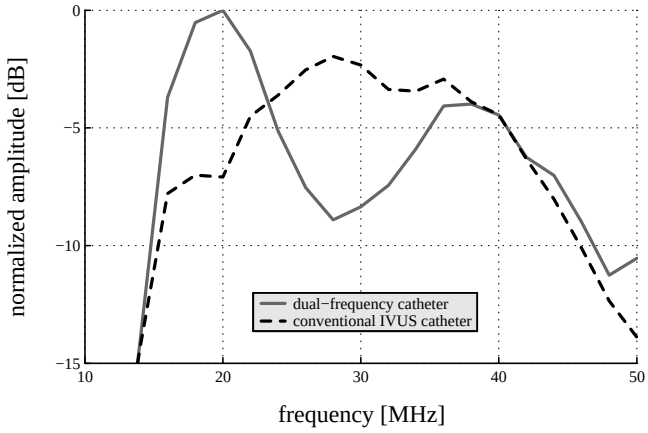

Figure 6.2: One-way frequency responses of the dual-frequency and conventional IVUS catheter.

6.4 Results

Hydrophone measurements measurement

The one-way frequency responses of the dual-frequency catheter and the conventional IVUS catheter are plotted in fig. 6.2. Their responses have been normalized with respect to the peak sensitivity of the dual-frequency catheter. Two sensitivity peaks at 20 and 40MHz can clearly be identified. The sensitivity of the dual-frequency catheter around 20 MHz is >6 dB higher than that of the conventional catheter, indicating an improved transmit efficiency when transmitting at 20 MHz, while around 40 MHz both catheters show a similar sensitivity.

Absolute pressure levels as generated by both catheter types and measured on-axis are given in fig. 6.3. Obviously, the dual-frequency catheter generates approximately twice as much fundamental pressure as a conventional catheter when both catheters were excited with an identical pulse.

Imaging experiments

Figure 6.4 displays cross-sections of the tissue-mimicking phantom in H40 mode, as acquired with the dual-frequency and the conventional IVUS catheter. The displayed images have been normalized with respect to the maximum tissue signal within the im-

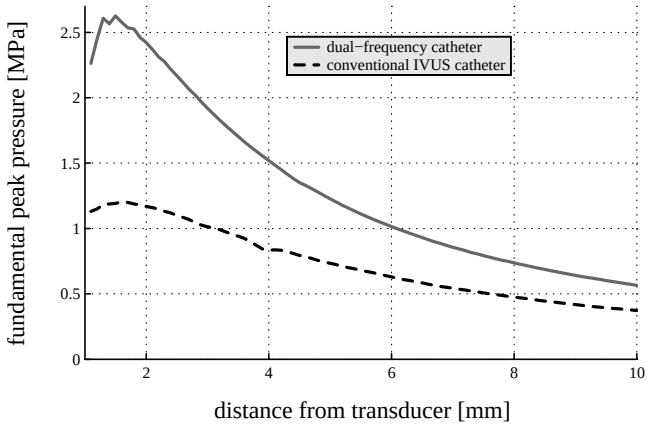

Figure 6.3: On-axis fundamental peak pressures (F20) of the dual-frequency and conventional IVUS catheter.

age acquired with the dual-frequency catheter (right panel). The signal power in both acquisitions has been compared to the noise power in acquisitions in water only (with both catheters). The SNR of the averaged H40 signal as acquired with the conventional IVUS catheter (left panel) was 15 dB, while the SNR of the dual-frequency acquisition

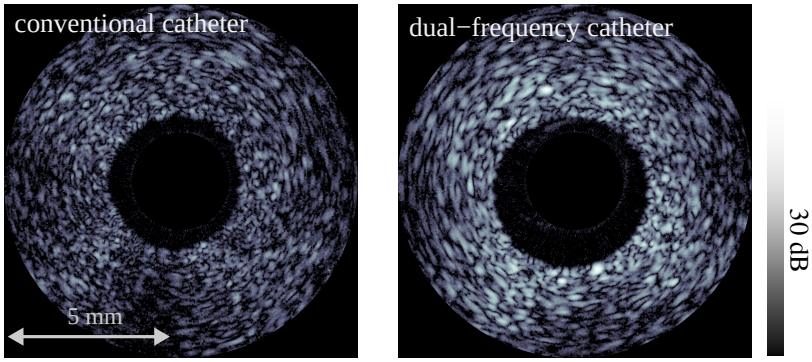

Figure 6.4: Cross-sections of a tissue mimicking phantom acquired in H40 mode with both a conventional and a dual-frequency IVUS catheter.

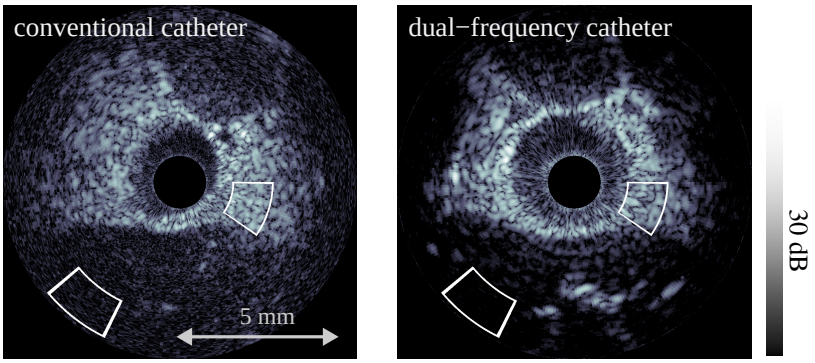

Figure 6.5: Cross-sections of rabbit aortas acquired in H40 mode with both a conventional and a dual-frequency IVUS catheter.

(right panel) was 21 dB.

Cross-sections of rabbit aortas acquired *in vivo* in H40 mode are shown in fig. 6.5. These images are normalized with respect to the maximum signal level in the individual images. The images indicate the contour of the vessel wall and surrounding structures. The structure at 1 o'clock in the left panel and at 12 o'clock in the right panel is the vena cava. Blood scattering is visible at these high ultrasound frequencies. The SNR is calculated by integrating and comparing the signal power in signal rich and signal poor regions indicated in fig. 6.5. The SNR of the H40 acquisition with the conventional catheter (left) is estimated to be 17 dB, while the SNR with the dual-frequency catheter (right) is estimated to be 30 dB. Although this SNR difference of 13 dB is considerable, careful interpretation is necessary since the aortas of two different animals were imaged.

6.5 Discussion and conclusion

A custom-made dual-frequency IVUS catheter was evaluated with a prototype Harmonic IVUS system under conditions relevant to tissue harmonic IVUS. Characterization experiments showed the dual-frequency catheter to have improved transmit efficiency at 20 MHz. Therefore, imaging experiments with this catheter under similar circumstances in both a tissue mimicking phantom and in rabbit aortas *in vivo* resulted in increased SNRs.

Since the dual-frequency element was designed to efficiently transmit 20 MHz pulses and sensitively detect 40 MHz harmonic signals, an increased SNR in H40 mode was anticipated provided that similar transmit conditions were used. The underlying as-

sumption is that the maximum possible excitation amplitude (determined by the depolarization and breakdown voltage) is equal for both catheters, since the thickness of the piezoelectric layer of both elements is in the same range (~74 μm versus ~60 μm). This was not explicitly verified experimentally for the elements used in this study. Since nonlinear propagation increases with increasing fundamental pressure (Averkiou and Hamilton, 1997; Hamilton and Blackstock, 1998; Duck, 2002), the maximum SNR for harmonic acquisitions is obtained for the highest fundamental pressure excitation where no depolarization, voltage breakdown or significant nonlinear transducer vibrations occur. Figure 6.3 shows that the fundamental peak pressure of the dual-frequency catheter is indeed much higher when identical voltages were applied.

While the focus of imaging experiments in this study was based on conditions relevant to tissue harmonic imaging, a dual-frequency transducer also has application potential in nonlinear contrast agent imaging. In chapter 8, a 40 MHz transmit frequency was employed to perform 20 MHz subharmonic contrast imaging. Provided that sufficient pressure levels could be generated on transmit at 40 MHz, an improved sensitivity at receive (20 MHz) would be advantageous. It was found that lower transmit pressure levels were required to improve contrast-to-tissue-ratios for second harmonic contrast imaging at IVUS frequencies, due to increasing propagation harmonics for increasing transmit pressures. In this case, a dual-frequency transducer with an improved sensitivity peak at 40 MHz would likely be advantageous. Tissue harmonic imaging applications would also benefit from an increased sensitivity at 40 MHz. Alternative design methods, such as those proposed in literature (Takeuchi et al., 2002) might be used to increase the peak sensitivity at the second harmonic frequency at the expense of the peak sensitivity at the fundamental frequency. Other designs which may result in sensitive transducers for harmonic IVUS could be based on ceramic/polymer composites or single-crystal materials (Snook et al., 2002).

Although the SNR in second harmonic acquisitions was shown to be higher with the dual-frequency catheter, other factors determining the image quality are also important. A significant factor is spatial resolution. The different appearance of the spatial frequency of the speckle patterns in fig 6.4 indicate a different spatial resolution for both catheters. The axial resolution could be different due to the different frequency responses. The fundamental pulse length will be influenced by this frequency response, leading to a potentially different second harmonic pulse length. Small differences in lateral resolution may be explained by the small difference in transducer dimensions; circular (0.8 mm) versus elliptically (0.75 $\times$ 1.0 mm). Future research will focus on these image quality determining factors when the dual-frequency element is mounted on current clinically used catheters.

The conventional IVUS catheter has not been optimally evaluated at fundamental 30 MHz

mode. Therefore, it is not appropriate to make conclusions about absolute SNR values in fundamental 30 MHz mode, or to compare second harmonic SNR values to fundamental SNR values. This study is primarily valid for comparing the SNR in harmonic mode between two different type IVUS transducers.

Element to element variability between individual catheters causes significant efficiency performance differences. We found sensitivity differences up to 3 dB for conventional catheters, which could only be partly explained by non-optimal alignment in the pressure measurements. Since only a few dual-frequency catheters have been made so far, no useful numbers can be given for these. However, it has experimentally been found that individual performances differ from catheter to catheter, and that the stability of the piezoelectric transducers decreases with age and duty time. Further optimization in the fabrication process might minimize the performance differences between individual catheters.

Chapter 7

Simulations on Tissue Harmonic Imaging with a single-element intravascular ultrasound catheter

Based on the publication *"A Simulation study on Tissue Harmonic Imaging with a Single-Element Intravascular Ultrasound Catheter"* by Frijlink M.E., Goertz D.E., Bouakaz A. and Van der Steen A.F.W., J Acoust Soc Am *in press*

Abstract – *In vivo* feasibility of tissue harmonic imaging with a mechanically-rotated IVUS catheter was experimentally demonstrated (chapter 4). To isolate the second harmonic signal content, a combination of pulse inversion (PI) and analog filtering was used. In this study the development of a simulation tool is reported to investigate nonlinear IVUS beams, and to evaluate the influence of transducer rotation and axial catheter-to-tissue motion on the efficiency of PI signal processing. Nonlinear beams were simulated in homogeneous tissue-mimicking media at a transmit frequency of 20 MHz which resulted in second harmonic pressure fields at 40 MHz. The competing effects of averaging and decorrelation between neighboring RF-lines on the signal-to-noise ratio (SNR) were studied for a single point-scatterer. When the transducer was rotated with respect to point-scatterers, simulating the acoustic response of tissue, the fundamental frequency suppression using PI degraded rapidly with increasing inter-pulse angles. The effect of axial catheter-to-tissue motion on the efficiency of PI seemed to be of less influence for realistic motion values. The results of this study will aid in the optimization of harmonic

IVUS imaging systems.

7.1 Introduction

In chapter 4 we demonstrated the feasibility of THI *in vivo* for an IVUS system using a 20–40 MHz mechanically-rotated IVUS catheter. In that study, tissue harmonic signals were isolated using a combination of analog filtering and pulse-inversion (PI).

The PI technique requires at least one firing of a pulse and its inverted counterpart along each line of sight (Hope Simpson et al., 1999). In the presence of relative motion between the tissue and catheter, the fundamental frequency signal (i.e. transmit bandwidth signal) is not completely canceled, and the harmonic intensity becomes smaller due to signal decorrelation. Motion artifacts of PI-based THI have been studied by Shen and Li (2002) whose results indicated that the performance of tissue harmonic imaging can be significantly affected by tissue motion. In particular it was found that for axial motion, both the fundamental reduction and the tissue harmonic intensity decreased much more rapidly than with lateral motion. This study was conducted under conditions relevant to low frequency array based scanning. These conditions depart significantly from the case of harmonic IVUS systems where a rapidly rotating single-element transducer is imaging in the presence of significant cardiac tissue motion.

Nonlinear ultrasound beams and their exploitation in the context of THI have been extensively investigated at lower diagnostic ultrasound frequencies (Duck, 2002; Humphrey, 2000; Averkiou et al., 1997). A number of different approaches have been developed to model nonlinear propagation in the field of an ultrasonic transducer. The most common technique is to solve the Khokhlov-Zabolotskaya-Kuznetsov (KZK) equation, which is a nonlinear parabolic equation that accounts for the combined effects of diffraction, absorption, and nonlinearity for directional sound beams (Hamilton and Blackstock, 1998). Comparisons of nonlinear simulation results and measurements show a very high level of agreement (Duck, 2002; Humphrey, 2000; Averkiou and Hamilton, 1997). For relatively short pulses, as typically used in diagnostic ultrasound, the time-domain implementation of the KZK equation is advantageous because many harmonic components could then be taken into account for the relatively broadband imaging pulses (Hamilton and Blackstock, 1998). At high frequencies, both nonlinear tissue properties and nonlinear ultrasound beams remain relatively unexplored.

In this study we simulated fundamental 20 MHz (F20), second harmonic (H40), and fundamental 40 MHz (F40) fields for an unfocused circular IVUS element using a two dimensional nonlinear parabolic KZK equation and medium characteristics (attenuation, nonlinearity, scattering) in the range of those of vascular tissue and blood. The pulse-echo responses from a single point-scatterer and a cloud of point-scatterers were

calculated for successive inverted pulses as the beam was rotated. The influence of rotation, and the effect of axial tissue-to-catheter motion on the performance of PI was then investigated for different inter-pulse angles.

7.2 Methods

Simulation design

nonlinear propagation

The proposed simulation method resembles the method as described by Li and Zagzebski (2000). The simulation of the transmitted nonlinear field by an unfocused circular transducer is based on a time-domain implementation of the KZK equation based on the numerical approach of Lee and Hamilton (1995). A two-dimensional implementation has been written in FORTRAN and has been evaluated (Bouakaz et al., 2003). The attenuation of acoustic waves propagating in a wide variety of lossy media obeys a power law dependence on frequency of the general form (Szabo, 1994),

$$\alpha = \alpha_0 |2\pi\nu|^{\gamma} \tag{7.1}$$

where ν is the frequency, and α_0 and γ are arbitrary real non-negative constants. Most biologic fluids and tissues have power law exponents in the $1 \leq \gamma \leq 2$ range (Duck, 1990). The algorithm described by Bouakaz et al. (2003) was modified to account for a frequency dependent attenuation different than a power law exponent of 2 (which corresponds to that of attenuation in water). This modification was implemented in the frequency domain after a Fast Fourier Transformation (FFT). Frequency dependent attenuation factors were then multiplied with individual frequency components. By means of an inverse FFT, a hybrid time and frequency domain algorithm was created.

pulse echo scattering

The received signal from an individual scatterer is calculated using an analytically derived spatial impulse response $h(r, z)$ for an unfocused circular transducer (Stephanishen, 1971):

$$\begin{aligned}
h(r,z:t) &= c_0 && \text{if } r < a \text{ and } t_0 < t < t_1 \\
h(r,z:t) &= \frac{c_0}{\pi} \cos^{-1}\left(\frac{r^2 - a^2 - z^2 + {c_0}^2 t^2}{2r\sqrt{{c_0}^2 t^2 - z^2}}\right) && \text{if } t_1 < t < t_2 \\
h(r,z:t) &= 0 && \text{elsewhere,}
\end{aligned} \tag{7.2}$$

in which,

$$\begin{aligned} t_0 &= z/c_0 \\ t_1 &= \frac{\sqrt{z^2 + (r-a)^2}}{c_0} \\ t_2 &= \frac{\sqrt{z^2 + (r+a)^2}}{c_0} \end{aligned} \tag{7.3}$$

where c_0 is the velocity of propagation within the medium, z is the axial coordinate of the field point, r is the radial coordinate of the field point, a is the radius of the piston transducer and t is time. Linear field calculations for a circular transducer with this analytically derived impulse response function showed a very high degree of similarity with acoustic fields calculated with the numerical ultrasound simulation program Field II (Jensen and Svendsen, 1992), which uses an approximation based on the summation of responses from small rectangles to calculate pressure fields from arbitrary shaped transducers using linear acoustics. The benefit of the analytically derived expression for the impulse response is that it is computationally efficient.

In order to be able to use this spatial impulse response in combination with propagation in a frequency dependent attenuating medium, the distance from an individual point-scatterer to the piston transducer is approximated by a single value, similar to the approach described by Jensen et al. (1993), which used the on-axis distance (z). Since signals in attenuating media exponentially decay with distance, the part of the transducer closest to the field point contributes most to the signal amplitude of this field point. Therefore, the shortest distance from a point-scatterer to the transducer, z_{att}, is used for attenuation calculations and is given by

$$\begin{aligned} z_{att} &= c_0 \cdot t_0 = z && \text{if } r < a \\ z_{att} &= c_0 \cdot t_1 && \text{if } r \geq a \end{aligned} \tag{7.4}$$

where t_0 and t_1 are defined in (7.3). Comparisons of this approximation with a numerical spatial impulse response method where frequency dependent attenuation was included showed a very high degree of similarity. For field points where $z \geq a/2$, amplitude differences of RF-signals were < 0.5 dB, calculated for attenuating media with a linear frequency dependency.

For the purposes of simulating ultrasound backscattered signals, tissue can be represented by many point scatterers positioned randomly in three dimensions (Kerr and Hunt, 1992; Hunt et al., 1995). Scatterers were placed at random locations, thus generally in

between grid locations where the transmitted field was calculated. All point scatterers were assigned the same scattering strength. Frequency dependent backscatter (μ_b) was taken into account by the approximation (Lockwood et al., 1991b)

$$\mu_b = \mu_0 \cdot \nu^\gamma \tag{7.5}$$

where μ_0 is the backscatter coefficient at 1 MHz, ν is the frequency expressed in MHz and γ represents the frequency dependence. The backscatter signal from the cloud of scatterers is calculated by a summation of the individual responses from each scatterer. The scatterer density (1250 scatterers/mm^3) was sufficient to produce Rayleigh envelope statistics.

The three-dimensional scatterer volume could be rotated with respect to the transmitted field to simulate catheter rotation of a mechanically scanned IVUS transducer.

For the simulations described in this paper, the following assumptions and simplifications have been made:
1. The sound-propagating medium is uniform and lossy, and dispersion is negligible.
2. The medium is assumed to be directly adjacent to the transducer surface.
3. Tissue is assumed to be a weak scattering medium (Born approximation).
4. Since weak scattering is assumed, the backscattered low-amplitude signal propagation is approximated by linear propagation.
5. The amplitudes of the backscattered signals are all relative, so no absolute pressures are given.
6. The catheter motion was assumed to be negligible during the transmit and receive of a single firing.
7. Motion other than catheter rotation was assumed to be not present, unless explicitly mentioned.

Simulation parameters

The nonlinear beams were calculated for a circular, unfocused transducer with a diameter of 0.9 mm, similar to elements used in previous IVUS THI studies (chapter 4). Since this element was centered at 30 MHz, the approach to attempt to use the lower and upper parts of the bandwidth for fundamental and harmonic imaging explained the choice of 20 MHz (fundamental) and 40 MHz (fundamental and 2^{nd} harmonic). Due to the circular symmetry, the three-dimensional field was calculated by a simulation in cylindrical coordinates. In all calculations, the excitation pulse was a Gaussian enveloped sine wave with a -6-dB fractional bandwidth of 30%.

The propagation medium characteristics were chosen to be in the range of those of vascular tissue and blood. Arterial tissue and blood have an attenuation frequency depen-

dency that can be described by equation (7.1), with power law exponents of $\gamma = 1.1$ and $\gamma = 1.2$ respectively in the frequency range 15–60 MHz (Lockwood et al., 1991b; Foster et al., 2000a). In the 10–50 MHz range, this is approximated by attenuation that has a linear frequency dependency in the range from 0.5 to 1.5 dB/cm/MHz. In this study, two different frequency dependent attenuation values of 0.6 and 1.0 dB/cm/MHz were used. The sound speed of the propagation medium was chosen to be 1560 m/s and the mass density was set at 1060 kg/m^3, both corresponding to published values of human tissue and human blood (Duck, 1990). The nonlinear parameter (B/A) (Hamilton and Blackstock, 1998) of tissue is estimated at 6–7 and that of human blood 6.0 (Duck, 1990), therefore the B/A-constant was chosen to be 6.0. These values appear not to have been measured at high frequencies (> 10 MHz).

The backscatter signal from scatterers is calculated by a summation of responses from all scatterers that are within the −20-dB beam width. In our case this means that all scatterers within a radial extent of 0.5 mm from the z-axis (corresponding to the propagation axis) are taken into account. In the depth direction, scatterers located between $z = 0.5$ and $z = 6.0$ mm are included in the calculations. There are no scatterers assumed to be close (< 0.5 mm) to the transducer, because of the water surrounding the transducer element within the protective sheath. Lockwood et al. (1991b) showed that the power law exponent of the frequency dependent backscatter in the artery wall ranged from $\gamma = 1.1$ to 1.4 at high frequencies, and that this parameter in blood ranged from $\gamma = 1.3$ to 1.4 at the same frequency range. A frequency dependence of $\gamma = 1.3$ has been chosen in this study.

Simulations

nonlinear beam simulations

Two-dimensional beam profiles were calculated for F20 and H40 mode through a medium with an attenuation of 1.0 dB/cm/MHz. For comparison, a beam profile of a fundamental 40 MHz pulse (F40) was also calculated. To study the influence of attenuation and excitation amplitudes on nonlinear generation, 20 MHz input pulses were propagated through two different attenuating media at peak envelope pressures ranging from 250 kPa to 4 MPa. F20 and H40 signal contents were isolated by digital filtering.

Penetration depth is an important issue in diagnostic ultrasound imaging, with attenuation effects limiting the signal strengths with increasing propagation distance. Since higher frequencies are attenuated more, the absolute penetration depth of a F40 field is less than that of a F20 field for identical excitation pressures. The penetration depth for the second harmonic (H40) field is more complicated since harmonic energy is both attenuated and generated during propagation. Since the harmonic generation is highly dependent on the fundamental amplitude, the absolute penetration depth will be highest

for high F20 excitation. The effective penetration depth of a F40 beam is therefore compared to an H40 beam by simulating a high amplitude (5 MPa) F40 beam and an H40 signal from a high amplitude (5 MPa) 20 MHz pulse through an attenuating medium of 1.0 dB/cm/MHz.

effects of rotation on averaging and decorrelation

As previously reported (chapter 4), averaging of neighboring RF-lines was used to increase signal-to-noise ratio (SNR). This assumes that the decorrelation effect on the H40 tissue signal from catheter rotation was small compared to uncorrelated noise. The competing effect of averaging and decorrelation by rotation on the SNR is investigated by pulse-echo simulations with a single point-scatterer located at 4 mm from the transducer face. The SNR is defined as the integrated RF-power of the signal only, divided by the integrated RF-power of the noise. White gaussian noise, characterized by a flat frequency spectrum and random phase, was generated by a random number generator. Both signal and noise were digitally band-pass filtered (32–50 MHz, 5^{th} order Butterworth). The catheter rotation was simulated by rotating the scatterer with respect to the beam over incremental angles of 0.15°, which corresponded to the experimentally employed line-density of 2400 RF-lines per rotation. Different background noise levels were added to calculate RF-lines and the results were digitally filtered. Next, the SNR difference was calculated as a function of number of averages. This SNR difference was then normalized for each different background noise level separately.

The point-spread function (PSF) was calculated for a single ideal point target at 4 mm from the transducer through an attenuating medium (1.0 dB/cm/MHz) for an F20, H40, and F40 field. The single-element transducer was rotated around its center (as indicated in fig. 7.1) with an angle of 0.15° between each line of sight.

effects of rotation on pulse inversion

The fundamental frequency signal will not be completely canceled with PI when motion between the tissue and catheter is present, which is explicitly shown for IVUS by Goertz et al. (2004). Nevertheless, this will be the situation when PI is performed with a single-element continuously-rotating IVUS catheter. To study the effect of catheter rotation on PI, two inverted 20 MHz pulses (0° and 180°) were propagated through the attenuating medium as the beam rotated past a 3D volume of point scatterers (fig. 7.1). The incremental inter-pulse angle was again 0.15°. Backscatter signals from the 3D volume of point scatterers have been calculated to simulate RF pulse-echo responses for different angles with respect to the IVUS transducer. A data set consisting of 32 different realizations of a volume of randomly positioned scatterers was calculated for a F20 2 MPa amplitude pulse-pair. The average cross-correlation value between RF-lines was calculated as a function of inter-pulse angle for raw and filtered RF-lines (32–50 MHz,

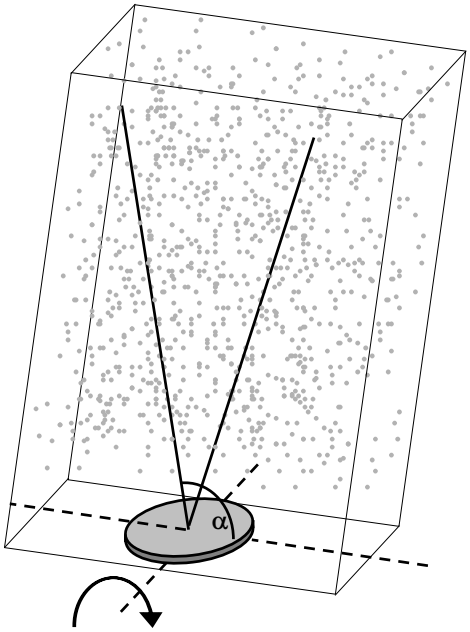

Figure 7.1: Schematic simulation setup, showing randomly distributed point-scatterers in a 3D volume relative to a rotating transducer.

5^{th} order Butterworth). For comparison, the average cross-correlation for F40 RF-lines has also been calculated. Fundamental suppression by PI was estimated at different distances from the transducer as a function of inter-pulse angle, assuming that the rotation speed is uniform. The mean fundamental signal content of pulse-pairs was calculated by summing the frequency power in the 18–22 MHz range.

Effects of axial motion on pulse inversion

Relative catheter and tissue motion due to effects other than element rotation is another potential cause for additional decorrelation between successive RF-lines. As investigated by Shen and Li (2002), axial motion, resulting in a phase/time shift, is much more severe than lateral motion for degrading the efficiency of PI. Therefore we simulated axial catheter-to-tissue motion (perpendicular to the transducer surface) to investigate the effect on fundamental suppression by PI at fixed inter-pulse angles. The calculated axial catheter-to-tissue motion is based on a PRF of 12.5 kHz, corresponding to a previously reported PRF (chapter 4). The mean fundamental signal content of pulse-pairs

was calculated by summing the frequency power in the 18–22 MHz range.

7.3 Results

nonlinear beam simulations

Example two-dimensional beam profiles for F20, H40 and F40 mode are plotted in fig. 7.2. These images are normalized with respect to the maximum signal within the individual images. The frequency dependent attenuating medium causes the F40 beam to decay faster than both the F20 and H40 beams. Close to the transducer, the H40 field exhibits a low intensity compared to the F20 and F40 field. Figure 7.3 shows on-axis fundamental and second harmonic pressures of the 20 MHz pulse at five different amplitudes, propagated through two different attenuating media. The frequency dependent attenuation in these simulations was 0.6 (left column) and 1.0 dB/cm/MHz (right column). The second harmonic pressure can be seen to build up progressively to reach a maximum pressure around 3 mm. From these figures the amplitude dependent second harmonic generation is evident. The ratio of the second harmonic at 40 MHz and the fundamental can also be seen in fig. 7.3 (bottom). Due to the increased attenuation, the H40/F20 ratio exhibits a faster decrease from approximately 3 mm than in the medium with the lower 0.6 dB/cm/MHz attenuation.

To compare penetration depth between F40 and H40, the absolute on-axis pressures of both beams are plotted in fig. 7.4. For both pulses the fundamental excitation amplitude was 5 MPa. From this graph it is clear that between 2 and 4 mm, which corresponds to the near field of the F40 beam, the absolute on-axis pressure of the second harmonic is higher than the F40. Above 4 mm the absolute pressures are similar. This simulation suggests that the H40 mode could result in a similar effective penetration depth

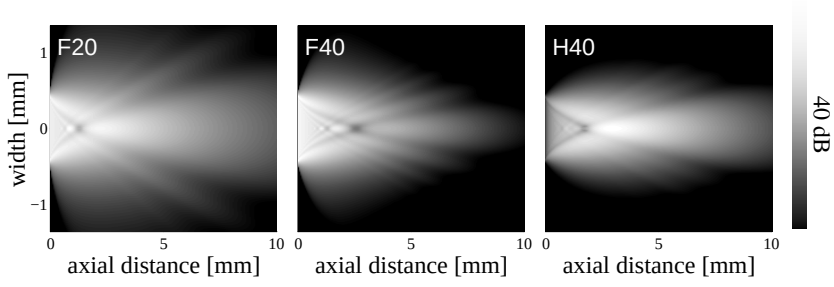

Figure 7.2: Two-dimensional beam profiles in F20, F40 and H40 mode. The beam profiles have been normalized with respect to the maximum signal within individual images.

compared to F40 mode.

effects of rotation on averaging and decorrelation

For a single scatterer located at 4 mm from the transducer, the normalized SNR difference is plotted logarithmically as a function of averaging in fig. 7.5 for different noise

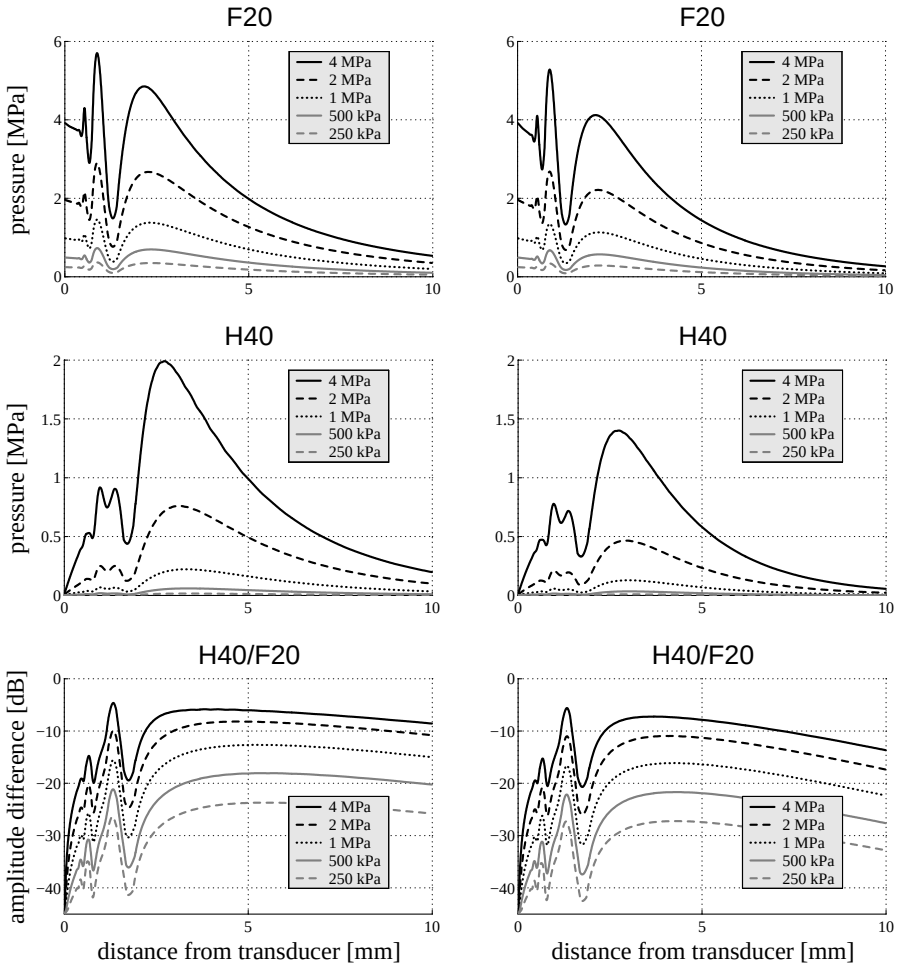

Figure 7.3: On-axis F20 and H40 pressures and the H40/F20 ratios for two different attenuating media (0.6 db/cm/MHz (left) and 1.0 db/cm/MHz (right)).

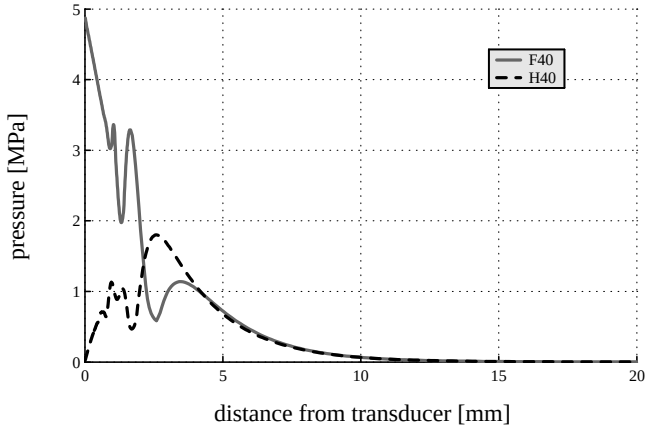

Figure 7.4: On-axis F40 and H40 pressures in an attenuating medium (1.0 dB/cm/MHz). Fundamental excitation pressures were 5 MPa for both.

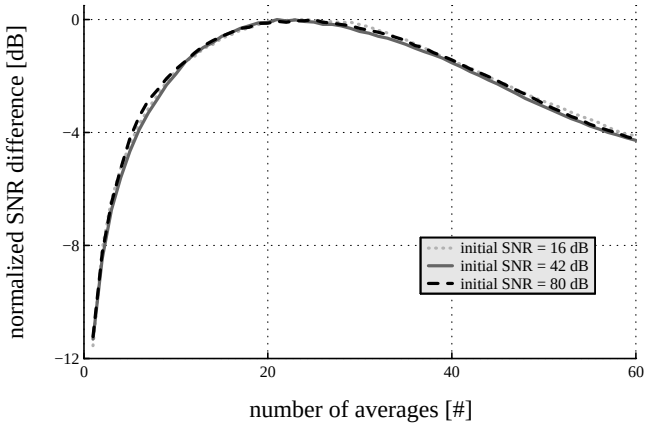

Figure 7.5: The normalized SNR effect of averaging neighboring noisy RF-pulse-echo responses from a single scatterer at 4 mm from the transducer.

levels (SNR is 16, 42 and 80 dB). These curves show the effect of averaging neighboring RF-lines around a center RF-line receiving the highest amplitude signal from the scatterer. The competing effects of averaging and decorrelation produce a local maximum

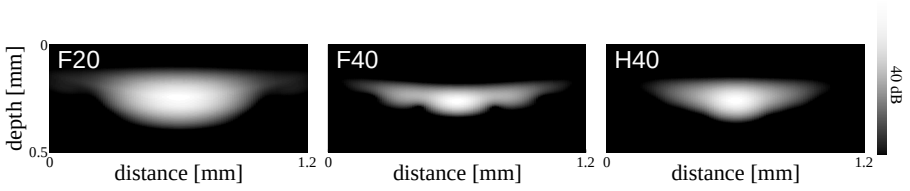

Figure 7.6: Point spread functions of F20, F40 and H40 of an ideal point scatterer at 4 mm distance from the transducer in an attenuating medium (1.0 dB/cm/MHz).

in SNR when 20–25 neighboring lines (corresponding to 3°–3.75°) were combined.

Point spread functions for a single scatterer at 4 mm from the transducer are depicted in fig. 7.6. These PSFs are normalized to the maximum signal level in each individual image. The different appearance can be partly attributed to the diffraction pattern of the different fields (see fig. 7.2). The −6-dB lateral beam widths of the F20, H40 and F40 PSFs are 0.39, 0.23 and 0.23 mm respectively. PSFs at different distances from the transducer will differ considerably, though fig. 7.6 gives a clarifying example of the PSF differences between F20, H40 and F40 modes. Note that the number of averages of neighboring lines will increase the effective beam width and therefore will degrade lateral resolution.

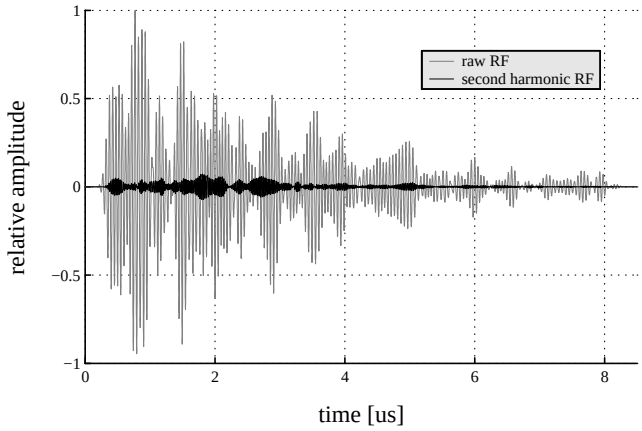

Figure 7.7: Typical raw and filtered (H40) RF-responses.

effects of rotation on pulse inversion

Nonlinear backscatter signals have been calculated to simulate the RF pulse-echo responses from different angles with respect to the IVUS transducer. A typical pulse-echo response can be seen in fig. 7.7. The digitally band-passed second harmonic signal of this RF-line is indicated in the same figure. The average inter-pulse cross-correlation estimates for the raw, H40 and F40 RF-lines are given in fig. 7.8 as a function of inter-pulse angle.

These curves show the mean of 100 cross-correlation curves for windowed RF-lines corresponding to backscatter from 2 to 3 mm from the transducer surface. It can be seen that the cross-correlation peak is narrower for H40 and narrowest for F40 where cross-correlation is > 0.5 within an angle of $1.0°$. The width of these cross-correlation peaks is attributed to the beam width at this distance (see fig. 7.2). These curves indicate the efficacy of averaging neighboring RF-lines to improve the signal-to-noise ratio (SNR) for small inter-pulse angles. For example, the decorrelation between H40 RF-lines (from 2–3 mm) is less than 0.1 within an angle of $0.5°$. Figure 7.9 shows the average frequency spectra of PI-pairs (2–4 mm) for different inter-pulse angles for 2 MPa amplitude pulse-pairs ($0°$ and $180°$). The fundamental suppression through PI at different distances is expressed as a function of inter-pulse angle in fig. 7.10. From this figure it is clear that the efficiency of PI decreases more rapidly with increasing inter-pulse angles. This figure

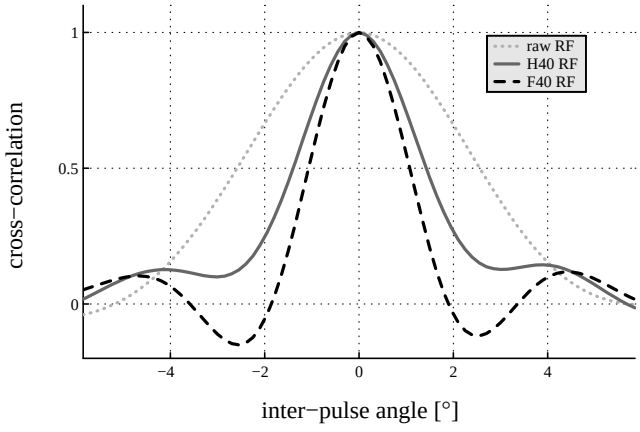

Figure 7.8: Cross-correlation between raw, H40 and F40 RF-lines at a distance of 2–3 mm from the transducer, plotted as a function of inter-pulse angle.

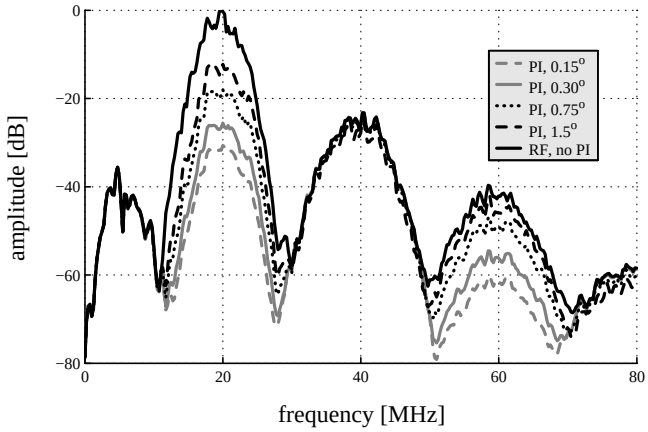

Figure 7.9: Average frequency spectra of single RF-line (solid black) and of PI-pairs with different inter-pulse angles.

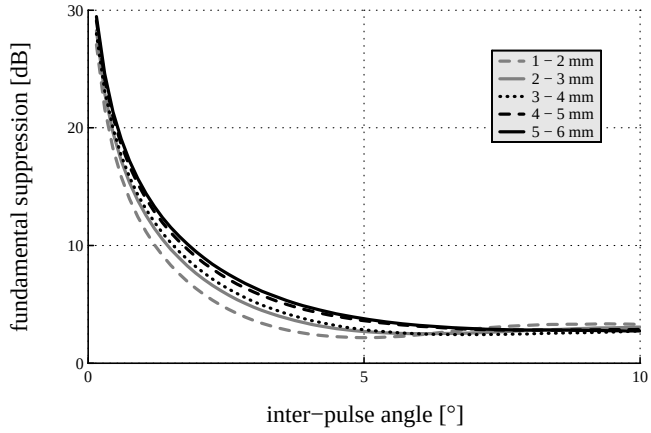

Figure 7.10: The fundamental suppression with PI as a function of inter-pulse angle as calculated for a 2 MPa pulse-pair calculated for different backscatter distances from the transducer.

also shows that the inter-pulse angle dependent fundamental reduction decreases quicker for scatterers that are located closer to the transducer. A fundamental suppression of approximately 16 and 10 dB is obtained when PI is applied with 512 (inter-pulse angle $\sim 0.70°$) and 256 (inter-pulse angle $\sim 1.4°$) RF-lines per rotation respectively. These line-densities correspond to those used in current clinical mechanically scanned IVUS systems.

effects of axial motion on pulse inversion

The effect of axial catheter-to-tissue motion on the average cross-correlation values between raw and H40 filtered RF-signals from a depth of 2 to 3 mm has been plotted in fig. 7.11. For a transmit amplitude of 2 MPa PI-pairs at a depth of 2 to 3 mm and for inter-pulse angles of $0.15°$, $0.30°$, $0.75°$ and $1.5°$, the average fundamental suppression is plotted as a function of catheter-to-tissue motion expressed in fundamental wavelengths between successive pulses (λ) in fig. 7.12. This graph illustrates that axial motion begins to degrade fundamental suppression for an inter-pulse angle of $0.15°$ from $\lambda > 0.005$, corresponding to > 5 mm/s, based on a fundamental frequency of 20 MHz and a PRF of 12.5 kHz.

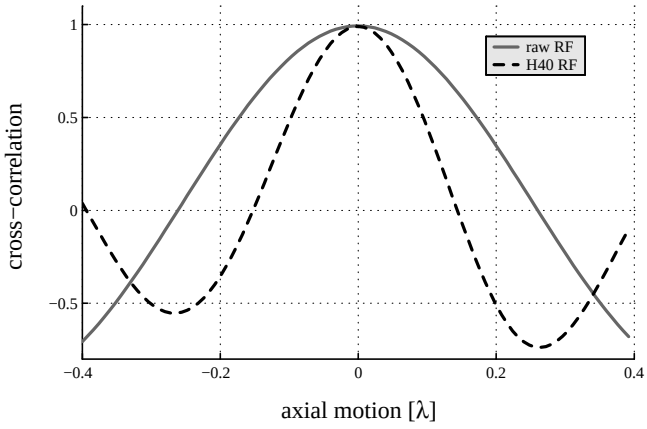

Figure 7.11: Cross-correlation of raw and H40 RF-lines at a distance from 2 to 3 mm from the transducer, plotted as a function of axial catheter-to-tissue motion expressed in fundamental wavelengths.

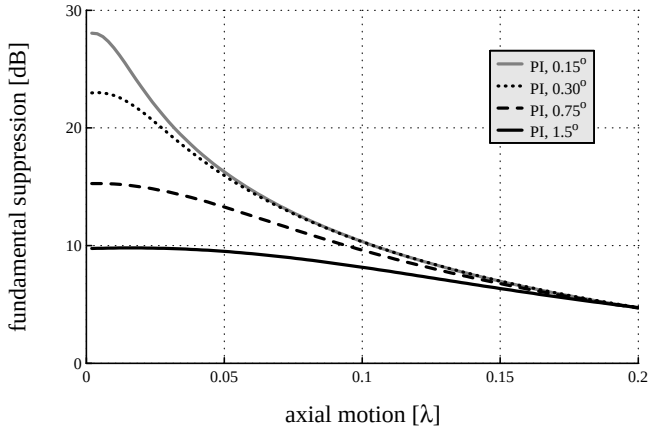

Figure 7.12: Fundamental suppression with PI as a function of axial catheter-to-tissue motion at a distance from 2 to 3 mm from the transducer for different inter-pulse angles.

7.4 Conclusion and discussion

Nonlinear fields at 20–40 MHz have been simulated for circular IVUS transducers through media with frequency dependent attenuation values in the range of those of vascular tissue and blood. The influence of catheter rotation on the fundamental suppression of pulse inversion has been studied for a range of inter-pulse angles. The effect of axial catheter-to-tissue motion on the fundamental suppression of pulse inversion has also been investigated.

The nonlinear beam simulations were carried out in a lossy and nonlinear medium, where dispersion was assumed to be negligible. Dispersion, the frequency dependent phase speed, would lead to smoothing of the wave profile and thereby suppressing nonlinear distortions (Naugolnykh and Ostrovsky, 1998). Limited experimental evidence shows that biologic tissue is dispersive but that it is only 0.7% per frequency decade for an attenuation of 1 dB/cm/MHz (Gurumurthy and Arthur, 1982). For many practical purposes this variation in the phase velocity can be assumed constant (Angelsen, 2000). The frequencies of interest in this study cover only a limited frequency range and the relatively high frequency dependent attenuation of blood and tissue prevents shock waves from being generated. Hence, dispersion was considered negligible. Thorough studies on the effect of dispersion under nonlinear propagation in media with frequency power law dependent attenuation have been performed (Szabo, 1995; He, 1998; Wallace et al.,

2001).

In the nonlinear beam simulations where absolute penetration depths of F40 and H40 fields were compared, the assumption was made that the maximum pressure at the transducer surface was the same for the 20 MHz as well as for the 40 MHz excitation pulse. The maximum excitation pressure for a single-element IVUS catheter was approximated by 5 MPa. Moran et al. reported a peak negative pressure of 3.27 MPa at a distance of 2 mm from a commercial 30 MHz single-element catheter, corresponding to a Mechanical Index (MI) of 0.59 (Moran et al., 2002). The 20 and 40 MHz pulses with a peak negative pressure of 5 MPa, which were used in this study, would lead to maximum MI-values of 1.1 and 0.79 respectively, which is below the MI limit (of 1.9) of current clinical ultrasound equipment. Another potential restriction on the maximum peak pressure is acoustic saturation, which is a physical limit. Acoustic saturation, defined as the condition where incremental transmission loss closely approximates the incremental increase in source intensity, limits the maximum acoustic pressure that may be reached in a soft tissue. According to Duck (1999) saturation pressure in tissue may tend toward the saturation limits given by weak-shock theory. These theoretical saturation limits were far from exceeded by the 5 MPa amplitude pulses at 20 and 40 MHz as used in this simulation.

The effect of rotation on averaging, decorrelation and pulse inversion was simulated by rotating the transducer with respect to the scatterer volume. The minimal rotation angle between successive lines of sight was chosen to be 0.15°, corresponding to the experimentally used line-density of 2400 lines per rotation (chapter 4). Using this line-density, the commercially and clinically used rotational speed of thirty rotations per second will then result in a pulse-repetition-frequency (PRF) of approximately 75 kHz, which is still lower than the maximum PRF ($\sim$100 kHz) of a rotating single-element IVUS system as limited by sound propagation speed assuming a penetration depth of 7.5 mm. So in spite of the lower line-density (e.g. 256 lines per rotation) at 30 rotations per second of current commercially available IVUS systems, no physical limitations exist to increase to a line-density of 2400 lines per rotation.

Experimental data on the effect of catheter rotation on PI with a prototype harmonic IVUS system is reported in chapter 8. Those results correspond reasonably well to the simulation results as presented in this study, indicating the validity of the simulation approach.

The effect of axial tissue-to-catheter motion on the average fundamental suppression by PI was expressed as a function of relative axial motion between successive inverted pulses. Shen and Li (2002) found that axial motion between two successive pulses of less than 0.125 λ (where λ is the wavelength at the fundamental frequency) partly can-

cels the second harmonic intensity and increases fundamental leakage. An estimation of absolute axial motion as present in arteries is needed for useful interpretation of fig. 7.12. The maximum axial tissue (vessel wall) motion with respect to the center-line of a vessel can be obtained from published data (Tortoli et al., 2001; Hoeks et al., 1990), which show common carotid artery wall peak velocities in the range of 2–8 mm/s. Derived from coronary artery pressure-area curves (Williams et al., 1999), maximum vessel wall velocities in the radial direction are 2 mm/s. If no catheter translation is assumed, an upper estimate of axial vessel wall motion between successive pulses at the experimentally used PRF of 12.5 kHz (chapter 4) would be 0.008 λ. For the more realistic situation where catheter translation is assumed, the maximum axial tissue motion of the coronary vessel wall with respect to an IVUS catheter was estimated at approximately 3.5 mm/s, derived from recent IVUS palpography data (Leung et al., 2006). Since this would correspond to a movement of 0.004 λ (when the PRF is 12.5 kHz), axial catheter-to-tissue motion between consecutive pulses could be considered to be of low influence on fundamental suppression ($<$ 1dB) and on the second harmonic intensity. Nevertheless, the significance of axial catheter-to-tissue motion will increase with increasing fundamental frequencies and for decreased PRFs.

The results from this simulation study are important to guide future optimization of system design for harmonic IVUS applications (THI and contrast harmonic imaging) with mechanically scanned single-element catheters. The PRF, line-density and transducer size and geometry could be altered to optimize the fundamental suppression with PI. This simulation tool could also be used to investigate different pulse schemes (coded excitation) for isolating harmonic signals. Further, such simulations may also be useful in the context of guiding the implementation and optimization of nonlinear contrast imaging systems (Goertz et al., 2006a). For example, for second harmonic intravascular contrast imaging, where the tissue harmonic component is an artifact that must be minimized.

Chapter 8

Nonlinear intravascular ultrasound contrast imaging

Based on the publication *"Nonlinear intravascular ultrasound contrast imaging"* by Goertz D.E., Frijlink M.E., De Jong N. and Van der Steen A.F.W., Ultrasound Med Biol, 32(4):491–502, 2006. *with permission from the World Federation of Ultrasound in Medicine and Biology*

Abstract – Nonlinear contrast agent imaging with IVUS is investigated using a prototype IVUS system and an experimental small bubble contrast agent. The IVUS system employed a mechanically scanned single element transducer and was operated at a 20 MHz transmit frequency (F20) for second harmonic imaging (H40), and at a 40 MHz transmit frequency (F40) for subharmonic imaging (SH20). Characterization experiments were performed with agent and tissue phantom signals acquired during transducer rotation. The suppression of transmit frequency tissue signals was achieved using a combination of pulse-inversion and bandpass filtering. H40 was found to improve the contrast-to-tissue signal ratio (CTR) relative to F20, but suffered from tissue propagation harmonics at higher pressures (>0.3 MPa). SH20 was also shown to be possible, with tissue signals suppressed to near the noise floor. Coronary phantom experiments demonstrated the detection of agent in 1 mm diameter vessels outside a larger 4 mm diameter vessel in which the IVUS catheter was situated. These results suggest the feasibility of harmonic IVUS contrast imaging, which may have applications in coronary lumen boundary detection and *vasa vasorum* imaging.

8.1 Introduction

A potential application of contrast in IVUS is *vasa vasorum* imaging. The *vasa vasorum* are microvessels surrounding and penetrating the walls of larger blood vessels. The pathologic development of neovascular *vasa vasorum* has been linked with atherosclerotic plaque progression (Moulton, 2002). *Vasa vasorum* have also been associated with intraplaque hemorrhage and plaque inflammation (Kumamoto et al., 1995; Moulton et al., 2003). Increasingly, it is thought that *vasa vasorum* may play an important role in plaque rupture in stroke (Mofidi et al., 2001) and myocardial infarctions (Barger and Beeuwkes, 1990; Tenaglia et al., 1998). There is, therefore, a growing demand for vasa vasorum imaging techniques for diagnostic purposes and for monitoring therapeutic interventions. Recent work has shown the potential of magnetic resonance imaging (Kerwin et al., 2003) and transcutaneous ultrasound (Feinstein, 2004) to detect *vasa vasorum* within atherosclerotic plaques of carotid arteries. However, there are no established *in vivo* or clinical tools for imaging *vasa vasorum* in the coronary arteries. Though high frequency (20–50 MHz) ultrasound biomicroscopy (UBM) flow imaging systems have been shown to detect and image microvascular flow (Kruse and Ferrara, 2002; Goertz et al., 2003b) in the absence of contrast agents, issues of severe tissue motion may render such approaches ineffective with IVUS systems operating in coronary arteries. IVUS flow imaging systems developed to examine flow within the lumen of large arteries (Li et al., 1998; Lupotti et al., 2003) appear not to be capable of detecting vasa vasorum. We hypothesize that the use of nonlinear contrast imaging may be one strategy for enabling the effective detection of *vasa vasorum* with IVUS.

To date, IVUS contrast work has examined or assumed linear agent behavior. However, recent studies have shown the feasibility of nonlinear microbubble imaging at transmit frequencies of up to 30 MHz (Goertz et al., 2005a). Subharmonic imaging was demonstrated for transmit frequencies of 20 and 30 MHz and ultraharmonic imaging for a 20 MHz transmit frequency. Second harmonic imaging for a 20 MHz transmit frequency was not found to improve the contrast-to-tissue ratio (CTR) due to the presence of strong tissue propagation harmonics under the conditions investigated. This work was conducted with modifications to existing UBM instrumentation (Foster et al., 2002), which is appropriate for use in ophthalmology, dermatology and small animal imaging. The spherically focused PVDF transducers used in this instrumentation are broad bandwidth (Sherar and Foster, 1989; Foster et al., 2000a) and capable of generating high pressures in the focal zone. Nonlinear signals were extracted directly through analog filtering rather than using multi-pulse techniques such as pulse-inversion (Hope Simpson et al., 1999). Furthermore, the agent employed was Definity™ (Bristol Myers Squibb Medical Imaging, New York, NY, USA), which was not specifically designed for use at high frequencies.

It has been hypothesized that nonlinear scattering observed for higher transmit frequencies is associated with a subpopulation of smaller bubbles present in current clinically available agents. This is supported by the results of mechanical filtration experiments (Goertz et al., 2003a). Though generally not reported on in a quantitative manner, micrometer to submicrometer diameter bubbles only comprise a small portion of the volume fraction of these agents (e.g. Gorce et al., 2000), which suggests that the majority of the volume fraction may not be participating in nonlinear scattering at high transmit frequencies. In a study by Goertz et al. (2006b) an experimental lipid encapsulated agent (BG2423, Bracco Research, Geneva, Switzerland) comprised substantially of micrometer and submicrometer sized bubbles was evaluated for nonlinear scattering for transmit frequencies of 20 and 30 MHz. A spherically focused PVDF transducer was employed, with pulse bandwidths varied between 5 to 25% and pressures from ~0.25 to 5.0 MPa. This configuration permitted broad bandwidth observations of nonlinear scattering with pressure conditions controlled at focus, which was not possible with IVUS transducers. It was found that subharmonics could be generated at a wide range of pressures. Second harmonic energy was also observed, though in the presence of substantial nonlinear propagation harmonics. Evidence of bubble disruption was found only at high pressures (e.g. >2 MPa for 30 MHz and 25% bandwidth).

The objective of this study was to investigate the feasibility of performing harmonic contrast agent imaging with IVUS. The contrast agent employed was BG2423, the same as that previously employed by Goertz et al. (2006b). The prototype single-element mechanically-scanned nonlinear IVUS imaging system was used. The generation and reception of nonlinear signals in contrast agent suspensions and phantom material were examined for 20 and 40 MHz transmit frequencies. Specifically, we evaluated the second harmonic of a 20 MHz transmit (H40) and the subharmonic of a 40 MHz transmit (SH20). Phantom imaging experiments were then performed to investigate image formation using H40 and SH20.

8.2 System description

System overview

The prototype nonlinear IVUS imaging system was previously described (section 2.3). The amplified transmit signals were sent through the modified commercial rotational motor unit (section 2.2) to a single-element IVUS catheter (Princeps 4.3 French, DuMed, Rotterdam, Netherlands). The transducer element was unfocused and elliptical (long axis 1 mm, short axis 0.75 mm) with a nominal center frequency of 30 MHz.

On receive, the RF signals were amplified and bandpass filtered (12–60 MHz, 5^{th} order Butterworth). The signals were digitized at 200 megasamples/sec with the 12-bit

acquisition board (section 2.2).

Transmit characteristics: Methods

The second harmonic signal of a 20 MHz transmit (F20; 25% −6-dB Gaussian enveloped input pulse), and the subharmonic signal of a 40 MHz transmit (F40; 25% −6-dB Gaussian enveloped input pulse) were examined here. Experiments were conducted at a range of transmit pressures, which were characterized with hydrophone water tank experiments. The relative hydrophone-transducer position was controlled by mounting the transducer to the XYZ-micropositioning stage (see section 2.2). Two-dimensional beam measurements of a plane perpendicular to the transducer face, parallel to the short axis of the transducer ellipse, were performed to estimate lateral beam widths and to align the transducer and hydrophone axes for the on-axis beam plots. A grid spacing of 50 μm laterally (parallel to the transducer face) and 200 μm axially (perpendicular to the transducer face) was employed. The peak of the envelope was estimated at each location using a transmit amplitude for the 20 and 40 MHz scans respectively.

One-dimensional on-axis beam profiles were then made using a step size of 100 μm. Peak negative pressures are reported for the 20 and 40 MHz cases. The H40 pressure is also reported by taking the pressure of the envelope of the received signal after it had been digitally bandpass filtered (32–50 MHz) to isolate the harmonic signal. The −6-dB pulse lengths and bandwidths for the 20 and 40 MHz transmit pulses were estimated using the hydrophone signals at 1 and 2 mm from the transducer respectively.

Transmit characteristics: Results

Axial beam pressure plots for the 20 MHz case are shown in fig. 8.1 for a range of transmit conditions. The curves exhibit peaks at approximately 0.9–1 mm and then undergo monotonic decays. By 6 mm, the amplitudes are less than half the peak amplitude (for example 44% in the 0.9 MPa peak pressure case). In phantoms and *in vivo* this decay can be expected to be more pronounced according to attenuation levels. The beam diffraction will therefore result in a considerable variation in the pressure level experienced by bubbles at different locations within the beam.

The second harmonic signal level is shown in fig. 8.1 for five of the 20 MHz transmit pressures. The H40 signal builds until approximately the 3.5–5 mm range, and then decreases, a pattern similar to that reported in chapter 4. The peak H40 signal level can also be seen to increase steeply as a function of transmit pressure. These signals are exploited in chapter 4 for the purposes of tissue harmonic imaging by using high transmit amplitudes. In the present study nonlinear propagation will act to degrade the perfor-

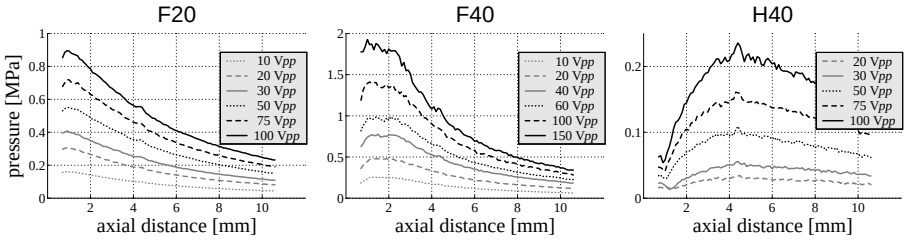

Figure 8.1: F20, F40 and H40 on-axis peak negative pressure values for a range of F20 and F40 transmit amplitudes.

mance of H40 contrast imaging. The H40 levels in phantom and *in vivo* conditions will differ from these measurements according to attenuation and nonlinearity properties of the propagation medium.

The 40 MHz curves exhibit peak pressures in the 0.8–2.3 mm range and then decay in amplitude. The flatness of the peaks may be the result of spatial averaging due to the size of the hydrophone. By 6 mm, the amplitudes are less than half the peak amplitude (for example 43% in the 1.4 MPa peak pressure case). Again, this decay in transmit amplitude will have implications for the generation of nonlinear signals from bubbles at different locations within the beam.

The pulse lengths and bandwidths for the 20 and 40 MHz cases at 1 and 2 mm from the transducer face respectively are summarized in table 8.1. In the remainder of this chapter, the transmit pressure levels quoted will refer to the peak on-axis hydrophone values.

Table 8.1: Summary of hydrophone measured transmit pulse lengths and bandwidths for the IVUS experiments. 20 MHz data collected at 1 mm from transducer face; 40 MHz data at 2 mm from transducer face.

Transmit center frequency	**20 MHz**	**40 MHz**
−6-dB pulse lengths (μm)	146	143
−6-dB BW points	18.2–27.8 MHz	32.8–43.2 MHz
−12-dB BW points	15.2–28.9 MHz	31.2–44.7 MHz

The transmit frequency response of the transducer had a peak at 26.0 MHz and −10-dB points at 15.6 and 47.3 MHz. At 20 and 40 MHz, the response was 5.4 and 2.5 dB lower than the peak response. The 2D one-way beam measurements indicated −3-dB beam widths of 305 μm at 1 mm for the 20 MHz case, and 230 μm at 2 mm for the 40 MHz case.

8.3 Phantom and agent characterization experiments

Methods

Phantom experiments were performed to investigate the production and detection of nonlinear signals with an IVUS system, and to form images based on nonlinear signals acquired during mechanical scanning. The IVUS transducer was situated in a semicircular 1.4 mm diameter notch in the boundary between a suspension of agent and a block of tissue mimicking material. The acquisition of tissue signals in addition to agent signals was necessary in order to examine issues of fundamental frequency signal suppression and nonlinear propagation. Such a phantom configuration is directly relevant to the situation where the ultrasound beam propagates through agent before reaching a region of interest. This will be the case for enhanced lumen boundary imaging (e.g. Cachard et al., 1997), where both the catheter and agent will be situated within the lumen of a large vessel. This configuration is also relevant to *vasa vasorum* imaging, where agent is present in the main lumen and microvessels are situated in close proximity to the lumen boundary, such as at the plaque shoulders. Another relevant scenario for *vasa vasorum* imaging will involve the beam passing through intervening regions of agent (in the lumen) and tissue before encountering agent in small vessels. This case is explored in a preliminary manner in the following section.

The phantom material was produced according to the procedures detailed by de Korte et al. (1997). The acoustic velocity and attenuation properties of this material at IVUS frequencies have been examined by de Korte et al. (1997). Using this configuration, a single rotation of the catheter was sufficient to permit an analysis of received signals from both agent and tissue regions. Additionally, a 24-gauge needle was inserted into the phantom proximal to the phantom/agent interface with an orientation parallel to the catheter axis. This was done in order to provide a large amplitude reflector within the images. The contrast agent was diluted with saline (0.9% NaCl by weight) by a factor of 1000 times relative to that in the vial.

Imaging was conducted in the following manner. A pulse-inversion sequence (Hope Simpson et al., 1999) was employed using equally spaced, alternately inverted pulses. Since relative motion between the tissue and transducer between pulses can result in decorre-

lation that will degrade the performance of pulse-inversion suppression of fundamental frequency signals (Shen and Li, 2002), it was desirable to minimize the spatial separation (i.e. inter-pulse rotation angle) between pulses. A higher pulse density will also enable increased pulse averaging in order to improve SNR. A typical clinical frame rate for IVUS is 30 Hz, which corresponds to 33.3 ms per rotation. If it is assumed that attenuation and beam diffraction effects limit penetration depth to 10 mm, and the acoustic velocity is assumed to be 1500 m/s, then this imposes a 75 kHz limit in PRF if the received energy from successive pulses is to remain separated. In this regard, the depth limitations imposed by the use of high frequencies are advantageous from the perspective of permitting a high PRF to be employed. With these assumptions, there is a 2500 pulses-per-rotation limit. In practice, power amplifier PRF limitations required a PRF of 12.5 kHz to be employed in this study. In order to evaluate the 2500 pulses per rotation condition, the frame rate was therefore reduced to 5 Hz.

For a 20 MHz transmit pulse, an H40 image line was calculated by first summing 8 adjacent pulses (i.e. 4 adjacent inverted pulse-pairs), applying a digital bandpass filter (30–45 MHz, 5^{th} order Butterworth), and then calculating the envelope of the resulting signal. F20 image lines were calculated from the same data sets by averaging 4 alternate pulses (from the same 8 pulse ensemble used for the H40 image line), applying a digital bandpass filter (15–30 MHz, 5^{th} order Butterworth), and then taking the envelope of the resulting signal. A similar procedure was used for the 40 MHz transmit pulse, with the digital filters instead being between 15–30 MHz for SH20 imaging, and 30–45 MHz for F40 imaging.

The choice of the pulse ensemble length parameter can be expected to affect SNR through the competing effects of noise averaging and signal decorrelation, and will also impact the lateral resolution. An exploration of the effects of this parameter is not conducted in this study.
To gain insight into the received IVUS signals, the average tissue and agent spectra are examined as a function of depth prior to image formation. Example results are shown for a depth window of 1 mm in length (1.3 μs), centered at 2.5 mm in depth. After the application of a Hanning window to each RF segment, the raw spectra were estimated with 700 traces from either the tissue or agent regions. Specifically, the average spectra of the 700 individual traces, and the average spectra of the 350 time-averaged pulse-pairs were calculated.

Results: received signals

Example spectra from tissue and contrast regions (between 2–3 mm offset from transducer face) for the 20 MHz transmit case (0.3 MPa) are shown in fig. 8.2. In tissue, there

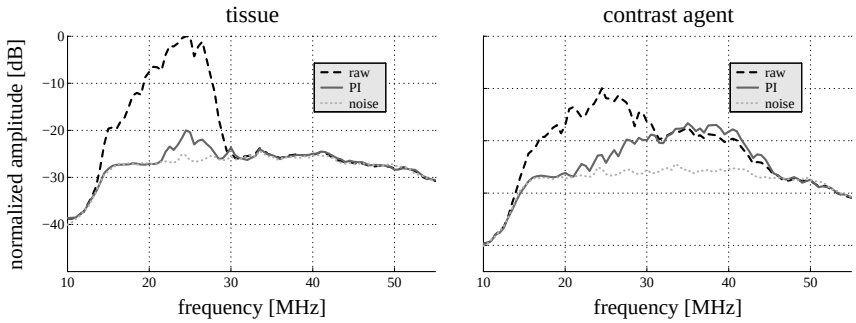

Figure 8.2: Frequency spectra of raw RF-signals, pulse-inversion pairs and noise from the tissue (left) and contrast agent (right) regions for a 20 MHz transmit pulse (0.3 MPa, 2–3 mm depth).

was a pronounced peak just above 20 MHz. With the application of pulse-inversion, this was reduced by approximately 20 dB. In the contrast agent region there was also a peak towards 20 MHz, though the energy was distributed more broadly. With the application of PI, energy in the second harmonic region was preferentially retained. While pulse-inversion resulted in substantial reduction in fundamental frequency energy, some still remained, which is interpreted to be due to decorrelation effects arising from transducer motion between adjacent pulses. A digital bandpass filter was therefore used to remove the residual fundamental frequency energy.

Average spectra from tissue and contrast regions (between 2–3 mm offset from transducer face) for the 40 MHz transmit case (0.9 MPa) are shown in fig. 8.3. In tissue, there was a pronounced peak just below 40 MHz. With the application of PI, this was reduced by approximately 25 dB. In the contrast region, there was also a peak towards 40 MHz, but a lower peak towards the subharmonic region is also evident. Upon application of PI, the subharmonic peak became the dominant portion of the remaining energy.

Results: imaging

Example results of F20 and H40 image formation are shown in fig. 8.4. In F20 mode (0.3 MPa), the agent signals were clearly weaker than the tissue signals. With the application of bandpass filtering to extract the H40 signal, the CTR improved substantially, though residual tissue signals were clearly present. Using pulse-inversion in combination with filtering, the tissue signals were suppressed to below the noise floor. As pressure was increased however, tissue propagation harmonic degraded CTR. Note also the prominence of the highly reflective needle in the 8 o'clock position.

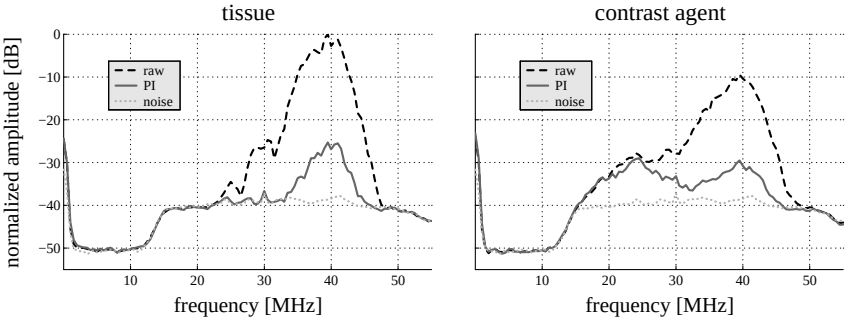

Figure 8.3: Frequency spectra of raw RF-signals, pulse-inversion pairs and noise from the tissue (left) and contrast agent (right) regions for a 40 MHz transmit pulse (0.9 MPa, 2–3 mm depth).

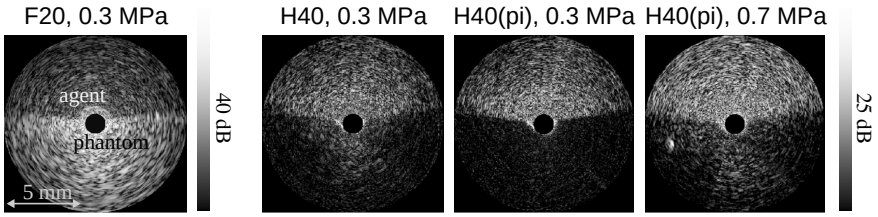

Figure 8.4: Images of tissue phantom and contrast agent for a 20 MHz transmit frequency. H40 images, with and without pulse-inversion (pi) and for different fundamental transmit pressures, show different levels of suppression of tissue signals.

The results for F40 and SH20 image formation are shown in fig. 8.5. In F40 mode (0.9 MPa), the agent signal was again substantially weaker than the tissue signals. With digital bandpass filtering about the SH20 (13–30 MHz), the agent signal becomes prominent, but a residual tissue signal was still present due to F40 energy leakage. When pulse-inversion was applied in addition to filtering, the subharmonic agent signal remained, while the F40 tissue signal was suppressed to below the noise floor. As the pressure was lowered from 0.95 MPa to 0.65 MPa, the contrast-to-noise ratio (CNR) degraded.

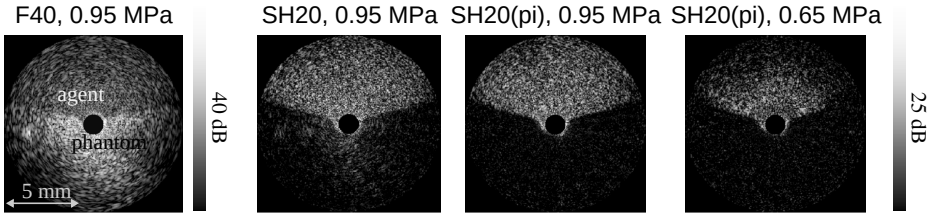

Figure 8.5: Images of tissue phantom and contrast agent for a 40 MHz transmit frequency. SH20 images, with and without pulse-inversion (pi) and for different fundamental transmit pressures, show different levels of suppression of tissue signals.

8.4 Coronary phantom imaging experiments

Methods

Additional phantom experiments were conducted to explore the detection of small vessels present outside the main lumen of a coronary artery, a situation relevant to *vasa vasorum* detection. The phantom was comprised of tissue mimicking material in which a main vessel of 4 mm in diameter (representing the coronary artery) and up to four 1 mm diameter parallel vessels situated at different locations outside the main lumen are present. This configuration permits the investigation of a range of relative catheter-vessel locations under different flow conditions. In this section, examples of image formation are shown for the case of agent being present in the main lumen and in two small vessels with center axes located at distances of 2 mm (“v1”) and 4 mm (“v2”) from the main lumen boundary.

Stainless steel rods were used to cast the vessel lumens, which were formed upon removal of the rods after the phantom had solidified. Flow through the small vessels and central coronary channel can be controlled independently through connections to flow tubes, but in these particular experiments is kept stationary.

CTR (F20 and H40; F40 and SH20) estimates are made for the smaller vessels by taking the average power in a 0.5 mm square region within the vessel and in the tissue region immediately adjacent to it.

Results

Example F20 and H40 images at lower (0.32 MPa) and higher (0.58 MPa) pressures are shown in fig. 8.6. At both pressures, the main lumen can be observed in the F20 images

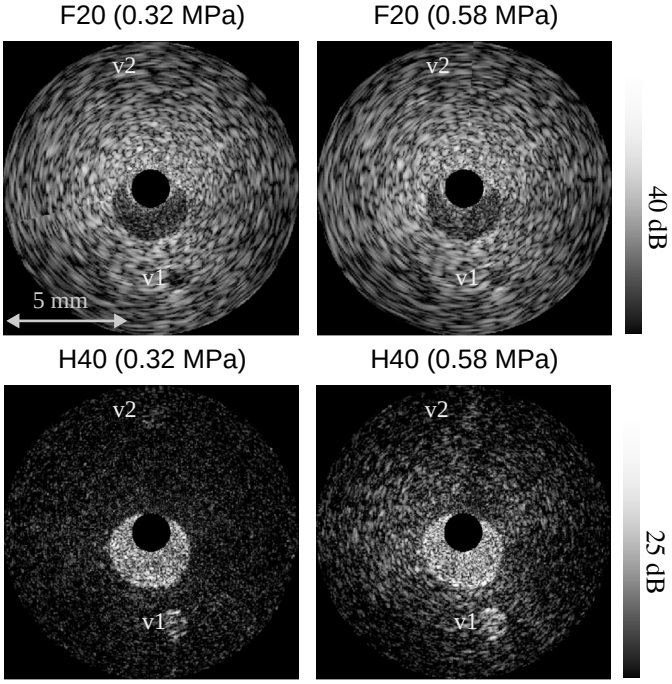

Figure 8.6: Coronary phantom images for a 20 MHz transmit frequency. F20 images at two pressure levels show agent within the main lumen and the "v1" vessel outside the main lumen. In H40 mode at 0.32 MPa, the CTR improves substantially for the main lumen, the "v1" vessel, while the "v2" vessel is at the edge of detection. As at a 0.58 MPa transmit level, the H40 tissue signal becomes prominent, though the CTR is still better relative to F20.

as a region of lower echogenicity than the surrounding tissue. The "v1" vessel can also be delineated with difficulty (CTR = −1.8 dB) whereas the "v2" vessel cannot be distinguished from the surrounding tissue. In H40 mode, the use of lower pressures results in improved visualization of the lumen and "v1" vessel (CTR = 8.9 dB) while the "v2" vessel is barely visible (CTR = 4 dB). At the higher pressure the H40 CTR degrades.

Example F40 and SH20 images at lower (0.9 MPa) and higher (1.4 MPa) pressures are shown in fig. 8.7. As for the F20 case, the main lumen can be observed in the F40 images as a region of lower echogenicity than the surrounding tissue. The "v1" vessel can also be delineated with difficulty (CTR = −6.7 dB) and the "v2" vessel is arguably at the edge of detection for the surrounding tissue (CTR = −3.3 dB). In SH20 mode, the low pressure image exhibits improved visualization of the lumen and "v1" vessel (CTR =

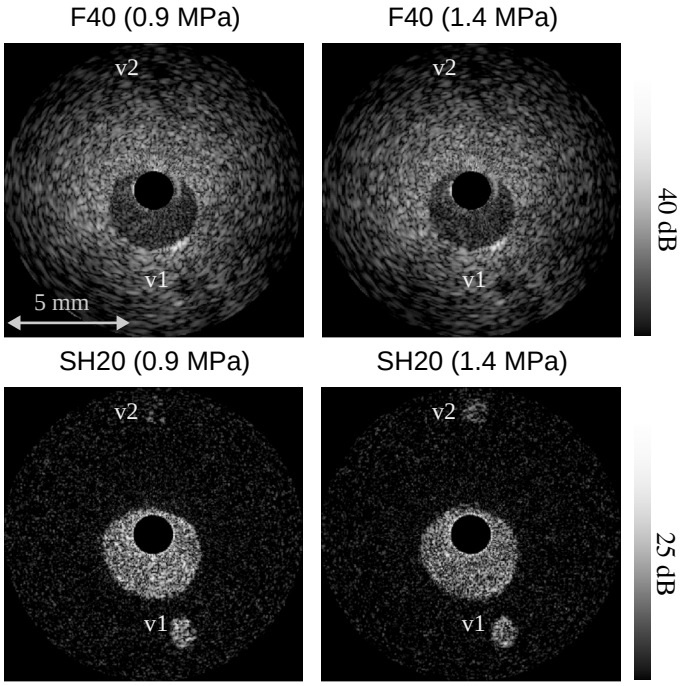

Figure 8.7: Coronary phantom images for a 40 MHz transmit frequency. F40 images at two pressure levels show agent within the main lumen and the "v1" vessel outside the main lumen. In SH20 mode at 0.9 MPa, the CTR improves substantially for the main lumen, the "v1" vessel, while the "v2" vessel is at the edge of detection. At a 1.4 MPa transmit level, the tissue signal does not increase, as in the H40 case, and the CTR for the "v2" vessel undergoes further improvements.

13.2 dB) while the "v2" vessel is barely visible (CTR = 3.8 dB). At higher pressure, the main lumen and "v1" (CTR = 10.8 dB) are visible, and "v2" has become more prominent (CTR = 7 dB).

These data indicate that visualization of agent in vessels outside the main lumen is feasible in both H40 and SH20 modes. The signal strength from agent will clearly depend upon the transmit pressure and the attenuation properties of the intervening tissue.

8.5 Discussion

Previous high frequency nonlinear contrast imaging studies (Goertz et al., 2005a, 2006b) employed analog receive filtering to isolate nonlinear signals, which imposes bandwidth and therefore resolution limitations. In the present study it has been shown that pulse-inversion extraction of both subharmonic and second harmonic signals arising from a contrast agent is possible in this frequency range. It is also notable that substantial suppression of tissue signals was achieved during mechanical scanning. Array-based implementations of PI techniques employed in conventional ultrasound machines apply PI using pulse-pairs that are sent along the same line of sight. It is known that relative transducer-tissue motion leads to a decorrelation of tissue signals that can result in ineffective cancelation of linear signals (Shen and Li, 2002). Using a spatial pulse separation that is compatible for use at clinical IVUS frame rates (30 Hz), it has been found that pulse-inversion techniques can result in effective suppression of linear signals (see also chapter 7).

The results of this study show that it is possible to achieve improvements in CTR with second harmonic imaging at high frequencies. No improvement of CTR was found by using H40 mode relative to F20 by Goertz et al. (2005a). This different conclusion may be due to a number of factors that favor the production of a detectable second harmonic bubble signals at pressure levels that do not result in the significant accumulation of propagation harmonic. One factor may be the use of a more effective contrast agent at high frequencies. A second factor may be the transducer sensitivity at 40 MHz, which may result in the detection of signals at lower transmit pressures. Thirdly, it may relate to differences in the development of second harmonic content between the two different beams. Finally, the use of pulse averaging in this study as opposed to single pulses for image lines employed in the previous study may have contributed to improving SNR at reduced transmit amplitudes.

It has also been shown that it is possible to generate subharmonics at a transmit frequency of 40 MHz. The rise of a detectable subharmonic as a function of pressure is consistent with the results of Goertz et al. (2006b). The ability of SH20 imaging to improve CTR is consistent with previous results obtained at lower frequencies (Forsberg et al., 2000), and at 20 and 30 MHz with Definity^{TM} (Goertz et al., 2005a). The absence of tissue propagation harmonics in the subharmonic frequency region circumvents the second harmonic problem of CTR degradation with increasing transmit pressure (Shankar et al., 1998).

The results have shown that it is possible to perform nonlinear imaging with a single element unfocused IVUS transducer. With the particular harmonic imaging approach used in this study, it would be beneficial to investigate the use of specialized broad bandwidth

or multiple frequency peak transducers. Such transducers may enable improvements in axial resolution and improve SNR. A prototype IVUS transducer element has been developed for this purpose (chapter 5). Alternatively, it may also be possible to employ detection strategies that detect nonlinear bubble behavior within the transmit frequency band (e.g. Brock-Fisher et al., 1996; Shen and Li, 2003).

This study was restricted to the use of an experimental micrometer to submicrometer sized lipid encapsulated contrast agent. It is also of interest to examine the performance of nonlinear IVUS contrast imaging with current approved contrast agents. With such agents, it may be useful to modify the native size distributions through, for example, decantation (Goertz et al., 2003a). Alternatively, it may also be fruitful to examine other agent detection strategies such as those combining low and high frequencies (e.g. Kruse et al., 2003; Hansen, 2004; Bouakaz and De Jong, 2004). Such approaches will require more substantial modifications to existing commercial instrumentation platforms than for harmonic IVUS.

A key issue for the performance of harmonic IVUS contrast *in vivo* will be the concentration of agent that can be realized within the imaging plane. For IVUS detection of agent in coronary lumen or coronary *vasa vasorum*, it will be possible to locally inject agent through a catheter upstream of the region of interest. This may enable the attainment of much higher local concentrations of agent than can be achieved with conventional contrast imaging scans involving systemic agent administration. First results of *in vivo* experiments in atherosclerotic rabbit aortas can be found in chapter 9.

This study has presented an investigation of the feasibility of nonlinear contrast agent imaging with an experimental contrast agent. The imaging results indicate that it is possible to perform both second harmonic and subharmonic contrast agent imaging with IVUS instrumentation. This approach may be a means for improving vessel lumen boundary detection and in enabling a new clinical application of IVUS *vasa vasorum* imaging.

Chapter 9

Contrast Harmonic Intravascular Ultrasound: a feasibility study for vasa vasorum imaging

Based on the publication *"Contrast Harmonic Intravascular Ultrasound: a Feasibility Study for Vasa Vasorum Imaging "* by Goertz D.E., Frijlink M.E., Tempel D., Van Damme L.C.A., Krams R., Schaar J.A., Ten Cate F.J., Serruys P.W., De Jong N. and Van der Steen A.F.W., Invest Radiology, 41(8):631–2422, 2006.

Abstract – The objective of this study was to investigate the feasibility of *vasa vasorum* imaging using contrast harmonic intravascular ultrasound (IVUS). Prototype IVUS instrumentation was developed for the sensitive detection of microbubble contrast agents. Harmonic imaging involved transmitting ultrasound at 20 MHz (fundamental) and detecting contrast signals at 40 MHz (second harmonic). Phantom experiments were conducted to investigate the detection of a small vessel in the wall surrounding a larger vessel. *In vivo* experiments were conducted in atherosclerotic rabbit abdominal aortas. The phantom experiments showed improved small vessel detection in harmonic mode relative to fundamental mode. For the *in vivo* experiments, harmonic imaging enabled the visualization of contrast agent outside the aortic lumen through a statistically significant ($p<0.001$) enhancement of image power, consistent with the detection of adventitial microvessels. These microvessels were not detected in fundamental imaging mode. These results indicate the feasibility of harmonic intravascular contrast ultrasound as a

new technique for vasa vasorum imaging.

9.1 Introduction

There is increasing evidence that the *vasa vasorum* play an important role in atherosclerotic plaque pathogenesis and stability (Barger et al., 1984; Zamir and Silver, 1985). It is well established that pathologic neovascularization occurs during plaque development and that the resulting microvessels have abnormal spatial distributions and branching patterns (Zhang et al., 1993; Kwon et al., 1998). Neovascular *vasa vasorum* are correlated with the presence of inflammatory cells and infiltrate within plaques (Kumamoto et al., 1995; de Boer et al., 1999) and are implicated in a positive feedback loop of inflammation and angiogenesis (Moulton et al., 2003). Plaque neovessels have been associated with intraplaque hemorrhage and thereby to rupture (Milei et al., 1998; Kolodgie et al., 2003). Elevated plaque microvessel counts have been found in the coronary arteries of patients with acute myocardial infarctions (Barger and Beeuwkes, 1990; Tenaglia et al., 1998) and in the carotid arteries of those with symptomatic carotid occlusive disease (Mofidi et al., 2001).

Therefore, a rapidly growing demand exists for the development of sensitive, robust and quantitative techniques for *in vivo* and clinical imaging of the *vasa vasorum*. Such techniques can potentially contribute to the identification of vulnerable plaques (Schaar et al., 2004) and in monitoring therapeutic response. Because of the heterogeneous nature of plaque *vasa vasorum* and the potential significance localized measures of vascularization as markers of vulnerability (Moreno et al., 2004), high-resolution imaging also may be required. In an *ex vivo* setting, microCT techniques are capable of generating high-resolution images of coronary *vasa vasorum* in animal studies and have provided considerable insight into their structure and function (Jorgensen et al., 1998; Herrmann et al., 2001; Gossl et al., 2003). In the carotid artery, contrast-enhanced MRI (Kerwin et al., 2003) and transcutaneous contrast ultrasound (Feinstein, 2004) have been shown to be sensitive to plaque neovascularization. While signs of plaque "blush" are sometimes evident with angiography (Casscells et al., 2003), there are no established clinical techniques for examining coronary artery *vasa vasorum* with high resolution and sensitivity.

At present, IVUS is not established as a tool for imaging vasa vasorum. High frequency (20–50 MHz) transcutaneous ultrasound flow imaging systems designed for ophthalmology and small animal imaging have been shown to be capable of detecting and monitoring neovascular blood flow (Goertz et al., 2002). However, issues of tissue motion will likely render such approaches ineffective for IVUS vasa vasorum imaging in the coronary arteries, as their performance degrades rapidly when tissue velocities approach or exceed those of blood. IVUS imaging systems developed to examine flow within the

lumen of larger arteries (Li et al., 1998) appear not to be capable of detecting *vasa vasorum*. It has recently been reported that bolus injections of contrast agents can give rise to IVUS echogenicity enhancement in the adventitia of coronary arteries, consistent with the detection of *vasa vasorum* (Carlier et al., 2005). However, this approach is restricted to a single imaging plane and assumes that images acquired at the same point of successive cardiac cycles are not affected by tissue motion.

At low ultrasound frequencies (2–5 MHz), the use of microbubble contrast agents has enabled the detection of microvascular blood flow by employing techniques that cause the echoes from bubbles to be substantially different to those from tissue (Goldberg, 2001). One means of achieving this is through second harmonic imaging, which stimulates substantial bubble vibrations to emit energy at twice the transmitted frequency. Commercial contrast agents are therefore designed to be comprised primarily of bubble sizes that resonate in the 2–5 MHz diagnostic ultrasound frequency range (2–6 microns in diameter) (Gorce et al., 2000). It has been generally assumed that it is not possible to conduct harmonic imaging at high ultrasound frequencies (Cachard et al., 1997; Li et al., 1998; Moran et al., 2002). However, contrast harmonic imaging of microvessels was recently demonstrated at 20 MHz by Goertz et al. (2005a) using instrumentation and extracorporeal transducers compatible with applications in ophthalmology and small animal imaging.

We hypothesize that harmonic imaging of microbubble contrast agents with IVUS may be a technique to enable *vasa vasorum* imaging and have developed novel instrumentation for this purpose (Frijlink et al., 2004; Goertz et al., 2004). In this study, the feasibility of using contrast harmonic IVUS imaging to detect *vasa vasorum* is investigated in small vessel flow phantom experiments and in atherosclerotic rabbit aortas.

9.2 Materials and Methods

System overview

The technical details of the prototype IVUS system are described in section 2.3. The transmitted ultrasound pulses were centered at 20 MHz, and the receive frequency range of interest was centered at 40 MHz. Raw ultrasound data was recorded at 200 megasamples/second and processed off-line on a personal computer using custom designed software. Both fundamental and harmonic signals were extracted from each data set with RF-processing, followed by envelope reconstruction to form 300 image lines of approximately 6 mm in depth. The frame rate was 5 Hz and data from alternate image frames could be recorded for processing. The system has been evaluated with a 30 MHz catheter (DuMed, Rotterdam, Netherlands) with its transducer element replaced by a custom made element designed for second harmonic imaging at 20 and 40 MHz (chapter 5). A

sequence of alternate image frames was acquired during the course of one minute, beginning several seconds before a bolus injection of contrast agent upstream of the imaging plane.

Contrast agents

The results were obtained with the commercially available contrast agent Definity™ (Bristol-Myers Squibb Inc., New York, NY). Agent was decanted within the vial for 10 to 15 minutes and 0.5 ml was extracted and diluted in 2.0 ml of 0.9% saline. The decantation procedure preferentially removed larger bubbles, which are less responsive at high ultrasound frequencies and therefore not expected to contribute as significantly to second harmonic signals. A Coulter counter (Multisizer 3, Beckman Coulter Inc., Fullerton, CA) was used to measure the size distribution of native and decanted agent samples. The decantation process was found to modify the mean (volume weighted) bubble diameter from 3.02 to 1.36 microns, and reduced the volume fraction of bubbles by 42%. The concentration in the injected suspension was estimated to be 2.5×10^9 bubbles per milliliter.

Phantom experiments

A flow phantom was constructed to investigate the visualization of a small "adventitial" vessel outside a larger artery after the release of a bolus of contrast. The phantom consisted of a 4-mm main lumen surrounded by tissue mimicking phantom material (Goertz et al., 2004). A 0.75-mm diameter adventitial vessel branched off the main lumen at an angle of 15 degrees in the downstream direction. The mean flow velocities within the 4-mm vessel and 0.75-mm vessel were 20 cm/s and 0.2 cm/s respectively. The IVUS transducer was situated within the main lumen distal from the branch point, creating an image plane that included the small vessel. A 5-French delivery catheter was situated 4 cm upstream from the transducer. Agent was released (2 ml of 20% concentration decanted agent) over 3 seconds and IVUS data was recorded for 1 minute following the bolus. Quantification of signal power was performed in a 0.5 mm square region of interest (ROI) located within the small vessel and tissue regions to estimate the contrast-to-tissue ratio (CTR) in decibels (dB), where a higher CTR indicates improved specificity of contrast agent detection. Note that in this study blood mimicking scatterers have not been employed, which facilitated the detection of agent arrival within the vessels.

In vivo experiments

In vivo studies were conducted in atherosclerotic rabbit abdominal aortas. Atherosclerosis was initiated using endothelial cell injury procedures followed by a high cholesterol diet (Schaar et al., 2005). Experiments were performed 10–11 weeks after initiation

of atherosclerosis. With Definity™, a total of 8 data sets from 3 atherosclerotic rabbits were acquired. Experiments began with an examination of the abdominal aorta using 3D pull back of a 40-MHz CIVUS© system (Boston Scientific Inc., Freemont, CA), to confirm the presence and extent of the atherosclerotic plaque within the aorta. After this, the harmonic IVUS catheter was advanced through the femoral artery and positioned within the atherosclerotic aorta. The IVUS catheter tip was situated at locations within 2 to 10 mm below a limbic artery branch, which facilitated the colocalization of images and subsequent histologic sections. The agent delivery catheter was advanced through the carotid artery and its tip was located approximately 1 cm below the lower renal artery. To confirm that the delivery catheter was in a position that enabled injected microbubble contrast agent to enter the *vasa vasorum*, a bolus of radiopaque contrast was first released and monitored with angiography. Radiopaque contrast was observed to be present within the abdominal aorta and limbic arteries following the injection. Figure 9.1 shows an angiogram following a bolus release of radiopaque contrast, where limbic arteries, the IVUS catheter and delivery catheter can be visualized. Limbic artery branch points are marked with needles that are subsequently employed to guide tissue harvesting.

Ultrasound contrast agent injections were then performed using 2-ml boluses (of 20% agent concentration) released over 3 seconds. All experiments were conducted in accordance with institutional regulations and the "Guide for the care and use of laboratory

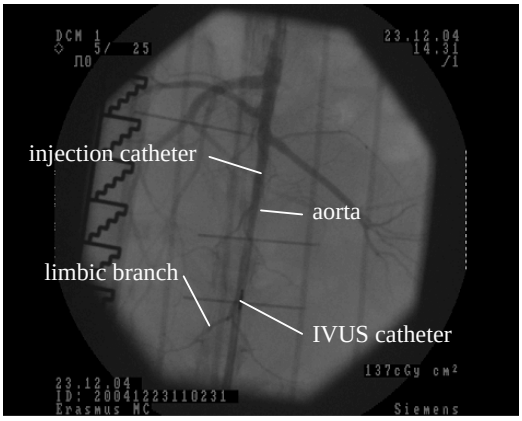

Figure 9.1: Contrast angiogram of rabbit abdominal aorta indicating experimental configuration. An IVUS catheter is introduced through the femoral artery and situated in the vicinity of a limbic artery. A delivery catheter is introduced through the carotid artery an its tip is positioned below the lower renal artery. Scale is indicated by 1 cm markers at left of the image.

animals" as approved by the Council of the American Physiological Society.

Quantification of *in vivo* experiments

A quantification of adventitial second harmonic contrast enhancement was performed by integrating the signal power within a region of interest outside the main aortic lumen. Custom software was first used to manually demarcate a contour defining the lumen boundary in the harmonic images. As will be discussed later, this could be readily achieved due to the presence of a small ring of agent enhancement at the lumen boundary, and the absence of agent within the plaque itself. The depth extent of the region of interest in axial direction was selected to be 1.5 mm which, based on histology, was sufficient to include microvessels that would be considered to be *vasa vasorum* (Edelman et al., 1992; Kwon et al., 1998; Herrmann et al., 2001). Circumferentially, the region of interest subtended an arc of 270 degrees, with its center opposite to the vena cava. This ROI limitation was imposed in order to exclude the vena cava from the analysis, since the purpose of the study was to assess enhancement in small extraluminal vessels. Within the region of interest the power of the envelope of the ultrasound signals was summed on a pixel basis. To obtain a baseline measurement, the power integration procedure was averaged over 4 consecutive image frames immediately prior to agent injection. A post-injection enhancement measurement was obtained from an averaged measurement of 4 consecutive frames at the peak of post-injection adventitial harmonic enhancement (occurring typically at 5 to 15 seconds post-injection). The non-zero baseline measurement of power was primarily due to system electronic noise. The mean and standard deviation of the contrast enhancement was calculated by taking the ratio of baseline and post-injection powers. A Mann-Whitney U test (two-tailed) was then used to test for the significance of difference between the baseline and contrast enhanced measurements.

Histology

After IVUS experiments, the animals were euthanized and 2-cm long sections of tissue, including the aorta, vena cava, and surrounding tissue, were harvested to include the IVUS imaged region. The tissue was fixed for 24 hours in 4% formalin/phosphate-buffered saline (PBS), and subsequently processed through a graded alcohol series, xylenes, and was then paraffin-embedded. A series of 5 sections, each 5 μm thick, were taken at locations every 300 μm to gain insight into the tissue appearance in the vicinity of the imaging plane. Sections were mounted on Superfrost plus (Menzel-Gläser) glass slides. At each location, one slide underwent routine hematoxylin/eosin (HE) staining, which was performed on formalin-fixed paraffin-embedded sections. A second slide underwent endothelial cell staining (CD31 staining).

9.3 Results

Phantom experiments

Phantom results are shown in fig. 9.2 for fundamental and harmonic imaging modes. Prior to agent injection, the fundamental images clearly show the main vessel lumen. The small adventitial vessel can also be resolved at 8 o'clock, though it should be noted that *in vivo* the presence of echoes from blood within a small vessel would act to inhibit its detection. Following the contrast injection, the high agent concentration in the bolus transiently obscured imaging through attenuation effects as it passes the transducer within the main lumen. Beginning at approximately 5 to 7 seconds post-injection, agent arrived within the adventitial vessel, which was difficult to resolve due to similar echogenicity of the agent and tissue. An image at 10 seconds after injection. In harmonic mode, the tissue signals were largely suppressed. Following injection, agent could be seen within the main lumen and, after a delay, the adventitial microvessel was readily visualized. An example at 10 seconds after injection, where the vessel was detected with a CTR of 14 dB. Note that a ring of enhancement remained at the periphery of the main lumen, which may be due primarily to increased clearance times caused by lower flow velocities near the vessel wall. Since the fluid speed within a vessel goes to zero near the wall and will be the highest in the vessel center, this will spatially and temporally elongate the bolus. Therefore, the contrast agent situated towards the wall will arrive later and take a longer time to pass.

In vivo experiments

Example *in vivo* results are shown in fig. 9.3 for fundamental and harmonic imaging modes. In fundamental mode before injection, the vena cava can be seen at 10 o'clock, whereas the main aortic lumen boundary and plaque are difficult to visualize. Following contrast injection, the passage of the bolus transiently obscured imaging through attenuation effects and by 5 seconds post-injection the intensity of the image had recovered. Echogenicity enhancement was then evident in the vena cava, but was not apparent in the adventitia, except in a small region at the 4 o'clock. The harmonic imaging results are substantially different. Before injection, it can be seen that the tissue signals have been largely suppressed, with only a small amount of tissue signal artifact remaining. Post-injection, agent was first visualized in the main lumen. By approximately 5 seconds after injection, a ring at the boundary of the main lumen could be viewed, which is consistent with that observed in the phantom experiments and can be attributed to the presence of a small amount of more slowly moving agent adjacent to the aortic wall. This effect enabled the lumen boundary to be easily distinguished. There was then an eccentric circumferential region devoid of enhancement, with a thickness larger in the 2-o'clock direction than in the 8-o'clock direction. Outside this hypoechogenic region,

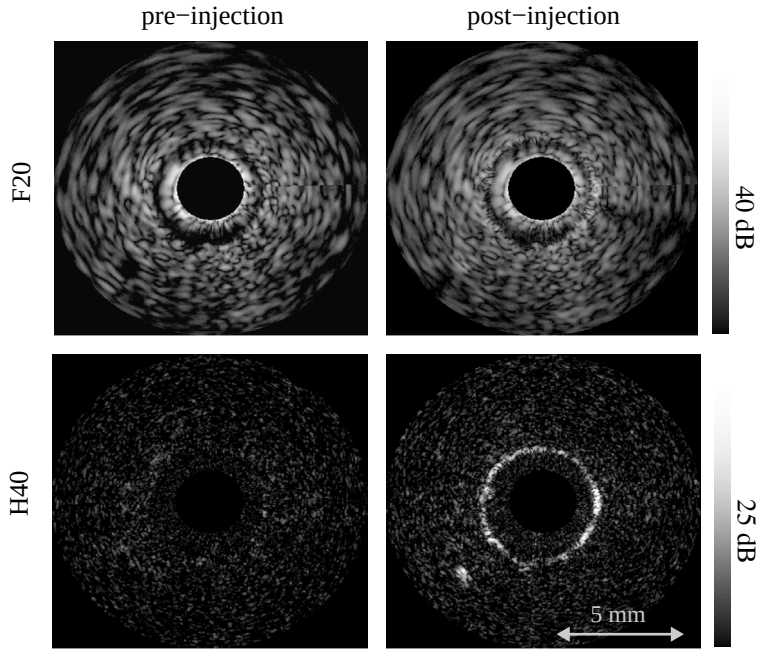

Figure 9.2: Phantom results using decanted Definity™. F20 prior to agent injection visualizes the main lumen and small vessel ("v"). The signal immediately surrounding the catheter is a sheath artifact. F20 post-injection shows that the adventitial vessel is difficult to visualize. Post-injection H40 mode detects the adventitial vessel.

numerous locations of enhancement were observed that are associated with the presence of agent. Although toward 10 o'clock the enhancement is associated with vena cava, the other locations are consistent with the detection of microvessels outside the main vessel lumen.

Histology

A number of issues prohibit the precise co-registration of IVUS images and histologic sections that might enable a direct comparison of image vascularity with that indicated by histology. Foremost are uncertainties in IVUS imaging plane orientation and location relative to the extracted tissue, the presence of tissue deformation and shrinkage, and that the IVUS imaging "plane" is a flattened cone rather than a true plane. Further, because of the spatial scale of the microvasculature, a single thin histologic section is not capable of providing insight into all microvasculature present within the thicker IVUS imaging

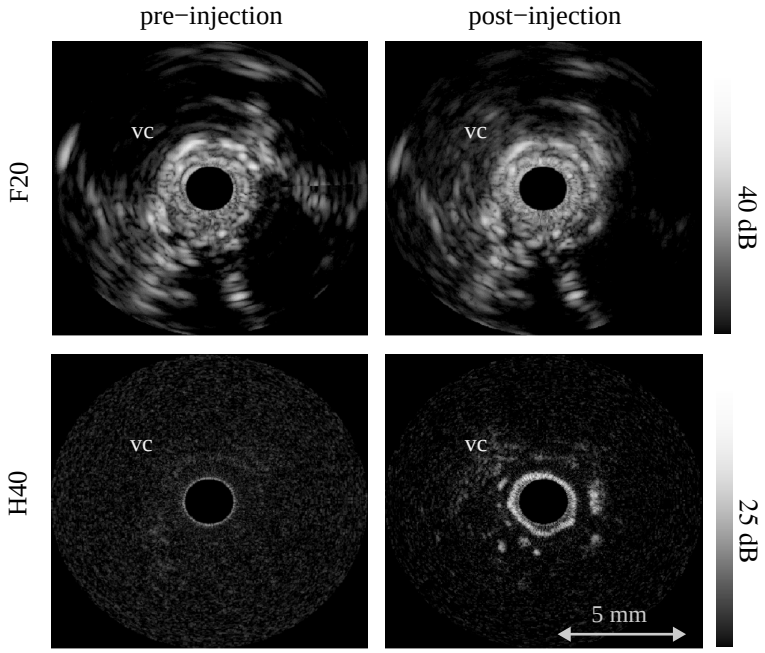

Figure 9.3: *In vivo* results in an atherosclerotic rabbit aorta using decanted Definity™. F20 prior to agent injection visualizes the main lumen and vena cava ("vc"). F20 post-injection show no evident changes in adventitial enhancement, except for in a region at 4 o'clock and within the vena cava. H40 pre-injection shows the tissue signals to be largely suppressed. 10 second post-injection H40 mode shows significant adventitial enhancement, consistent with the detection of adventitial microvessels.

volume. Because of these factors, histology is therefore used to establish general plaque features and the relative location and character of extraluminal vascularity that is present in vicinity of the imaging plane. Example histologic sections from this aorta are shown in fig. 9.4 for HE and CD31 staining respectively.

The HE stained section shows the presence of a large, eccentric plaque within the aorta. The plaque thins towards the 7-o'clock position and the vena cava is situated to the left of the aorta. Accounting for the different orientation of the histology sections, these features generally are consistent with the IVUS images. CD31 staining revealed the plaque to be avascular, and the media also had very little evidence of the presence of blood vessels. Contrast enhancement of harmonic IVUS images between the lumen and adventitial regions would therefore not be expected and, in fact, was not observed. Within

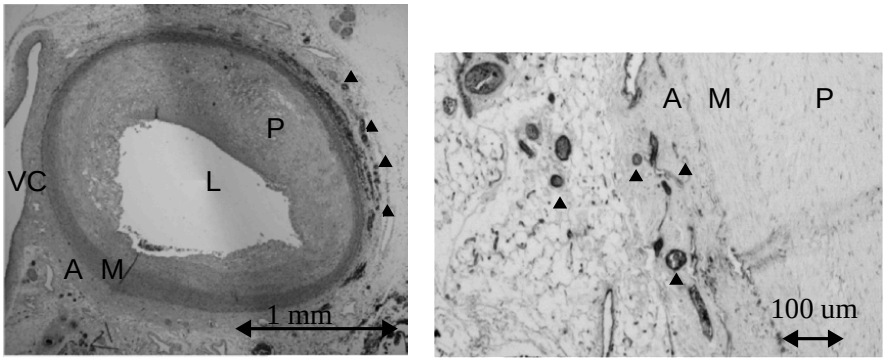

Figure 9.4: Overview hematoxylin/eosin stained section (left) from the aorta examined with IVUS in fig. 9.3. "VC" is the vena cava, "L" the aortic lumen, "M" the media, "P" the atherosclerotic plaque and "A" the adventitia. A large eccentric plaque is evident. CD31 stained section (right) highlights endothelial cells and reveals the presence of numerous adventitial microvessels (many containing erythrocytes), some examples of which are denoted with ▲.

the adventitia, extensive evidence was found of microvessels, particularly towards the bottom and right. The histology therefore indicates the general presence of microvessels in regions where harmonic IVUS has detected contrast enhancement. Although a specific comparison between histology microvessels and IVUS images cannot be made, these results do support the conclusion that harmonic IVUS has detected adventitial microvessels.

Quantitative analysis

A quantitative analysis for the imaging results was performed as described in the methods sections. Referring to fig. 9.4, a region of interest was selected to have its inner contour selected to be just outside the ring of enhancement at the boundary of the lumen, and within the hypoechogenic region corresponding to the avascular plaque. A total of 8 data sets were analyzed. The mean relative contrast enhancement in the region of interest was found to be 2.6±0.63. The pre- and post-injection power measurements were found to be significantly different ($p<0.001$).

9.4 Discussion

In the present study, the objective was to detect a small "adventitial" vessel in a controlled phantom experiment and to investigate the feasibility of *in vivo vasa vasorum*

detection. Both the phantom and *in vivo* results indicated the primary bolus passage through the main lumen and then a delayed enhancement in adventitial microvessels. The vessels were not detected using conventional fundamental mode imaging. In the phantom experiments, the delay was associated with the slower velocity and longer path length relative to the main vessel lumen. *In vivo*, such a pattern is consistent with the delay that would be induced by the longer traveling distance and slower blood velocities within the *vasa vasorum*. From serial histologic sectioning it was established that, aside from the vena cava, only microvessels were present within the adventitia, thereby confirming that extraluminal microvessels were detected. Following the convention detailed by Kwon et al. (1998) and Edelman et al. (1992), these results indicated the presence of *vasa vasorum*. The results of this study therefore indicate the feasibility of imaging microvessels using harmonic IVUS contrast imaging.

For any vascular imaging modality, the appearance of small vessels in an image is determined in large part by the spatial resolution of the system relative to the vessel sizes and spacing. In the microcirculation, vessel calibers are considered to range from 5 up to 100 to 300 μm in diameter, and reports of the *vasa vasorum* appear to fall within this range (Kumamoto et al., 1995; Kwon et al., 1998; Herrmann et al., 2001). In the case of clinical MRI and low-frequency contrast ultrasound, spatial resolution is typically on the order of a cubic millimeter or more. Imaging voxels of this size generally will contain a large number of microvessels that cannot be individually resolved. Although these modalities are sensitive to microvascular flow, they map "perfusion" at a relatively coarse scale and the images cannot be used to directly visualize or examine microvascular morphology. Consistent with this, the results of these modalities for carotid *vasa vasorum* imaging indicate a spatially diffuse enhancement outside the main lumen following contrast injection (Kerwin et al., 2003; Feinstein, 2004). With *ex vivo* microCT studies of the *vasa vasorum*, imaging voxels ranging from 20 to 42 μm have been used (Kwon et al., 1998; Herrmann et al., 2001; Gossl et al., 2003; Kerwin et al., 2003). As indicated by Jorgensen et al. (1998), when objects become smaller and approach the voxel size, they appear larger than their actual sizes and are eventually rendered undetectable due to sensitivity issues. *Vasa vasorum* less than 50 to 60 μm in diameter appear not to have been reported with microCT imaging. For the harmonic IVUS system reported, the resolution is on the order of larger microvessel diameters. Detected vessels that are smaller than this voxel size will appear to be larger than their actual size. This effect was demonstrated with high-frequency ultrasound in the absence of contrast by Roelandt et al. (1994), where known vessel sizes were effectively blurred and enlarged to the resolution size. If multiple vessels are present within an imaging voxel then they will not be individually resolved and will appear as a larger cluster. It is also possible that the smallest vessels are simply not detected because of either sensitivity limitations of the system, or insufficient uptake of agent within the *vasa vasorum*. Qualitatively, the enhancement took a similar form to that of two-dimensional microCT images of the

vessel wall in that numerous discrete locations of vascularity were observed.

It is notable that the results of this report were derived from data acquired during a single catheter rotation, an approach offering several advantages over procedures that rely upon comparing multiple image frames to detect changes in echogenicity following a bolus injection (Carlier et al., 2005). First, the harmonic approach is not susceptible to inter-frame motion artifacts. Second, because it is not necessary for the catheter to be stationary for an entire bolus passage, this approach can be readily adapted to three-dimensional imaging. Three-dimensional IVUS imaging has been previously implemented using transducer pullback procedures (Roelandt et al., 1994). Volumetric acquisitions are anticipated to be central to the utility of IVUS *vasa vasorum* imaging because of the highly heterogeneous spatial distribution of *vasa vasorum*. Specifically, this will be necessary to enable spatial analyses of the vasculature such as those performed using microCT. Further, it will also be necessary to effectively detect localized regions of vascularity and to establish their spatial relation to plaque and vessel wall structures. Such information may be relevant as an indicator of plaque vulnerability (Moreno et al., 2004).

Previous *in vitro* demonstrations of this technique were conducted with an experimental small bubble agent, which is designed for use at high frequencies (Goertz et al., 2006a). It is significant that adventitial microvessels were observed with a clinically approved agent not designed for use at high frequencies, because this will facilitate the clinical adaptation of these approaches. Further, the instrumentation used in this study is also appropriate to image targeted microbubbles for the purposes of molecular imaging which may provide an alternative means by which to image neovascular *vasa vasorum* (Winter et al., 2003).

The purpose of this work was to demonstrate the feasibility of *vasa vasorum* detection with contrast harmonic IVUS imaging. One limitation of this study was a limited comparison with other microvascular detection techniques. Due to the absence of high resolution *in vivo* imaging techniques, future work will necessarily entail comparisons with histology, microsphere deposition and *ex vivo* microCT analysis. In such studies, issues of sensitivity and quantification must be addressed. One aspect of quantification will be to integrate signals both volumetrically, and within specific regions of interest as a function of time after injection. It is also of interest to analyze aspects of the spatial distribution of *vasa vasorum*, such as branching patterns and the location of vascularization with respect to wall and plaque structures. A model of particular interest for such experiments will be atherosclerotic pig coronaries, with which it will be relevant to perform longitudinal monitoring of both control and cholesterol fed animals.

A second limitation of this study is that the instrumentation is not clinically approved

at present and is therefore restricted to use in animal experiments. Despite recent advances, a great deal remains unknown about the specific mechanisms of *vasa vasorum* involvement in the progression and instability of plaques. Within this context, harmonic IVUS contrast imaging is suitable for longitudinal studies of the role of vasa vasorum in pathogenesis of atherosclerosis as well as for preclinical therapeutic studies. Such experiments may be particularly relevant due to the lack of other techniques capable of *in vivo* high resolution monitoring of *vasa vasorum*, and should also provide a foundation for understanding the potential role and limitations of contrast harmonic IVUS in future clinical applications.

Chapter 10

Discussion and conclusions

10.1 Introduction

In the last decade, intravascular ultrasound (IVUS) has become an important clinical tool for the detection and evaluation of atherosclerotic lesions, for therapy guidance and for clinical research. Although second-harmonic ultrasound imaging is used more and more in conventional diagnostic ultrasound (1–10 MHz) to suppress image artifacts, to enhance image quality and to increase contrast detection at low frequencies, little work has been done to assess potential benefits of harmonic imaging in IVUS. The work presented in this thesis was done to show the feasibility of harmonic IVUS, to demonstrate its inherent benefits and to indicate potential clinical applications.

When compared to other vascular imaging modalities, intravascular ultrasound has several advantages for the detection of atherosclerotic lesions. This minimally-invasive technique results in high resolution 3D tomographic images with a penetration depth of 5–10 mm, and no need for saline flushing or balloon occlusion. The spatial resolution is not high enough to directly visualize thin fibrous caps of vulnerable plaques, but additional information on both mechanical properties of the vessel wall (IVUS elastography / palpography) and perfusion of atherosclerotic lesions (chapter 9) might be obtained with a single IVUS catheter. This makes harmonic IVUS a promising diagnostic tool for vulnerable plaque detection.

The following sections summarizes and discusses the most important findings of each chapter. Future directions of harmonic IVUS are discussed subsequently.

10.2 General discussion

In order to experimentally test the feasibility and potential advantages of tissue and contrast harmonic imaging at intravascular ultrasound frequencies, a measurement setup was constructed. First results with this experimental setup showed that tissue harmonic imaging (THI) could reduce image artifacts from a reflective metal stent in the near field of a focused ultrasound beam of an ultrasound biomicroscopy transducer (chapter 3). Although experiments showed that an unfocused IVUS transducer mounted on a needle-tip could also generate and detect a second harmonic 40 MHz beam, imaging results did not show an obvious reduction in stent imaging artifacts. However, THI indicated to improve the delineation of a stent close to an unfocused IVUS transducer.

The prototype harmonic IVUS system was used in a subsequent study to demonstrate the feasibility of IVUS THI both in a phantom and *in vivo*, using a conventional single-element rotating IVUS catheter (chapter 4). This study also showed the potential of THI to reduce image artifacts in situations where no stents were involved. First, the combined effect of amplifier saturation and the reflective sheath surrounding the catheter element, displayed as a white ring close to the transducer, was reduced in harmonic acquisitions. This finding was consistent with nonlinear simulations and 2D beam profile measurements, both showing a relatively lower near-field energy in the harmonic beam compared to fundamental beams. Second, the decay of signal strength as a function of depth was less pronounced in harmonic mode than in both fundamental modes. This was also consistent with nonlinear simulations and hydrophone measurements. In *in vivo* experiments the signal decay of harmonic acquisitions will be a function of the combined effects of beam diffraction and tissue properties like nonlinear coefficients and frequency dependent attenuation. Nonlinear simulations through a medium with realistic tissue properties indicated that absolute far-field pressures of a second harmonic 40 MHz beam and a fundamental 40 MHz beam, both generated with an identically shaped unfocused IVUS transducer, can be comparable. This means that the effective penetration depth, which is determined by absolute pressure levels, of a 40 MHz harmonic beam could be similar to that of a fundamental beam excited at 40 MHz.

Since it was expected that an ultrasound transducer optimized for harmonic IVUS could facilitate harmonic IVUS imaging by efficient transmission at the fundamental frequency and sensitive detection at the second harmonic frequency, a new IVUS element was designed, fabricated and characterized (chapter 5). This element has been designed for harmonic imaging in the 20–40 MHz range, showing a frequency response with two peaks around 20 and 40 MHz as caused by a dual-layer structure consisting of an active piezo layer and a passive resonant layer. This dual-frequency element increased its sensitivity in the vicinity of 20 MHz, compared to a single-layer conventional IVUS element. For second harmonic contrast imaging, it was found that lower transmit pressure

levels were required to produce improvements in contrast to tissue ratio with an IVUS transducer, in order to avoid propagation harmonics. In this case, an improved sensitivity peak at 40 MHz would likely be advantageous.

An adapted version of the custom-made dual-frequency IVUS element was then mounted on a conventional catheter (chapter 6). This version omitted the mismatching layer and the passive resonant layer was changed from aluminum to tin, which was then electroplated in stead of glued. This dual-frequency catheter was evaluated and compared with a conventional IVUS catheter using the prototype Harmonic IVUS system under conditions relevant to tissue harmonic IVUS. Characterization experiments showed the dual-frequency catheter to have improved transmit efficiency at 20 MHz. Under similar circumstances in both a tissue mimicking phantom and in rabbit aortas *in vivo*, harmonic imaging experiments with this catheter therefore resulted in increased SNRs. Although the SNR was shown to be higher with the dual-frequency catheter, the lateral and axial resolution, which are dependent on the shape and frequency response of the transducer, were not discussed. When dual-frequency elements will be mounted on current clinically used catheters, it will be useful to assess improvements in IVUS image quality compared to "single-frequency" catheters.

A simulation tool was developed to investigate nonlinear IVUS beams, and to evaluate the influence of transducer rotation and axial catheter-to-tissue motion on the efficiency of Pulse Inversion (PI) signal processing (chapter 7). When PI is applied, a simulation study with this model showed that fundamental signal suppression of >25 dB is realizable for inter-pulse angles of 0.15°. This inter-pulse angle is can be used at clinical IVUS frame rates, namely 2400 pulses per rotation at a rotation speed of 30 Hz. The effect of axial tissue-to-catheter motion on the average fundamental signal suppression was considered to be of little influence for pulse-repetition frequencies of 12.5 kHz. These simulation results are consistent with fundamental suppression levels as presented in chapter 8, and support the application of PI as used in chapter 4 and 6.

Chapter 8 showed the first results of nonlinear contrast imaging with IVUS instrumentation. The feasibility of both subharmonic and second harmonic imaging of an experimental micrometer to sub-micrometer sized lipid-encapsulated contrast agent was presented. Initial subharmonic imaging experiments with an IVUS catheter suggested increased contrast-to-tissue ratios for increased fundamental pressures, whereas for second harmonic imaging the contrast-to-tissue ratios degraded with higher pressures, due to increasing nonlinear propagation. Both subharmonic and second harmonic contrast detection may be a means for improving vessel lumen boundary detection and may enable a new clinical application of IVUS *vasa vasorum* imaging.

Second harmonic contrast IVUS imaging has been shown to be feasible *in vivo* (chapter

9). Adventitial microvessels surrounding the aorta of an atherosclerotic rabbit were imaged by means of nonlinear detection of a modified clinically approved contrast agent with the prototype harmonic IVUS system. These adventitial microvessels were not detected using conventional fundamental mode imaging. Contrast harmonic IVUS is therefore a promising technique for the *in vivo* visualization of *vasa vasorum*, which structure may indicate the vulnerability of atherosclerotic plaques.

10.3 Future directions

It has been shown that the development of a sensitive IVUS transducer that was optimized for 20 to 40 MHz harmonic imaging resulted in an increased SNR in THI acquisitions. A different transducer design, based on piezoelectric materials or capacitive micro-machined ultrasonic transducers (CMUTs) might lead to an even further increased sensitivity. The relatively new and continuously developing CMUT technology offers great advantages over the traditional ferroelectric-based transducers such as very wide bandwidth, ease of fabrication of complex two-dimensional arrays, and potential integration with electronics. It may be expected that CMUTs ultimately will replace ferroelectric materials in IVUS catheters. Harmonic IVUS applications might especially profit from small transducers with good sensitivity over a wide bandwidth. However, specific concerns like limited pressure output (Bayram et al., 2005) and excitation of harmonics in transmission (Zhou et al., 2004) need to be addressed.

Static and dynamic focusing could potentially be implemented with CMUT technology in a single-element configuration, where many small CMUT-cells form one IVUS element. The effect of focused IVUS beams, as opposed to beams from unfocused IVUS elements as reported in this thesis, may have a beneficial effect on harmonic IVUS imaging. The harmonic field can build up faster in a stronger focused beam, which could lead to an increased SNR of harmonic acquisitions, and an increased lateral resolution around the focus. Future research might focus on the differences in harmonic fields and resulting image quality of harmonic acquisitions between focused and unfocused IVUS elements.

The results presented in this thesis showed not only the feasibility of THI but also the potential to improve image quality at IVUS frequencies. THI resulted in the reduction of near-field artifacts in images acquired *in vivo* with a single-element conventional IVUS catheter. However, this relatively large and stiff IVUS catheter is not clinically approved for the diagnosis of atherosclerotic lesions in coronary arteries. In addition, the sheath covering the IVUS transducer could be considered thick compared to the sheath of current commercially available catheters. It was this sheath that caused relatively high-amplitude reflections and other undesired artifacts in IVUS images. For future clinical approval of harmonic IVUS, it is therefore of utmost importance to collaborate

with IVUS catheter and system manufacturers. Since the image quality and image artifacts are partially dependent on the geometry and characteristics of the IVUS catheter and transducer, future research should aim at optimizing currently used catheters for harmonic IVUS. Further studies should subsequently quantify the reduction of image artifacts with THI as compared to fundamental IVUS.

Although current IVUS systems in general consist of almost all components that are necessary to perform harmonic IVUS imaging, optimization and tuning is necessary in order to be able to discriminate ultrasound responses in the frequency domain. As a first step, the combination of relatively narrow-band excitation pulses and analog filtering could result in initial harmonic IVUS imaging results on existing IVUS platforms. However, a second step involves the implementation of excitation pulse sequences like pulse inversion in combination with flexible signal processing possibilities. These system changes could lead to increased spatial resolution, enhanced signal-to-noise ratios and increased flexibility for the detection of contrast agent. The implementation of real-time second harmonic IVUS imaging will not be an issue, since similar processing is currently used in clinical 2–10 MHz systems equipped with real-time second harmonic imaging.

As indicated in section 1.4, different biological tissues have different nonlinearity coefficients. Further studies are necessary to assess the potential for THI for IVUS to estimate nonlinear tissue properties. If harmonic RF-signals could reveal Gol'dberg number estimates of tissue parts, this information could be used as an additional input for intravascular tissue or plaque characterization techniques based on self-organizing maps or statistical classification trees (Baldeweck et al., 1995; Nair et al., 2002).

Second harmonic detection of contrast agent *in vivo* has been shown to be feasible. Future work will also focus on different nonlinear contrast detection techniques for IVUS applications. For example, subharmonic detection of contrast microbubbles can lead to increasing contrast-to-tissue ratios for increasing pressures, because of the absence of tissue propagation harmonics (chapter 8 and Goertz et al. (2006a)). Another contrast detection technique, in which the tissue and contrast agent are exposed to two different frequencies, is now referred to as "radial modulation". This technique uses a low frequency pulse to manipulate high frequency scattering properties of contrast agents (Bouakaz and De Jong, 2004; Hansen, 2004). Both techniques need further investigation for their use in IVUS applications.

The feasibility of *vasa vasorum* detection with contrast harmonic IVUS imaging has been demonstrated. It is of interest to analyze aspects of the spatial distribution of *vasa vasorum*, such as branching patterns and the location of vascularization with respect to wall and 3D plaque structures. First results on the detection of targeted microbubbles with IVUS catheters were reported by Goertz et al. (2005b). The ultimate future could

be the combination of targeted contrast agent (e.g. to neovascular microvessels) with an IVUS catheter pullback using a nonlinear contrast detection technique, leading to 3D morphology of coronary arteries and surrounding vasculature. This might lead to more insight in the role of *vasa vasorum* in the pathogenesis of atherosclerosis. Collaboration between physicists, clinicians and pharmacists should be pursued to understand the potential role and limitations of tissue and contrast harmonic IVUS in future clinical applications.

10.4 Conclusions

The work reported in this thesis describes the development of a harmonic IVUS system and shows the feasibility of both tissue harmonic imaging and contrast harmonic imaging with a single-element IVUS catheter *in vivo*. Tissue harmonic IVUS imaging could suppress image artifacts that are more pronounced in conventional fundamental IVUS imaging. It was demonstrated that the development of sensitive IVUS transducers, optimized for harmonic IVUS applications, can result in an improved image quality and lead to sensitive detection of ultrasound contrast agent. Both subharmonic and second harmonic contrast agent detection have been shown *in vitro* with an experimental small-bubble contrast agent. Furthermore, pulse inversion was justified as a technique to effectively suppress the linear signal from both tissue and contrast at the fundamental frequency as acquired with a continuously-rotating IVUS catheter.

Harmonic intravascular ultrasound is a promising tool in the identification of atherosclerotic lesions in patients suffering from coronary heart disease. IVUS tissue harmonic imaging has the potential to improve image quality of diagnostic IVUS imaging. IVUS contrast harmonic imaging has the potential being a sensitive, robust and quantitative technique for *in vivo* imaging of microvasculature (e.g. *vasa vasorum*), which may contribute to the identification and monitoring of vulnerable plaques.

References

Angelsen B. A. J. *Ultrasound Imaging, Waves, Signals and Signal Processing*, volume 1. Emantec As, Trondheim, 2000.

Averkiou M. A. and Hamilton M. F. Nonlinear distortion of short pulses radiated by plane and focused circular pistons. *J Acoust Soc Am*, 102(5 Pt 1):2539–2548, 1997.

Averkiou M. A., Roundhill D. N., and Powers J. E. A new imaging technique based on the nonlinear properties of tissues. In *IEEE Ultrason Ferroelec Freq Control Symp Proc*, pages 1561–1566, 1997.

Baldeweck T., Laugier P., Herment A., and Berger G. Application of autoregressive spectral-analysis for ultrasound attenuation estimation - interest in highly attenuating medium. *IEEE Trans Ultrason Ferroelectr Freq Control*, 42(1):99–110, 1995.

Baldewsing R. A., Mastik F., Schaar J. A., and van der Steen A. F. W. A compounding method for reconstructing the heterogeneous young's modulus distribution of atherosclerotic plaques from their radial strain. *Proceedings of the Fourth International Conference on the Ultrasonic Measurement and Imaging of Tissue Elasticity*, page 68, 2005.

Baldewsing R. A., Mastik F., Schaar J. A., Serruys P. W., and van der Steen A. F. Young's modulus reconstruction of vulnerable atherosclerotic plaque components using deformable curves. *Ultrasound Med Biol*, 32(2):201–10, 2006.

Barger A. C. and Beeuwkes R. Rupture of coronary vasa vasorum as a trigger of acute myocardial infarction. *Am J Cardiol*, 66(16):41G–43G, 1990.

Barger A. C., Beeuwkes R., Lainey L. L., and Silverman K. J. Hypothesis: vasa vasorum and neovascularization of human coronary arteries. A possible role in the pathophysiology of atherosclerosis. *N Engl J Med*, 310(3):175–177, 1984.

Barnett S. B., Ter Haar G. R., Ziskin M. C., Rott H. D., Duck F. A., and Maeda K. International recommendations and guidelines for the safe use of diagnostic ultrasound in medicine. *Ultrasound Med Biol*, 26(3): 355–366, 2000.

Bayram B., Oralkan Ö., Ergun A. S., Hæggström E., Yaralioglu G. G., and Khuri-Yakub B. T. Capacitive micromachined ultrasonic transducer design for high power transmission. *IEEE Trans Ultrason Ferroelectr Freq Control*, 52(2):326–339, 2005.

Blessing E., Hausmann D., Sturm M., Wolpers H. G., Amende I., and Mugge A. Intravascular ultrasound and stent implantation: intraobserver and interobserver variability. *Am Heart J*, 137(2):368–371, 1999.

Bouakaz A. and De Jong N. New contrast imaging method using double frequency exposure. In *IEEE Ultrason Ferroelec Freq Control Symp Proc*, pages 339–342, 2004.

Bouakaz A., Frigstad S., Ten Cate F. J., and de Jong N. Super harmonic imaging: a new imaging technique for improved contrast detection. *Ultrasound Med Biol*, 28(4):59–68, 2002.

Bouakaz A., Lancee C. T., and de Jong N. Harmonic ultrasonic field of medical phased arrays: Simulations and measurements. *IEEE Trans Ultrason Ferroelec Freq Control*, 50(6):730–735, 2003.

Brezinski M. E. Optical coherence tomography for identifying unstable coronary plaque. *Int J Cardiol*, 107 (2):154–165, 2006.

Brezinski M. E., Tearney G. J., Weissman N. J., Boppart S. A., Bouma B. E., Hee M. R., Weyman A. E., Swanson E. A., Southern J. F., and Fujimoto J. G. Assessing atherosclerotic plaque morphology: comparison of optical coherence tomography and high frequency intravascular ultrasound. *Heart*, 77(5):397–403, 1997.

Brock-Fisher G., Poland M., and Rafter P. Means for increasing sensitivity in nonlinear ultrasound imaging systems, Nov. 26 1996.

Bruining N., Sabate M., and Serruys P. W. Clinical implications of intravascular ultrasound imaging for stenting procedures. *Am Heart J*, 137(2):207–210, 1999.

Burns P. N., Hope Simpson D., and Averkiou M. A. Nonlinear imaging. *Ultrasound Med Biol*, 26 Suppl 1: S19–22, 2000.

Cachard C., Finet G., Bouakaz A., Tabib A., Francon D., and Gimenez G. Ultrasound contrast agent in intravascular echography: an in vitro study. *Ultrasound Med Biol*, 23(5):705–717, 1997.

Carlier S., Kakadiaris I. A., Dib N., Vavuranakis M., O'Malley S. M., Gul K., Hartley C. J., Metcalfe R., Mehran R., Stefanadis C., Falk E., Stone G., Leon M., and Naghavi M. Vasa vasorum imaging: a new window to the clinical detection of vulnerable atherosclerotic plaques. *Curr Atheroscler Rep*, 7(2):164–169, 2005.

Casscells W., Hassan K., Vaseghi M. F., Siadaty M. S., Naghavi M., Kirkeeide R. L., Hassan M. R., and Madjid M. Plaque blush, branch location, and calcification are angiographic predictors of progression of mild to moderate coronary stenoses. *Am Heart J*, 145(5):813–820, 2003.

Cherin E. W., Poulsen J. K., van der Steen A. F. W., Lum P., and Foster F. S. Experimental characterization of fundamental and second harmonic beams for a high-frequency ultrasound transducer. *Ultrasound Med Biol*, 28(5):635–646, 2002.

Christopher T. Finite amplitude distortion-based inhomogeneous pulse echo ultrasonic imaging. *IEEE Trans Ultrason Ferroelectr Freq Control*, 44(1):125–139, 1997.

de Boer O. J., van der Wal A. C., Teeling P., and Becker A. E. Leucocyte recruitment in rupture prone regions of lipid-rich plaques: a prominent role for neovascularization? *Cardiovasc Res*, 41(2):443–449, 1999.

de Feyter P. J. and Nieman K. New coronary imaging techniques: what to expect? *Heart*, 87(3):195–197, 2002.

De Jong N. *Acoustic properties of ultrasound contrast agents*. PhD thesis, EUR, 1993.

de Korte C. L., Cespedes E. I., van der Steen A. F. W., Norder B., and te Nijenhuis K. Elastic and acoustic properties of vessel mimicking material for elasticity imaging. *Ultrason Imaging*, 19(2):112–126, 1997.

de Korte C. L., van der Steen A. F. W., Cespedes E. I., and Pasterkamp G. Intravascular ultrasound elastography in human arteries: initial experience in vitro. *Ultrasound Med Biol*, 24(3):401–408, 1998.

de Korte C. L., Sierevogel M. J., Mastik F., Strijder C., Schaar J. A., Velema E., Pasterkamp G., Serruys P. W., and van der Steen A. F. Identification of atherosclerotic plaque components with intravascular ultrasound elastography in vivo: a yucatan pig study. *Circulation*, 105(14):1627–1630, 2002.

Degertekin M., Lemos P. A., Lee C. H., Tanabe K., Sousa J. E., Abizaid A., Regar E., Sianos G., van der Giessen W. J., de Feyter P. J., Wuelfert E., Popma J. J., and Serruys P. W. Intravascular ultrasound evaluation after sirolimus eluting stent implantation for de novo and in-stent restenosis lesions. *Eur Heart J*, 25(1): 32–38, 2004.

Demos S. M., Alkan-Onyuksel H., Kane B. J., Ramani K., Nagaraj A., Greene R., Klegerman M., and McPherson D. D. In vivo targeting of acoustically reflective liposomes for intravascular and transvascular ultrasonic enhancement. *J Am Coll Cardiol*, 33(3):867–875, 1999.

Doyley M. M., Mastik F., de Korte C. L., Carlier S. G., Cespedes E. I., Serruys P. W., Bom N., and van der Steen A. F. Advancing intravascular ultrasonic palpation toward clinical applications. *Ultrasound Med Biol*, 27(11):1471–1480, 2001.

Duck F. A. Nonlinear acoustics in diagnostic ultrasound. *Ultrasound Med Biol*, 28(1):1–18, 2002.

Duck F. A. *Physical properties of tissue*. Academic Press Limited, London, 1990.

Duck F. A. Acoustic saturation and output regulation. *Ultrasound Med Biol*, 25(6):1009–18, 1999.

Edelman E. R., Nugent M. A., Smith L. T., and Karnovsky M. J. Basic fibroblast growth factor enhances the coupling of intimal hyperplasia and proliferation of vasa vasorum in injured rat arteries. *J Clin Invest*, 89 (2):465–473, 1992.

Eeckhout E., Berger A., Roguelov C., Lyon X., Imsand C., Fivaz-Arbane M., Girod G., and De Benedetti E. Direct stenting with a combined intravascular ultrasound-coronary stent delivery platform: a feasibility trial. *Catheter Cardiovasc Interv*, 59(4):451–454, 2003.

Fayad Z. A., Fuster V., Fallon J. T., Jayasundera T., Worthley S. G., Helft G., Aguinaldo J. G., Badimon J. J., and Sharma S. K. Noninvasive in vivo human coronary artery lumen and wall imaging using black-blood magnetic resonance imaging. *Circulation*, 102(5):506–510, 2000.

Feinstein S. B. The powerful microbubble: from bench to bedside, from intravascular indicator to therapeutic delivery system, and beyond. *Am J Physiol Heart Circ Physiol*, 287(2):H450–457, 2004.

Finet G., Cachard C., Delachartre P., Maurincomme E., and Beaune J. Artifacts in intravascular ultrasound imaging during coronary artery stent implantation. *Ultrasound Med Biol*, 24(6):793–802, 1998.

Forsberg F., Shi W. T., and Goldberg B. B. Subharmonic imaging of contrast agents. *Ultrasonics*, 38(1-8): 93–98, 2000.

Foster F. S., Ryan L. K., and Turnbull D. H. Characterization of lead zirconate titanate ceramics for use in miniature high-frequency (20-80 MHz) transducers. *IEEE Trans Ultrason Ferroelec Freq Control*, 38(5): 446–453, 1991.

Foster F. S., Harasiewicz E. A., and Sherar M. D. A history of medical and biological imaging with polyvinylidene fluoride (PVDF) transducers. *IEEE Trans Ultrason Ferroelec Freq Control*, 47(6):1363–1371, 2000a.

Foster F. S., Pavlin C. J., Harasiewicz K. A., Christopher D. A., and Turnbull D. H. Advances in ultrasound biomicroscopy. *Ultrasound Med Biol*, 26(1):1–27, 2000b.

Foster F. S., Zhang M. Y., Zhou Y. Q., Liu G., Mehi J., Cherin E., Harasiewicz K. A., Starkoski B. G., Zan L., Knapik D. A., and Adamson S. L. A new ultrasound instrument for in vivo microimaging of mice. *Ultrasound Med Biol*, 28(9):1165–1172, 2002.

Frijlink M. E., Goertz D. E., van Damme L. C. A., Krams R., and van der Steen A. F. W. Intravascular ultrasound tissue harmonic imaging in vivo. In *IEEE Ultrason Ferroelec Freq Control Symp Proc*, pages 1118–1121, Montreal, 2004.

Frinking P. J. A. *Ultrasound Contrast Agents*. PhD thesis, EUR, 1999.

Glagov S., Weisenberg E., Zarins C. K., Stankunavicius R., and Kolettis G. J. Compensatory enlargement of human atherosclerotic coronary arteries. *N Engl J Med*, 316(22):1371–1375, 1987.

Goertz D. E., Wong S. W. S., Chin C. T., Cherin E., Burns P. N., and Foster F. S. Non-linear scattering from microbubble contrast agents in the 14-40 mhz range. In *IEEE Ultrason Ferroelec Freq Control Symp Proc*, pages 1747–1751, 2001.

Goertz D. E., Yu J. L., Kerbel R. S., Burns P. N., and Foster F. S. High-frequency doppler ultrasound monitors the effects of antivascular therapy on tumor blood flow. *Cancer Res*, 62(22):6371–6375, 2002.

Goertz D. E., Frijlink M. E., Bouakaz A., Chin C. T., de Jong N., and van der Steen A. F. W. The effect of bubble size on nonlinear scattering at high frequencies. In *IEEE Ultrason Ferroelec Freq Control Symp Proc*, pages 1503–1507, 2003a.

Goertz D. E., Yu J. L., Kerbel R. S., Burns P. N., and Foster F. S. High-frequency 3-d color-flow imaging of the microcirculation. *Ultrasound Med Biol*, 29(1):39–51, 2003b.

Goertz D. E., Frijlink M. E., de Jong N., and van der Steen A. F. W. High frequency nonlinear scattering and imaging of a submicron contrast agent. In *IEEE Ultrason Ferroelec Freq Control Symp Proc*, pages 986–989, 2004.

Goertz D. E., Cherin E., Needles A., Karshafian R., Brown A. S., Burns P. N., and Foster F. S. High frequency nonlinear b-scan imaging of microbubble contrast agents. *IEEE Trans Ultrason Ferroelectr Freq Control*, 52(1):65–79, 2005a.

Goertz D. E., van Wamel J. E. T., Frijlink M. E., De Jong N., and van der Steen A. F. W. Nonlinear imaging of targeted microbubbles with intravascular ultrasound. In *IEEE Ultrason Ferroelec Freq Control Symp Proc*, pages 2003–2006, 2005b.

Goertz D. E., Frijlink M. E., de Jong N., and van der Steen A. F. W. Nonlinear intravascular ultrasound contrast imaging. *Ultrasound Med Biol*, 32(4):491–502, 2006a.

Goertz D. E., Frijlink M. E., de Jong N., and Van der Steen A. F. W. High frequency nonlinear scattering from a micrometer to submicrometer sized lipid encapsulated contrast agent. *Ultrasound Med Biol*, 32(4): 569–577, 2006b.

Goldberg B. B. *Ultrasound contrast agents: Basic principles and clinical applications in echocardiography*, volume Second edition. Martin Dunitz, London, 2001.

Gorce J. M., Arditi M., and Schneider M. Influence of bubble size distribution on the echogenicity of ultrasound contrast agents: a study of sonovue. *Invest Radiol*, 35(11):661–671, 2000.

Gossl M., Rosol M., Malyar N. M., Fitzpatrick L. A., Beighley P. E., Zamir M., and Ritman E. L. Functional anatomy and hemodynamic characteristics of vasa vasorum in the walls of porcine coronary arteries. *Anat Rec A Discov Mol Cell Evol Biol*, 272(2):526–537, 2003.

Gurumurthy K. V. and Arthur R. M. A dispersive model for the propagation of ultrasound in soft tissue. *Ultrason Imaging*, 4(4):355–377, 1982.

Guyton A. C. and Hall J. E. *Human physiology and mechanics of disease*. W. B. Saunders Company, Philadelphia, 6 edition, 1997.

Hamilton M. F. and Blackstock D. T. *Nonlinear Acoustics*. Academic Press, San Diego, 1998.

Hansen R. *New techniques for Detection of Ultrasound Contrast Agents*. PhD thesis, NTNU, 2004.

He P. Simulation of ultrasound pulse propagation in lossy media obeying a frequency power law. *IEEE Trans Ultrason Ferroelectr Freq Control*, 45(1):114–125, 1998.

Herrmann J., Lerman L. O., Rodriguez-Porcel M., Holmes Jr., D. R., Richardson D. M., Ritman E. L., and Lerman A. Coronary vasa vasorum neovascularization precedes epicardial endothelial dysfunction in experimental hypercholesterolemia. *Cardiovasc Res*, 51(4):762–766, 2001.

Hoeks A. P., Brands P. J., Smeets F. A., and Reneman R. S. Assessment of the distensibility of superficial arteries. *Ultrasound Med Biol*, 16(2):121–128, 1990.

Hope Simpson D. H., Chin C. T., and Burns P. N. Pulse inversion doppler: A new method for detecting nonlinear echoes from microbubble contrast agents. *IEEE Trans Ultrason Ferroelec Freq Control*, 46(2): 372–382, 1999.

Hossack J. A., Mauchamp P., and Ratsimandresy L. A high bandwidth transducer optimized for harmonic imaging. In *IEEE Ultrason Ferroelec Freq Control Symp Proc*, volume 2, pages 1021–1024, 2000.

Humphrey V. F. Nonlinear propagation in ultrasonic fields: measurements, modelling and harmonic imaging. *Ultrasonics*, 38(1-8):267–272, 2000.

Hunt J. W., Worthington A. E., and Kerr A. T. The subtleties of ultrasound images of an ensemble of cells: simulation from regular and more random distributions of scatterers. *Ultrasound Med Biol*, 21(3):329–41, 1995.

Jensen J. A. and Svendsen N. B. Calculation of pressure fields from arbitrarily shaped, apodized, and excited ultrasound transducers. *IEEE Trans Ultrason Ferroelec Freq Control*, 39(2):262–267, 1992.

Jensen J. A., Gandhi D., and O'Brien W. D. Ultrasound fields in an attenuating medium. In *IEEE Ultrason Ferroelec Freq Control Symp Proc*, pages 943–946, 1993.

Jorgensen S. M., Demirkaya O., and Ritman E. L. Three-dimensional imaging of vasculature and parenchyma in intact rodent organs with x-ray micro-ct. *Am J Physiol*, 275(3 Pt 2):H1103–1114, 1998.

Kasprzak J. D., Paelinck B., Ten Cate F. J., Vletter W. B., de Jong N., Poldermans D., Elhendy A., Bouakaz A., and Roelandt J. R. Comparison of native and contrast-enhanced harmonic echocardiography for visualization of left ventricular endocardial border. *Am J Cardiol*, 83(2):211–217, 1999.

Kerr A. T. and Hunt J. W. A method for computer simulation of ultrasound doppler color flow images–i. theory and numerical method. *Ultrasound Med Biol*, 18(10):861–872, 1992.

Kerwin W., Hooker A., Spilker M., Vicini P., Ferguson M., Hatsukami T., and Yuan C. Quantitative magnetic resonance imaging analysis of neovasculature volume in carotid atherosclerotic plaque. *Circulation*, 107 (6):851–856, 2003.

Kim W. Y., Stuber M., Bornert P., Kissinger K. V., Manning W. J., and Botnar R. M. Three-dimensional black-blood cardiac magnetic resonance coronary vessel wall imaging detects positive arterial remodeling in patients with nonsignificant coronary artery disease. *Circulation*, 106(3):296–299, 2002.

Kino G. S. *Acoustic waves: Devices, Imaging and Analog signal processing*. Prentice-Hall, Englewood Cliffs, NJ, 1987.

Knight J. G. and Degertekin F. L. Fabrication and characterization of cMUTs for forward looking intravascular ultrasound imaging. In *IEEE Ultrason Ferroelec Freq Control Symp Proc*, pages 577–580, 2003.

Kolodgie F. D., Gold H. K., Burke A. P., Fowler D. R., Kruth H. S., Weber D. K., Farb A., Guerrero L. J., Hayase M., Kutys R., Narula J., Finn A. V., and Virmani R. Intraplaque hemorrhage and progression of coronary atheroma. *N Engl J Med*, 349(24):2316–2325, 2003.

Kruse D. E. and Ferrara K. W. A new high resolution color flow system using an eigendecomposition-based adaptive filter for clutter rejection. *IEEE Trans Ultrason Ferroelectr Freq Control*, 49(10):1384–1399, 2002.

Kruse D. E., Yeh C. K., and Ferrara K. W. A new imaging strategy utilizing wideband transient response of ultrasound contrast agents. In *IEEE Ultrason Ferroelec Freq Control Symp Proc*, pages 424–428, 2003.

Kumamoto M., Nakashima Y., and Sueishi K. Intimal neovascularization in human coronary atherosclerosis: its origin and pathophysiological significance. *Hum Pathol*, 26(4):450–456, 1995.

Kwon H. M., Sangiorgi G., Ritman E. L., McKenna C., Holmes Jr., D. R., Schwartz R. S., and Lerman A. Enhanced coronary vasa vasorum neovascularization in experimental hypercholesterolemia. *J Clin Invest*, 101(8):1551–1556, 1998.

Ladabaum I., Jin X., Soh H. T., Pierre F., Atalar A., and Khuri-Yakub B. T. Microfabricated ultrasonic transducers: towards robust models and immersion devices. In *IEEE Ultrason Ferroelec Freq Control Symp Proc*, pages 335–338, 1996.

Lee Y. S. and Hamilton M. F. Time-domain modeling of pulsed finite-amplitude sound beams. *J Acoust Soc Am*, 97(2):906–917, 1995.

Lethiecq M., Tranhuuhue L. P., Patat F., and Pourcelot L. Measurement of losses in 5 piezoelectric ceramics between 2 and 50 MHz. *IEEE Trans Ultrason Ferroelectr Freq Control*, 40(3):232–237, 1993.

Leung K. Y. E., Baldewsing R. A., Mastik F., Schaar J. A., Gisolf A., and Van der Steen A. F. W. Motion compensation for intravascular ultrasound palpography. *IEEE Trans Ultrason Ferroelec Freq Control*, 53 (7):1269–1280, 2006.

Li W., van der Steen A. F., Lancee C. T., Cespedes I., and Bom N. Blood flow imaging and volume flow quantitation with intravascular ultrasound. *Ultrasound Med Biol*, 24(2):203–214, 1998.

Li Y. D. and Zagzebski J. A. Computer model for harmonic ultrasound imaging. *IEEE Trans Ultrason Ferroelec Freq Control*, 47(4):1000–1013, 2000.

Libby P. Inflammation in atherosclerosis. *Nature*, 420(6917):868–874, 2002.

Lockwood G. R., Hunt J. W., and Foster F. S. The design of protection circuitry for high-frequency ultrasound imaging-systems. *IEEE Trans Ultrason Ferroelec Freq Control*, 38(1):48–55, 1991a.

Lockwood G. R., Ryan L. K., Hunt J. W., and Foster F. S. Measurement of the ultrasonic properties of vascular tissues and blood from 35-65 mhz. *Ultrasound Med Biol*, 17(7):653–666, 1991b.

Lupotti F. A., Mastik F., Carlier S. G., de Korte C. L., van der Giessen W. J., Serruys P. W., and van der Steen A. F. Quantitative IVUS blood flow: validation in vitro, in animals and in patients. *Ultrasound Med Biol*, 29(4):507–515, 2003.

Mackay J. and Mensah G. A. *The atlas of heart disease and stroke*. World health organization, London, 2004.

Meyer R.J., Alkoy S., Newnham R., and Cochran J. Development of materials and composites for > 25 MHz single element transducers. In *IEEE Ultrason Ferroelec Freq Control Symp Proc*, volume 2, pages 1299–1302, 1999.

Milei J., Parodi J. C., Alonso G. F., Barone A., Grana D., and Matturri L. Carotid rupture and intraplaque hemorrhage: immunophenotype and role of cells involved. *Am Heart J*, 136(6):1096–1105, 1998.

Mills D. M. and Smith L. S. Real-time in-vivo imaging with capacitive micromachined ultrasound transducer (cMUT) linear arrays. In *IEEE Ultrason Ferroelec Freq Control Symp Proc*, pages 568–571, 2003.

Mofidi R., Crotty T. B., McCarthy P., Sheehan S. J., Mehigan D., and Keaveny T. V. Association between plaque instability, angiogenesis and symptomatic carotid occlusive disease. *Br J Surg*, 88(7):945–950, 2001.

Mollet N. R., Cademartiri F., and de Feyter P. J. Non-invasive multislice ct coronary imaging. *Heart*, 91(3): 401–407, 2005.

Moran C. M., Watson R. J., Fox K. A., and McDicken W. N. In vitro acoustic characterisation of four intravenous ultrasonic contrast agents at 30 MHz. *Ultrasound Med Biol*, 28(6):785–791, 2002.

Moreno P. R., Purushothaman K. R., Fuster V., Echeverri D., Truszczynska H., Sharma S. K., Badimon J. J., and O'Connor W. N. Plaque neovascularization is increased in ruptured atherosclerotic lesions of human aorta: implications for plaque vulnerability. *Circulation*, 110(14):2032–2038, 2004.

Moulton K. S. Plaque angiogenesis: its functions and regulation. *Cold Spring Harb Symp Quant Biol*, 67: 471–482, 2002.

Moulton K. S., Vakili K., Zurakowski D., Soliman M., Butterfield C., Sylvin E., Lo K. M., Gillies S., Javaherian K., and Folkman J. Inhibition of plaque neovascularization reduces macrophage accumulation and progression of advanced atherosclerosis. *Proc Natl Acad Sci U S A*, 100(8):4736–4741, 2003.

Nair A., Kuban B. D., Tuzcu E. M., Schoenhagen P., Nissen S. E., and Vince D. G. Coronary plaque classification with intravascular ultrasound radiofrequency data analysis. *Circulation*, 106(17):2200–2206, 2002.

Naugolnykh K. and Ostrovsky L. *Nonlinear Wave Processes in Acoustics*. Cambridge University Press, Cambridge, 1998.

NRC . *Guide for the care and use of laboratory animals*. National Research Council, National Academy Press, Washington D.C., 1996.

Oralkan O., Ergun A. S., Johnson J. A., Karaman M., Demirci U., Kaviani K., Lee T. H., and Khuri-Yakub B. T. Capacitive micromachined ultrasonic transducers: Next-generation arrays for acoustic imaging? *IEEE Trans Ultrason Ferroelectr Freq Control*, 49(11):1596–1610, 2002.

Qiu B., Karmarkar P., Brushett C., Gao F., Kon R., Kar S., Atalar E., and Yang X. Development of a 0.014-inch magnetic resonance imaging guidewire. *Magn Reson Med*, 53(4):986–990, 2005.

Reiber J. H. C. and Serruys P. W. *Quantitative Coronary Arteriography*, volume 117 of *Developments in Cardiovascular Medicine*. kluwer Academic Publishers, Dordrecht, 1991.

Roelandt J. R., di Mario C., Pandian N. G., Wenguang L., Keane D., Slager C. J., de Feyter P. J., and Serruys P. W. Three-dimensional reconstruction of intracoronary ultrasound images. rationale, approaches, problems, and directions. *Circulation*, 90(2):1044–1055, 1994.

Römer T. J., Brennan J. F., Schut T. C., Wolthuis R., van den Hoogen R. C., Emeis J. J., van der Laarse A., Bruschke A. V., and Puppels G. J. Raman spectroscopy for quantifying cholesterol in intact coronary artery wall. *Atherosclerosis*, 141(1):117–124, 1998.

Saijo Y. and van der Steen A. F. W. *Vascular Ultrasound*. Springer Verlag, Tokyo, 2003.

Saitoh S., Izumi M., and Mine Y. A dual frequency ultrasonic probe for medical applications. *IEEE Trans Ultrason Ferroelectr Freq Control*, 42:294–300, 1995.

Schaar J. A. *Palpography*. PhD thesis, Erasmus University Rotterdam, 2005.

Schaar J. A., Muller J. E., Falk E., Virmani R., Fuster V., Serruys P. W., Colombo A., Stefanadis C., Ward Casscells S., Moreno P. R., Maseri A., and van der Steen A. F. Terminology for high-risk and vulnerable coronary artery plaques. report of a meeting on the vulnerable plaque, june 17 and 18, 2003, santorini, greece. *Eur Heart J*, 25(12):1077–1082, 2004.

Schaar J. A., de Korte C. L., Mastik F., van Damme L. C., Krams R., Serruys P. W., and van der Steen A. F. W. Three-dimensional palpography of human coronary arteries. *Herz*, 30(2):125–133, 2005.

Schindel D. W., Hutchins D. A., Zou L. C., and Sayer M. The design and characterization of micromachined air-coupled capacitance transducers. *IEEE Trans Ultrason Ferroelectr Freq Control*, 42(1):42–50, 1995.

Schmitt J. M. Oct elastography: imaging microscopic deformation and strain of tissue. *Optics Express*, 3(6): 199–211, 1998.

Schneiderman J., Wilensky R. L., Weiss A., Samouha E., Muchnik L., Chen-Zion M., Ilovitch M., Golan E., Blank A., Flugelman M., Rozenman Y., and Virmani R. Diagnosis of thin-cap fibroatheromas by a self-contained intravascular magnetic resonance imaging probe in ex vivo human aortas and in situ coronary arteries. *J Am Coll Cardiol*, 45(12):1961–1969, 2005.

Serruys P. W., de Jaegere P., Kiemeneij F., Macaya C., Rutsch W., Heyndrickx G., Emanuelsson H., Marco J., Legrand V., Materne P., and et al. . A comparison of balloon-expandable-stent implantation with balloon angioplasty in patients with coronary artery disease. Benestent Study Group. *N Engl J Med*, 331(8):489–495, 1994.

Shankar P. M., Dala Krishna P., and Newhouse V. L. Advantages of subharmonic over second harmonic backscatter for contrast-to-tissue echo enhancement. *Ultrasound Med Biol*, 24(3):395–399, 1998.

Shen C. C. and Li P. C. Motion artifacts of pulse inversion-based tissue harmonic imaging. *IEEE Trans Ultrason Ferroelec Freq Control*, 49(9):1203–1211, 2002.

Shen C. C. and Li P. C. Pulse-inversion-based fundamental imaging for contrast detection. *IEEE Trans Ultrason Ferroelectr Freq Control*, 50(9):1124–1133, 2003.

Sherar M. D. and Foster F. S. The design and fabrication of high frequency poly(vinylidene fluoride) transducers. *Ultrason Imaging*, 11(2):75–94, 1989.

Silbernagl S. and Despopoulos A. *Sesam atlas van de fysiologie*. Bosch en Keuning, Baarn, the Netherlands, 1981.

Snook K. A., Zhao J. Z., Alves C. H., Cannata J. M., Chen W. H., Meyer Jr., R. J., Ritter T. A., and Shung K. K. Design, fabrication, and evaluation of high frequency, single-element transducers incorporating different materials. *IEEE Trans Ultrason Ferroelectr Freq Control*, 49(2):169–176, 2002.

Stefanadis C., Diamantopoulos L., Vlachopoulos C., Tsiamis E., Dernellis J., Toutouzas K., Stefanadi E., and Toutouzas P. Thermal heterogeneity within human atherosclerotic coronary arteries detected in vivo: A new method of detection by application of a special thermography catheter. *Circulation*, 99(15):1965–1971, 1999.

Stephanishen P. R. Transient radiation from pistons in an infinite planar baffle. *J Acoust Soc Am*, 49(5): 1629–1638, 1971.

Szabo T. L. Time-domain wave-equations for lossy media obeying a frequency power-law. *J Acoust Soc Am*, 96(1):491–500, 1994.

Szabo T. L. Causal theories and data for acoustic attenuation obeying a frequency power-law. *J Acoust Soc Am*, 97(1):14–24, 1995.

Takeuchi S., Al Zaabi M. R. A., Sato T., and Kawashima N. Development of ultrasound transducer with double-peak-type frequency characteristics for harmonic imaging and subharmonic imaging. *Jap J Appl Phys*, 41:3619–3623, 2002.

ten Have A. G., Gijsen F. J. H., Wentzel J. J., Slager C. J., Serruys P. W., and van der Steen A. F. W. Intracoronary thermography: heat generation, transfer and detection. *EoroIntervention*, 1(1):105–114, 2005.

Tenaglia A. N., Peters K. G., Sketch Jr., M. H., and Annex B. H. Neovascularization in atherectomy specimens from patients with unstable angina: implications for pathogenesis of unstable angina. *Am Heart J*, 135(1): 10–14, 1998.

Thrush A. J., Bonnett D. E., Elliott M. R., Kutob S. S., and Evans D. H. An evaluation of the potential and limitations of three-dimensional reconstructions from intravascular ultrasound images. *Ultrasound Med Biol*, 23(3):437–445, 1997.

Tortoli P., Bettarini R., Guidi F., Andreuccetti F., and Righi D. A simplified approach for real-time detection of arterial wall velocity and distension. *IEEE Trans Ultrason Ferroelec Freq Control*, 48(4):1005–1012, 2001.

Tranquart F., Grenier N., Eder V., and Pourcelot L. Clinical use of ultrasound tissue harmonic imaging. *Ultrasound Med Biol*, 25(6):889–894, 1999.

Uchida Y., Nakamura F., Tomaru T., Morita T., Oshima T., Sasaki T., Morizuki S., and Hirose J. Prediction of acute coronary syndromes by percutaneous coronary angioscopy in patients with stable angina. *Am Heart J*, 130(2):195–203, 1995.

van de Poll S. W., Romer T. J., Volger O. L., Delsing D. J., Bakker Schut T. C., Princen H. M., Havekes L. M., Jukema J. W., van Der Laarse A., and Puppels G. J. Raman spectroscopic evaluation of the effects of diet and lipid-lowering therapy on atherosclerotic plaque development in mice. *Arterioscler Thromb Vasc Biol*, 21(10):1630–1635, 2001.

van der Steen A. F. W., Poulsen J. K., Cherin E., and Foster F. S. Harmonic imaging at high frequencies for IVUS. In *IEEE Ultrason Ferroelec Freq Control Symp Proc*, volume 2, pages 1537–1540, 1999.

Verheye S., De Meyer G. R., Van Langenhove G., Knaapen M. W., and Kockx M. M. In vivo temperature heterogeneity of atherosclerotic plaques is determined by plaque composition. *Circulation*, 105(13):1596–1601, 2002.

von Birgelen C., Mintz G. S., Eggebrecht H., Herrmann J., Jasper M., Brinkhoff J., Neumann T., Bose D., Baumgart D., Schmermund A., Wieneke H., Haude M., and Erbel R. Preintervention arterial remodeling affects vessel stretch and plaque extrusion during coronary stent deployment as demonstrated by three-dimensional intravascular ultrasound. *Am J Cardiol*, 92(2):130–135, 2003.

Wallace K. D., Holland M. R., and Miller J. G. Improved description of shock wave evolution in media with frequency power law dependent attenuation. *J Acoust Soc Am*, 109(5):2263–2265, 2001. Part 1.

Ward B., Baker A. C., and Humphrey V. F. Nonlinear propagation applied to the improvement of lateral resolution in medical ultrasound scanners. In *World Congress on Ultrasonics*, pages 965–968, 1995.

Ward B., Baker A. C., and Humphrey V. F. Nonlinear propagation applied to the improvement of resolution in diagnostic medical ultrasound. *J Acoust Soc Am*, 101(1):143–154, 1997.

Williams M. J., Stewart R. A., Low C. J., and Wilkins G. T. Assessment of the mechanical properties of coronary arteries using intravascular ultrasound: an in vivo study. *Int J Card Imaging*, 15(4):287–294, 1999.

Winter P. M., Morawski A. M., Caruthers S. D., Fuhrhop R. W., Zhang H., Williams T. A., Allen J. S., Lacy E. K., Robertson J. D., Lanza G. M., and Wickline S. A. Molecular imaging of angiogenesis in early-stage atherosclerosis with alpha(v)beta3-integrin-targeted nanoparticles. *Circulation*, 108(18):2270–2274, 2003.

Yuan C. and Kerwin W. S. Mri of atherosclerosis. *J Magn Reson Imaging*, 19(6):710–719, 2004.

Zamir M. and Silver M. D. Vasculature in the walls of human coronary arteries. *Arch Pathol Lab Med*, 109 (7):659–662, 1985.

Zhang Y., Cliff W. J., Schoefl G. I., and Higgins G. Immunohistochemical study of intimal microvessels in coronary atherosclerosis. *Am J Pathol*, 143(1):164–172, 1993.

Zhao J.-Z., Alves C.H.F., Snook K.A., Cannata J.M., Chen W.-H., Meyer Jr. R.J., Ayyappan S., Ritter T.A., and Shung K.K. Performance of 50MHz transducers incorporating fiber composite, PVDF, PbTiO3 and LiNbO3. In *IEEE Ultrason Ferroelec Freq Control Symp Proc*, pages 1185–1190, 1999.

Zhou S., Reynolds P., and Hossack J. A. Precompensated excitation waveforms to suppress harmonic generation in MEMS elctrostatic transducers. *IEEE Trans Ultrason Ferroelectr Freq Control*, 51(11):1564–1574, 2004.

Zhou Y. Q., Cannata J. M., Huang C. Z., Guo H. K., Marmarelis V., and Shung K. K. Fabrication and modeling of inversion layer ultrasonic transducers using $LiNbO_3$ single crystal. In *IEEE Ultrason Ferroelec Freq Control Symp Proc*, pages 1034–1037, 2003.

Samenvatting

Intravasculair ultrageluid (IVUS) is een techniek waarbij door middel van een catheter bloedvaten van binnenuit onderzocht kunnen worden met ultrageluid. De afbeelding van acoustische eigenschappen van de vaatwand kan op deze manier leiden tot real-time tweedimensionale doorsneden van bloedvaten. Hierdoor is IVUS momenteel een belangrijke diagnostische afbeeldingsmethode voor zowel de detectie en evaluatie van atherosclerotische plaques, als tijdens therapeutische interventies en klinisch onderzoek. Toch zou de beeldkwaliteit mogelijk verbeterd kunnen worden door een techniek genaamd "Harmonic Imaging", waarbij hogere harmonischen van de uitgezonden ultrageluidsfrequentie worden gebruikt voor afbeeldingen. Deze techniek wordt veelvuldig gebruikt in de conventionele echocardiografie (ultrageluidsfrequenties tussen 1 en 10 MHz). De harmonische beeldvormingstechniek kan de beeldkwaliteit verhogen door ongewenste beeldartefacten te verminderen (Tissue Harmonic Imaging) en de detectie van ultrageluidscontrastmiddelen verbeteren (Contrast Harmonic Imaging). Ondanks dat deze techniek zijn nut reeds heeft bewezen bij lage ultrageluidsfrequenties, zijn er weinig studies verricht die de mogelijkheden van deze techniek voor intravasculaire ultrageluidstoepassingen hebben onderzocht. Dit proefschrift beschrijft onderzoek naar de uitvoerbaarheid, potentiële voordelen en mogelijke klinische toepassingen van Harmonic IVUS Imaging, vooral met betrekking tot vulnerabele plaque detectie.

Een meetopstelling is gebruikt om experimenteel de uitvoerbaarheid en potentiële voordelen van zowel Tissue als Contrast Harmonic imaging (CHI) te onderzoeken bij gebruik op intravasculaire ultrageluids frequenties (hoofdstuk 2). Eerste resultaten met deze opstelling laten zien dat Tissue Harmonic Imaging (THI) beeldartefacten kan reduceren van een reflecterende stent in het nabije veld van een gefocusseerde ultrageluidsbundel, afkomstig van een transducent voor acoustische microscopie toepassingen (hoofdstuk 3). Ondanks dat is aangetoond dat ook een ongefocusseerde IVUS transducent een ultrageluidsbundel op de tweede harmonische frequentie (40 MHz) kan genereren en detecteren, werd niet een duidelijke vermindering van door de stent veroorzaakte beeldartefacten waargenomen. Wel lieten de THI resultaten een nauwkeuriger omlijning zien van de stent wanneer deze zich dichtbij de ongefocusseerde IVUS transducent

bevond.

In een volgende studie is een prototype harmonisch IVUS systeem met een conventionele continu roterende IVUS catheter gebruikt om de uitvoerbaarheid van THI te demonstreren in een weefselmodel en in een atherosclerotische aorta van een konijnenmodel *in vivo* (hoofdstuk 4). Deze studie toont ook de potentie van THI om beeldartefacten te reduceren in situaties zonder de aanwezigheid van reflecterende stents. Ten eerste verminderde THI het gecombineerde effect van verzadiging van de versterker en de reflecterende beschermmantel rond de IVUS transducent, zichtbaar als een witte ring dicht om de catheter heen. Dit resultaat komt overeen met niet-lineaire simulaties en gemeten twee-dimensionale bundelprofielen. Ten tweede, was de gemeten signaalverzwakking als functie van penetratiediepte minder tijdens harmonische beeldvorming (40 MHz) dan tijdens fundamentele beeldvorming (20 en 40 MHz). Ook dit is consistent met niet-lineaire simulaties en hydrofoonmetingen.

Omdat een voor harmonisch IVUS geoptimaliseerde ultrageluidstransducent harmonische beeldvorming zou kunnen vergemakkelijken, is een nieuwe IVUS transducent ontworpen, gefabriceerd en gekarakteriseerd (hoofdstuk 5). De ultrageluidstransducent was ontworpen voor harmonische beeldvorming in het frequentiebereik van 20 tot 40 MHz. Metingen aan deze transducent toonde een frequentiekarakteristiek met twee pieken op 20 en 40 MHz, veroorzaakt door een dubbel-laags structuur bestaande uit een actieve laag van piëzo-electrisch materiaal en een passieve resonantielaag. Vergeleken met een conventionele IVUS transducent bleek de gevoeligheid van de dubbel-laags transducent rond 20 MHz ongeveer te zijn verdubbeld, terwijl de gevoeligheid rond 40 MHz nagenoeg hetzelfde was.

Een aangepaste versie van de custom-made IVUS transducent is gemonteerd op een conventionele catheter (hoofdstuk 6). Deze catheter met een dubbele-frequentie karakteristiek is vervolgens geëvalueerd voor THI (zenden rond 20 MHz, ontvangen rond 40 MHz) in combinatie met het prototype harmonisch IVUS systeem en vergeleken met een conventionele IVUS catheter. Karakterisatie-experimenten toonden aan dat de custom-made catheter een verbeterde zend-efficiëntie rond 20 MHz had. Hierdoor lieten harmonische beeldvormings-experimenten met deze catheter onder een vergelijkbare omstandigheid in zowel een weefselmodel als in een *in vivo* konijnenaorta een hogere signaal-ruis-verhouding zien.

Een simulatiemodel is ontwikkeld om niet-lineaire IVUS bundels te berekenen en de invloed van catheterrotatie en relatieve axiale-catheterbeweging op de efficiëntie van "puls inversie" te onderzoeken (hoofdstuk 7). "Puls inversie" is een signaalverwerkingstechniek die gebruikt wordt om lineaire componenten uit een ontvangen signaal te filteren. Een studie met dit simulatiemodel stelde vast dat de lineaire component

op de fundamentele frequentie met meer dan 25 decibel (dB) onderdrukt kan worden bij een rotatiehoek van 0.15° tussen opeenvolgende beeldlijnen, overeenkomstig met een lijndichtheid van 2400 lijnen per rotatie. Deze lijndichtheid is compatibel met huidige klinische IVUS apparatuur waarbij een rotatiesnelheid van 30 omwentelingen per seconde wordt gebruikt. Het effect van relatieve axiale catheterbeweging op de gemiddelde onderdrukking van het lineaire signaal op de fundamentele frequentie bleek weinig invloed te hebben voor puls-repetitie frequenties van 12.5 kHz en hoger. Deze simulatieresultaten zijn consistent met de efficiëntie van "puls inversie" zoals deze gebruikt is in de harmonische beeldvormings-experimenten die beschreven zijn in dit proefschrift.

De eerste resultaten van niet-lineaire detectie van ultrageluidscontrastmiddelen met IVUS apparatuur zijn beschreven in hoofdstuk 8. De toepasbaarheid van zowel subharmonische als tweede harmonische beeldvorming is gedemonstreerd met een experimenteel contrastmiddel, bestaande uit met een lipide schil omhulde gasbelletjes met een gemiddelde diameter in de orde van een micrometer. Initiële resultaten van subharmonische beeldvormingsexperimenten met een IVUS catheter laten zien dat de contrast-weefselverhouding toeneemt bij hogere acoustische drukken, terwijl bij tweede harmonische beeldvorming deze verhouding relatief afneemt bij hogere drukken, als gevolg van toenemende niet-lineaire propagatie.

De toepasbaarheid van tweede harmonische contrastdetectie is tenslotte aangetoond *in vivo* (hoofdstuk 9). De microvasculatuur in de vaatwand (*vasa vasorum*) van een atherosclerotische konijnenaorta is afgebeeld door middel van niet-lineaire detectie van een gemodificeerd klinisch goedgekeurd contrastmiddel met het prototype harmonisch IVUS systeem. Deze microvasculatuur kon niet gedetecteerd worden met conventioneel IVUS. Deze studie demonstreert dat CHI met IVUS catheters een veelbelovende techniek is voor *in vivo* visualisatie van de *vasa vasorum*.

Concluderend kan gesteld worden dat Harmonisch Intravasculair Ultrageluid een veelbelovende diagnostische methode is voor zowel de detectie, evaluatie en behandeling van atherosclerose als voor cardiovasculair onderzoek. IVUS Tissue Harmonic Imaging maakt het mogelijk om de beeldkwaliteit van diagnostische IVUS-beelden te verbeteren. IVUS Contrast Harmonic Imaging kan leiden tot een gevoelige, robuuste en kwantitatieve techniek voor *in vivo* beeldvorming van microvasculatuur zoals bijvoorbeeld de *vasa vasorum*.

curriculum vitae

Personal

name	Frijlink, Martijn Egbert
date of birth	20 November 1976
place of birth	's Gravenhage, the Netherlands
nationality	Dutch

Education

1989—1995	V.W.O. (pre-university education), Erasmus College, Zoetermeer, the Netherlands
1995—2001	Delft University of Technology, the Netherlands M.Sc. in Electrical Engineering master thesis: *"Fast framing camera system for visualising the dynamic behaviour of ultrasound contrast agents in ultrasound fields"* supervisors: Prof.dr.ir. N. de Jong and Dr.ir. R.P. van Wijk van Brievingh
2001—present	Junior researcher at the Biomedical Engineering department of the Thoraxcenter of ErasmusMC, University Medical Center Rotterdam, the Netherlands. Ph.D. in Biomedical Engineering, to be expected in September 2006 thesis: *"Harmonic Intravascular Ultrasound"* supervisor: Prof.dr.ir. A.F.W. van der Steen